Design, Growth, and Characterization of III-Sb and III-N Materials for Photovoltaic Applications

by

Ehsan Vadiee

A Dissertation Presented in Partial Fulfillment
of the Requirements for the Degree
Doctor of Philosophy

Approved April 2019 by the
Graduate Supervisory Committee:

Christiana B. Honsberg, Chair
William A. Doolittle
Stephen M. Goodnick
Richard R. King

ARIZONA STATE UNIVERSITY

May 2019

ABSTRACT

Photovoltaic (PV) energy has shown tremendous improvements in the past few decades showing great promises for future sustainable energy sources. Among all PV energy sources, III-V-based solar cells have demonstrated the highest efficiencies. This dissertation investigates the two different III-V solar cells with low (III-antimonide) and high (III-nitride) bandgaps.

III-antimonide semiconductors, particularly aluminum (indium) gallium antimonide alloys, with relatively low bandgaps, are promising candidates for the absorption of long wavelength photons and thermophotovoltaic applications. GaSb and its alloys can be grown metamorphically on non-native substrates such as GaAs allowing for the understanding of different multijunction solar cell designs. The work in this dissertation presents the molecular beam epitaxy growth, crystal quality, and device performance of $Al_xGa_{1-x}Sb$ solar cells grown on GaAs substrates. The motivation is on the optimization of the growth of $Al_xGa_{1-x}Sb$ on GaAs (001) substrates to decrease the threading dislocation density resulting from the significant lattice mismatch between GaSb and GaAs. GaSb, $Al_{0.15}Ga_{0.85}Sb$, and $Al_{0.5}Ga_{0.5}Sb$ cells grown on GaAs substrates demonstrate open-circuit voltages of 0.16, 0.17, and 0.35 V, respectively. In addition, a detailed study is presented to demonstrate the temperature dependence of (Al)GaSb PV cells.

III-nitride semiconductors are promising candidates for high-efficiency solar cells due to their inherent properties and pre-existing infrastructures that can be used as a leverage to improve future nitride-based solar cells. However, to unleash the full potential of III-nitride alloys for PV and PV-thermal (PVT) applications, significant progress in growth, design, and device fabrication are required. In this dissertation, first, the performance of

InGaN solar cells designed for high temperature application (such as PVT) are presented showing robust cell performance up to 600 ºC with no significant degradation.

In the final section, extremely low-resistance GaN-based tunnel junctions with different structures are demonstrated showing highly efficient tunneling characteristics with negative differential resistance (NDR). To improve the efficiency of optoelectronic devices such as UV emitters the first AlGaN tunnel diode with Zener characteristic is presented. Finally, enabled by GaN tunnel junction, the first tunnel contacted InGaN solar cell with a high V_{OC} value of 2.22 V is demonstrated.

ACKNOWLEDGMENTS

I want to acknowledge my advisor, Christiana Honsberg, at Arizona State University (ASU) for never losing faith in me or my abilities. Her constant support and willingness to provide the facilities and platforms I needed to conduct my research was instrumental to my graduate studies. Also, I would like to recognize my co-advisor, W. Alan Doolittle, at Georgia Institute of Technology (Georgia Tech). I am incredibly appreciative of him allowing me to work in his research laboratory and educating me on MBE reactors, vacuum parts, molecular beam dynamics, crystal growth, and device physics. I would not be where I am today without the constant support from both my advisors.

I would like to thank my various collaborators at Arizona State University (ASU), Soitec Inc., Photonitride Inc., University of New Mexico, and Georgia Tech who helped me throughout my Ph.D. period: Dr. Chaomin Zhang, Dr. Joshua Williams, Dr. Alec Fischer, Dr. Yi Fang, Dr. Nikolai Faleev, Dr. Brooks Tellekamp, Dr. Joshua Shank, Alex Weidenbach, Zachary Engel, Christopher Matthews, Dr. Heather McFavilen, Dr. Chantal Arena, Dr. Emma Renteria, Prof. Ganesh Balakrishnan, Prof. Fernando Ponce, Prof. Richard R. King, and Prof. Stephen Goodnick. Special thanks to Evan Clinton at Georgia Tech for being a wonderful colleague and most importantly, a good friend.

Thanks to the LeRoy Eyring Center for Solid State Science and Nanofab at ASU. I would especially like to thank the Institute for Electronics Nanotechnology (IEN) at Georgia Tech for the constant support in device fabrication and characterization (particularly David Tavakoli, Dr. Hang Chen, Dr. Mikkel Thomas, Dr. Chris Yang, Charlie Turgeon, Todd Walters, Walter Henderson, Charlie Suh, Eric Woods, Scott Fowler, and Gary Spinner)**.**

I sincerely appreciate the following funding agencies: (a) the joint funding from the National Science Foundation and Department of Energy for the QESST ERC and (b) DOE ARPA-e program from the Department of Energy FOCUS program. To all these agencies, thank you for providing the resources to conduct research.

I have been extremely fortunate to be able to count on the support from my cousins during my stay in Arizona. Finally, I would not be where I am today without my parents' constant guidance, unconditional support, and love.

TABLE OF CONTENTS

Page

LIST OF TABLES

Table Page

LIST OF FIGURES

Figure Page

Figure Page

Figure Page

Figure Page

Figure Page

Figure Page

Figure Page

CHAPTER 1

MOTIVATION

1.1. Introduction

As civilization becomes more dependent on energy, introducing a source which is environmentally friendly and economically efficient is crucial. Power from traditional resources such as coal, natural gases, and oil is limited and produces environmental and ecological footprints (such as greenhouse gases). This makes renewable energy a viable option to the ever-increasing demand for energy and reduces the fossil-fuel-based energy byproducts. Among all the renewable energy sources, solar power is the fastest-growing source worldwide, currently accounting for more than two-thirds of net new renewable energy capacity globally [1]. Photovoltaic (PV) systems are highly reliable, environmentally friendly, and easy to install. Consequently, PV technologies are in a state of constant demand and innovation, making the solar industry one of the most competitive fields. In order to accelerate the adoption of PV technologies in markets such as rooftop and utility-scale solar farms, using more efficient, cost-effective, and environmentally friendly solar cells are required. Therefore, it is necessary to develop and commercialize alternative solar cells which can surpass the performance of multi-crystalline silicon (Si) solar cells, which have shown module efficiencies of around 19% in the field [2].

Multi-junction (MJ) solar cells are good options for the next generation of solar cells as they have demonstrated high efficiencies up to 46% (AlInGaP/GaAs/InGaAs/Ge with bandgaps of approximately 1.9/1.4/1.0/0.7 eV, respectively, under the concentration of 508 suns) [2]. Further efficiency improvement is predicted by optimizing the bandgap of the subcells for an efficient carrier collection. However, this necessitates accessing materials with bandgaps covering the entire solar spectrum. Based on the detailed balance

calculation, the optimum bandgaps for three- and four-junction solar cells under 500x AM1.5G concentration are 0.9/1.3/1.8 eV and 1.9/1.4/1.0/0.5 eV, respectively. However, growing materials with these bandgaps is challenging as they usually introduce a high density of extended defect in the solar cell structure due to the strain relaxation leading to a dramatic reduction of cell efficiency. Generally, materials with high bandgaps have lower lattice constants, whereas materials with low bandgaps have higher lattice constants. Thus, introducing new growth techniques (such as metamorphic growth, wafer bonding, and transfer printing) or an alloy that can cover the entire solar spectrum is necessary.

Most of MJ solar cells suffer from the poor long-wavelength response, due to the unavailability of narrow bandgap materials (other than Ge) lattice matched to the conventional substrates (*e.g.*, InP and GaAs) used in the high-efficiency MJ solar cells. Thus, the use of narrow bandgap materials, such as Sb-based alloys while using GaAs-based upper cells can dramatically improve the carrier collection efficiency at long wavelengths. In this work, we evaluate the viability of GaSb-based solar cells grown via molecular beam epitaxy (MBE) for future MJ solar cells by demonstrating an alternative growth metamorphic growth method, in which high-quality GaSb layers are grown on the GaAs substrate. A fabrication process, as well as device characterization, will be discussed.

Another alloy that can be used for MJ solar cells is indium gallium nitride (InGaN). III-nitride-based semiconductors have been demonstrated to be good candidates for high-efficiency PV applications due to their unique inherent properties [3]. The InGaN alloys (with bandgaps of 0.64 to 3.42 eV) can cover the entire visible solar spectrum, which potentially can introduce lower defect density compared to the conventional metamorphic MJ solar cells, and reduce the fabrication complexities. In addition, the available

infrastructures designed for nitride-based LEDs, laser diodes, and power electronics can be used to develop the InGaN-based solar cells. However, to fully utilize the InGaN for PV applications, substantial progress in crystal growth, device fabrication, and system design is necessary. This work presents the details of growth, material characterization, device fabrication, and device performance of single-junction InGaN solar cells for space applications, concentrated solar power (CSP), and photovoltaic hybrid thermal (PV-T) systems. Correlations between measurement techniques are established, and cell parameters for different device designs are compared.

In general, the MJ solar cells are connected via tunnel junctions (TJs). Tunnel junction can be achieved by a heavily doped pn junction. A low resistance GaSb tunnel junction is achievable due to its low bandgap. However, in order to achieve high-efficiency MJ InGaN-based solar cells, the monolithic formation of low-resistance GaN tunnel junction is necessary. A significant remaining challenge in III-nitride-based devices is the lack of low-resistance contacts to p-type GaN, owing to a low hole carrier concentration (N_A) and a high hole effective mass. Beryllium (Be) was introduced first as a viable p-type dopant; however, Be incorporation is severely limited by the formation of Be_3N_2 [4]. Magnesium (Mg) is one of the main p-type dopants used in III-nitride devices which shows higher solubility and carrier concentration compared to the Be. However, due to the large activation energy of Mg originating from the high effective hole mass of GaN, the hole concentration of p-GaN is much lower than the doping density. It has been shown that the thermodynamic limitation of Mg solubility can be solved by kinetically "trapping" Mg into the lattice structure by the low-temperature metal modulated epitaxy (MME) growth method [5], resulting in metastable supersaturation acceptors. The high hole carrier

concentration achieved via MME makes it possible to obtain low-resistance GaN homojunction tunnel diodes. Thus, in order to develop InGaN MJ solar cells, a low resistance GaN homojunction tunnel diode with a negative differential resistance feature is successfully demonstrated. In addition, enabled by the mentioned tunnel junction, the performance of InGaN single-junction solar cell with tunnel contact is shown for the first time. Finally, a proposed plan for the growth and fabrication of MJ InGaN-based solar cells will be presented.

1.2. Basics of Solar Cell Operation

The first PV effect was observed in 1839 by Alexandre-Edmond Becquerel. He observed the voltage across certain electrodes changes after being immersed in an electrolyte [6]. The first conventional solar cell was fabricated in Bell's laboratory in 1954 by forming a pn junction from silicon with an efficiency of ~6% [7]. After the discovery of the first solar cell, different generations of solar cells with various structures have been reported. The multi-junction solar cell, as the second generation, showed the highest efficiencies with a current record efficiency of ~46% by Fraunhofer Institute [8]. The basic concept of the solar cell can be summarized in two steps: (1) electron-hole pair (EHP) generation and (2) carrier collection by drift and diffusion mechanisms. In step one, the photons that have higher energies than the bandgap of the material will be absorbed and produce EHPs. The photo-generated carriers in the depletion region will then be drifted away by the built-in electric field towards the contacts and those which are generated in bulk, outside the depletion region, will contribute to the photo-current by diffusion. Drift mechanism is dominant in thin-film solar cells, whereas, diffusion mechanism is more important in the thicker solar cells. Recombination mechanisms, such as radiative, non-

radiative (known as Shockley-Read-Hall (SRH)), and Auger in the bulk and surface of the solar cells, lead to carrier loss and eventually a reduction of conversion efficiency. Radiative recombination is dominant indirect bandgap materials, SRH is related to the material degradation and crystalline defects, and Auger is a three carrier mechanism which is important in heavily doped materials.

The solar cell operation can be modeled by a single diode-equivalent circuit with a series resistance (R_s) and shunt resistance (R_{sh}) parallel to the current source and a pn diode. R_s is associated with the resistance of the contacts and quasi-neutral regions (QNRs). R_{sh} is related to the non-radiative recombination centers originated by defects and shunt paths in the bulk and mesa edges. Using the diode equation, one can deduce the current across the load resistance:

$$J = J_{SC} - J_0 \exp\left(\frac{V + IR_S}{nkT} - 1\right) - \frac{V + IR_S}{R_{SH}}. \quad (1.1)$$

The J_{SC} is the short-circuit current density, and the n is the ideality factor of the cell representing the recombination mechanism in the solar cell.

The performance of the solar cell can be characterized by current-voltage measurement under the dark and illumination. The J_{SC} can be found when the voltage across the load is zero. If the series resistance of the cell is negligible, the J_{SC} becomes the photo-generated current. The open-circuit voltage (V_{OC}) can be measured when the junction current is zero (in other words, when the forward bias diffusion current balances out with the photo-current). The maximum generated power density is the product of the maximum current density (J_{max}) and maximum voltage (V_{max}). The FF is simply defined by the ratio of P_{max} and the product of V_{OC} and J_{SC}. Typical values for the FF of the conventional solar cell are

around 70 to 90%. However, the large commercial solar cells have lower FF in the range of 50 to 60% due to the high series resistance associated with the connection of the cells.

1.3. Current Status of Solar Cell Technology

Si-based solar cells are the most widely used technology in the market due to their high-efficiency, low cost, and high reliability with a maximum module efficiency of ~19% for poly-crystalline and 26.6% for mono-crystalline [9]. However, due to the indirect bandgap of Si, the absorbing volume of Si solar cell is a significant portion of the cell cost. Thus, various thin film-based solar cell technologies have been explored such as CIGS, CdTe, amorphous Si (a-Si). The mentioned solar cells have low fabrication costs but lower efficiencies compared to the Si solar cell. Currently, the most efficient solar cell with a low cost that can compete with Si is CdTe with a maximum module efficiency of more than 17%. CdTe technology supplies more than 5% of the market (mostly solar farms). The highest efficiency of single-junction solar cells is ~28.8%, based on GaAs [9]. However, due to the high fabrication cost of GaAs, it is predominantly used for space and concentrated PV applications.

1.4. III-Sb-based Alloys for PV Applications

Sb-based compound semiconductors offer numerous advantages for narrow bandgap (E_g) devices including high electron mobility, flexible band alignment, high absorption coefficient, and tunable bandgap [10]. This material system has been typically used for thermo-photovoltaic applications (temperature range of ~1100 - 1400 K, corresponding to ~0.5-0.7 eV, respectively) [11]. However, Sb-based alloys cover a wider range of bandgap values, approximately from 0.1 eV (InAsSb) up to 1.6 eV (AlSb). This flexibility in choosing the bandgap makes this material system uniquely suited for MJ solar cell

applications. In addition, different band alignments, including staggered (type II) and broken (type III) bands, are possible while growing on nearly lattice-matched substrates (*e.g.*, GaSb and InSb).

Bandgaps of AlGaAsSb ($(GaSb)_{1-z}(AlAs_{0.08}Sb_{0.92})_z$) and $In_xGa_{1-x}As_ySb_{1-y}$ can be expressed as [12]

$$Eg(z) = 0.727(1-z) + 2.297z - 0.48Z(1-Z)\ eV, \quad (1.2)$$

$$Eg(x) = 0.725(1-x) + 0.29x - 0.6x(1-x)\ eV.$$

At $z > 14$, the bandgap transits to the indirect. Quaternary III-Sb alloys have two degrees of freedom in tuning the lattice constant and bandgap. The ability to have a lattice-matched system can significantly improve the performance of MJ solar cells. Thus, III-Sb-based solar cells can be good candidates for the development of future high-efficiency MJ solar cells.

1.5. InGaN Alloys for PV Applications

The III-nitride material system has outstanding importance for photonic and electronic devices, second only to silicon in the volume of its many applications. Contrary to the most conventional III-V material groups, III-nitride compounds have an existing mature technology. GaN-based semiconductors have unique properties, such as high breakdown voltage, high thermal conduction, and high saturation velocity, that make them suitable for the use in switching devices. The GaN transistors are functional at high power densities and high switching frequencies, which are more efficient compared to the silicon-based counterparts. The development of nitride-based optoelectronic devices, such as light-emitting diodes (LEDs) and lasers, is expected to expand due to the growing market of solid-state lighting. Furthermore, GaN-based transistors offer a large electric field and high

breakdown voltage. Thus, the existing mature III-nitride technology, including epitaxial growth, fabrication, and characterization, can be used as a leverage for the future InGaN solar cells.

1.5.1. Material Properties

The major advantage of the III-nitride material system over the conventional III-V compounds is its direct tunable bandgap (~0.65 - 3.42 eV) which covers the entire visible solar spectrum, making them suitable for MJ solar cells applications. Band diagrams of GaN, InN, and $In_{0.2}Ga_{0.8}N$ calculated by Fritsch *et al.* and Goano *et al.* are presented in Fig. 1 [13]. The valence band is degenerated in three sub-bands (heavy holes (hh), light holes (lh), and spin-orbit (sh)) due to the crystal field presence and spin-orbit coupling. The effective masses of electrons, hh, lh, and sh around the Γ point of the Brillouin zone are calculated by Rezaei *et al.* for GaN, InN, and AlN (see Table 1) [13].

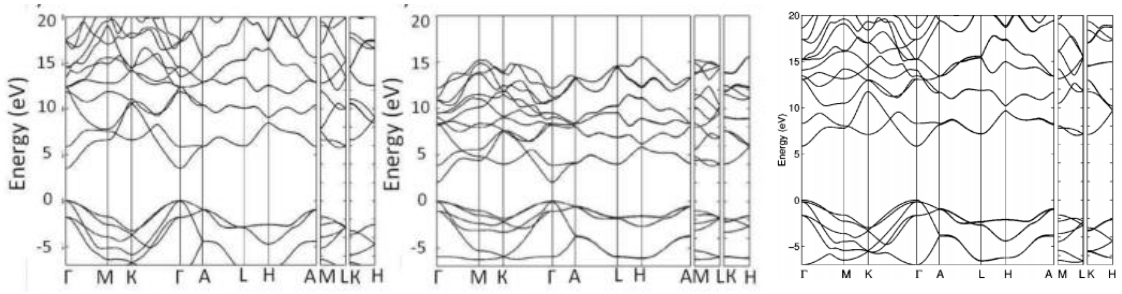

(a) (b) (c)

Figure 1. Band structures of (a) GaN, (b) InN, and (c) AlN [13].

TABLE 1. VALUES OF HOLE AND ELECTRON EFFECTIVE MASSES AT THE CENTER OF BRILLOUIN ZONE (Γ POINT) FOR GAN, INN, ALN [13]. II AND ⊥ ARE PARALLEL AND PERPENDICULAR DIRECTIONS TO C-AXIS. M_0 IS THE ELECTRON MASS (9.11×10^{-31} KG).

	GaN	InN	AlN
m_e^{II}	0.16 m_0	0.12 m_0	0.28 m_0
m_{hh}^{II}	1.45 m_0	1.39 m_0	1.96 m_0
m_{lh}^{II}	1.45 m_0	1.39 m_0	1.96 m_0
m_{ch}^{II}	0.14 m_0	0.1 m_0	0.23 m_0
$m_e^{\perp}$	0.13 m_0	0.11 m_0	0.27 m_0
$m_{hh}^{\perp}$	1.52 m_0	1.41 m_0	2.68 m_0
$m_{lh}^{\perp}$	0.168 m_0	0.12 m_0	0.26 m_0
$m_{ch}^{\perp}$	1.96 m_0	1.69 m_0	2.12 m_0

The temperature dependent bandgap value can be extracted from Varshni's law by [14]

$$\mathrm{E_g(T)} = \mathrm{E_g(0)} + \frac{\alpha \mathrm{T^2}}{\beta + \mathrm{T}}. \tag{1.3}$$

$E_g(0)$ is the bandgap at zero kelvin and α, and β are Varshni's parameters (see Table 2).

TABLE 2. VARSHNI'S PARAMETERS FOR GAN AND INN [14].

	α (meV/K)	β (K)	$E_g(0)$ (eV)
GaN	3.51	0.909	830
InN	0.78	0.245	624

The bandgap of InN, which was first proposed by Tansley *et al.* in 1986, showed a bandgap of 1.9 eV [15], which was revised to 0.9 eV [16] and even further to 0.7 eV at room temperature [17], [18]. It was found that in films grown at low-temperatures, oxygen appeared to form an optically transparent InN–In_2O_3 alloy, resulting in a larger absorption edge. However, in films grown at high temperatures oxygen, acted as an un-intentional donor, which caused a more considerable absorption edge due to a Burstein–Moss shift [18]. In contrast to the conventional III-V compounds, the bandgap of III-N ternary alloys shows a nonlinear trend as a function of alloy composition. For InGaN, this nonlinearity can be expressed by considering a bowing parameter (b):

$$E_g(In_xGa_{1-x}N) = xE_g(InN) + (1-x)E_g(GaN) - bx(1-x), \quad (1.4)$$

where E_g(InN) = 0.65eV and E_g(GaN) = 3.42eV are the bandgaps of InN and GaN, respectively. Recommended value for the bowing parameter of InGaN alloys is 1.43 eV [19].

As mentioned earlier, several InGaN subcells with different In compositions can be interconnected to form a full-spectrum-response solar cell system. In addition, a high bandgap InGaN solar cell can be used in an InGaN/Si tandem device, which would utilize the low-cost and efficient Si bottom cell. Hsu *et al*. reported that even if the Si (~1.1 eV) is not of highly efficient, such a tandem approach can practically improve the Si cell efficiency [21]. In addition, it is reported that n-$In_{0.4}Ga_{0.6}N$/p-Si with the bandgaps of ~1.8 and ~1.1 eV, respectively, can be an ideal option for the high-efficiency single-junction tandem solar cell as the alignment of n-InGaN conduction band with p-Si valance band provides a low resistance hetero-interface [20]. Due to the high absorption coefficient of InGaN (~10^5 cm^{-1} which is 10x higher than the GaAs), only a few hundred of nanometers is enough to absorb a large portion of the incident light, as opposed to the Si solar cells with indirect bandgap and think absorbers. Other solar cell related properties of InGaN alloys are suitability for high temperature operation, high radiation resistance, and high drift velocity [22], [23].

1.5.2. Material Challenges

In addition to the advantages of InGaN for PV applications, InGaN suffers from numerous material related issues such as lack of lattice-matched substrates, polarizations, low p-type doping, high background doping, phase separation, and hydrogen passivation. Due to the mentioned challenges, experimental studies have shown conversion efficiencies

of just less than ~4% for double heterojunction InGaN/GaN solar cells [24]–[31]. Thus, understanding of the inherent material challenges can pave the way for high-efficiency solar cells.

I. P-type Doping Issue

The most important challenge in the III-nitride-based material system is the low hole concentration and high Mg activation energy. A typical Mg activation energy is around ~170 - 240 meV due to the high bandgap and high hole effective mass of GaN [32], [33]. As the In composition of $In_xGa_{1-x}N$ increases, the residual electron concentration increases from ~10^{16} cm^{-3} (GaN) to ~10^{19} cm^{-3} (InN) [34]. Pantha *et al*. have shown that the background electron concentration increases sharply with an increase in the In composition (x) for $x < 0.5$ and becomes almost constant (10^{19} cm^{-3}) for $x > 0.5$ [34]. A typical hole concentration for p-type doped metalorganic chemical vapor deposition (MOCVD)-grown InGaN with low In content is approximately low 10^{18} cm^{-3} [4], [20]. The hole compensation originates from nitrogen vacancies, oxygen, hydrogen, and impurities acting as donors. As a result, un-doped GaN, InGaN, and AlGaN films usually display a high background donor concentration. In addition, the solubility of Mg is limited due to the formation of Mg_3N_2, which acts as a precipitate. Mg precipitates result in structural deterioration, inversion domains, and cubic inclusions [35], [36] (see Fig. 2). The inversion domain, where the polarity of the film changes, has been observed by excessive Mg-doping of the film [37]. As a result, the high background donor concentration and low solubility of Mg can lead to a low hole concentration, which makes the GaN homojunction Esaki tunnel diode hard to achieve and potentially limits the high-efficiency MJ III-nitride-based solar cells.

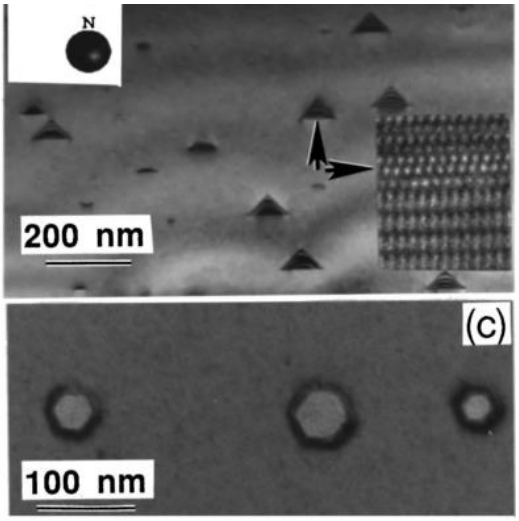

Figure 2. A cross-sectional and plan-view TEM image of an MOCVD-grown GaN: Mg with an Mg concentration of ~5×10^{19} cm^{-3} showing Mg precipitates with pyramidal defects.

At high growth temperatures (*e.g.*, MOCVD), the formation energies of Ga and nitrogen vacancies are low. The nitrogen vacancies (V_N) can form a complex with Mg_{Ga} (Mg substitutes in the Ga sites). As a result, V_N acts as a donor which results in self-compensation of Mg [37]. Thus, under a typical high temperature growth of MOCVD (*e.g.*, ~1100 ºC for GaN), the Mg is heavily compensated, leading to low hole concentrations. Nevertheless, recent efforts have mitigated this thermodynamic limitation by controlling the kinetics of Mg incorporation using a low-temperature growth method via MBE with a shuttering procedure [24]. By utilizing the low growth temperature method which led to high hole concentrations exceeding ~6×10^{19} cm^{-3} [25], it offers great promises for future MJ solar cells and tandem devices.

II. Polarization Effect

III-nitride material system exists in wurtzite, zinc blende, and rocksalt crystalline structures. Among all, the wurtzite structure is the most thermodynamically stable configuration as it can be achieved via MBE, hybrid vapor phase epitaxy (HVPE), and MOCVD. The wurtzite structure of space group P63mc lacks the centrosymmetry and

possesses ionicity between covalent metal and nitrogen bond, leading to an inherent spontaneous polarization (P_{SP}). In other words, the higher electronegativity of nitrogen compared to the metal atom leads to electrostatic dipole moment between the metal and nitrogen atoms. This leads to change in the properties of the film grown in [0001] and [000$\bar{1}$] directions such as surface morphology, dislocation density, growth condition, and chemical stability [40], [41]. In addition to the P_{SP}, the mechanical strain can change the position of the atoms and lattice matrix creating piezoelectric polarization (P_{PZ}) in the wurtzite structures. P_{PZ} depends on the pyroelectric coefficients of the material and strain tensor. The values of P_{SP} and P_{PZ} of the binary III-nitrides are reported by Bernardini *et al.* [42] and Dreyer *et al.* [43]. The combination of P_{SP} and P_{PZ} results in the presence of sheet charges at the interface and, consequently, an induced electric field. The mentioned interface charges can cause band-bending in heterojunction solar cells (including MQWs) which can reduce the carrier collection efficiency. The electric field induced by the polarization sheet charges in InGaN/GaN MQW structures depends on the In composition in the wells. For indium compositions of 5% and 24%, the electric field values are ~0.5 and 3.5 MV/cm^2, respectively, reported by Hangleiter *et al.* [44]. However, the induced electric field can be used in favor of carrier collection if it is in the same direction as the drift electric field (*e.g.*, in N-polar materials).

For non-polar orientations (*e.g.*, m-direction), where the growth direction is perpendicular to the c-plane, there is no sheet charge and, consequently, no induced electric field.

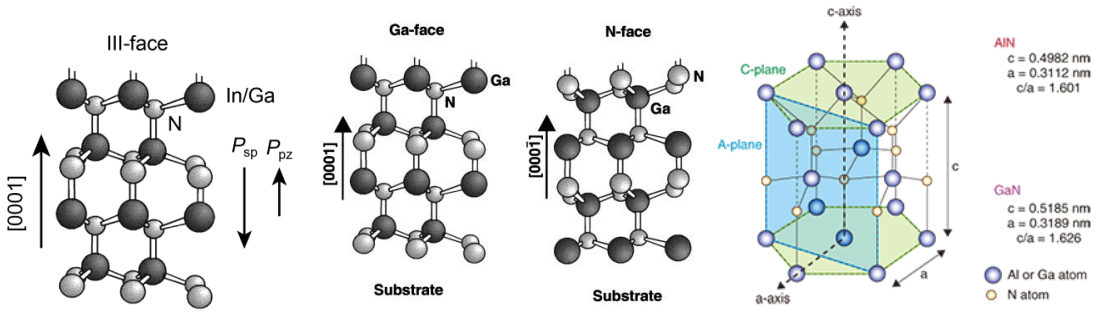

(a) (b) (c)

Figure 3. (a) Wurtzite crystal structure of GaN showing the polarization dipoles. (b) Ga-polar and N-polar GaN. (c) Main atomic planes of binary III-nitrides.

III. Crystal Quality

There are numerous crystal quality issues related to the growth of GaN-based materials, such as lack of lattice-matched native substrates, the lattice mismatch between different compounds, and the related defects originating from them. The conventional substrates for the growth of GaN-based materials are sapphire, Si, and nitride-based templates. The lattice mismatch between GaN and sapphire, Si, and AlN template are 13.9%, 17%, and 2.4%. Si substrate can be used for heterogeneous integration with the conventional III-V subcells. However, Si is highly reactive with group III elements such as Ga and Al. Sapphire is electrically insulating and has high chemical and electrical stability, making it suitable for operation in harsh environments. The lattice and thermal mismatch between the epitaxial layer and the substrate can lead to structural deterioration in the form of threading dislocations (edge, screw, and mixed types), point defects, V-pits, and stacking faults. These defects can form non-radiative recombination (SRH) centers [45], which can act as scattering domains and shunt paths. The SRH centers can lead to a reduction of the minority carrier lifetime and increase in the leakage current [46]. In particular, the high dislocation density can dramatically reduce the diffusion length of the solar cell. The diffusion length is a crucial parameter for solar cells because it affects the collection efficiency. Unlike

conventional solar cells (*e.g.*, Si and GaAs with diffusion lengths in the range of 100-300 μm and 10-50 μm, respectively), the main carrier transport mechanism for carrier extraction in a p-i-n InGaN solar cell is drift by means of the internal electric field in part due to the short minority carrier diffusion length (less than 0.2-0.3 μm) inherent in III-N compounds [47]–[49]. In the case of double heterojunction (DHJ) structures, the internal electric field depends on the doping concentrations, the intrinsic InGaN layer thickness, and the background doping concentration. Although a thick intrinsic InGaN layer, sandwiched between p- and n-GaN layers, can increase the photon absorption, it can lead to the diffusion length reduction due to the strain relaxation. MQW structures can also be used in order to delay the onset of strain relaxation in the InGaN layer. In general, the MQW design allows for a higher In incorporation compared to the bulk, although it is at the expense of lower carrier extraction. Thus, there is a tradeoff between carrier collection (higher In compositions) and carrier absorption (thicker InGaN).

Generally, due to the chemical instability of cation mixing of Ga and In, III-nitride compounds of InN and GaN exhibit an immiscibility gap (In composition of ~20% to ~80%), which leads to the compositional fluctuations (see Fig. 4(a)). This immiscibility gap, which is reported to be due to the significant difference in the interatomic spacing between GaN and InN, was theoretically shown by Ho *et al*. (see Fig. 4(b)) [50]. It is shown that at a growth temperature of 800 °C, the solubility of In atoms in GaN is less than 6%, which introduces a significant challenge in the growth of In-rich InGaN films via MOCVD with significantly higher growth temperatures than that of MBE. Thus, the low-temperature growth of MBE is a suitable candidate for the growth of InGaN throughout the miscibility gap [51].

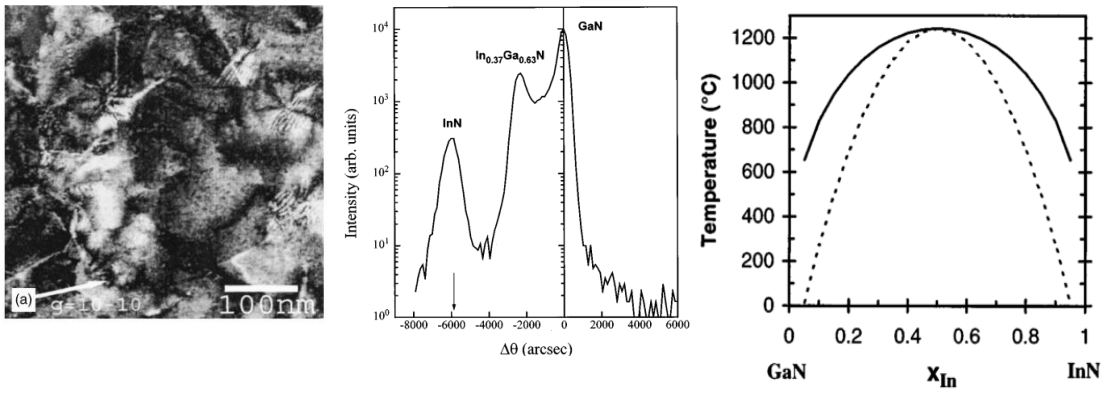

(a) (b) (c)

Figure 4. (a) Dark-field plan view TEM images of $In_{0.12}Ga_{0.88}N$ showing speckled contrast [52]. (b) X-ray diffraction (XRD) data for $In_{0.37}Ga_{0.63}N$ showing the presence of phase separation [53]. (c) Binodal (solid) and spinodal (dashed) curves for the $In_xGa_{1-x}N$ material system [50].

In addition to the intermixing issue of In and Ga, nitrogen incorporation can be a significant challenge. N_2 molecules should be cracked to turn into the active species (suitable for chemical reactions). The active species can be achieved by cracking N_2 by RF-plasma in MBE or thermal pre-cracking of ammonia (NH_3) at temperatures above 450 ºC in MOCVD [54]. The active nitrogen elements such as metastable molecules (N_2^*) and active N atoms have enough lifetimes in such a way that they can impinge on the substrate and contribute to the growth [54].

The growth conditions such as substrate temperature, growth rate, nitrogen and metal fluxes, and plasma species can dramatically change the surface kinetics of the film and eventually, the film quality. For example, if the growth temperature is low and/or the nitrogen flux is higher than the metal flux (nitrogen-rich condition), the surface diffusion of metals reduces as N atoms can act as diffusion barriers leading to columnar and three-dimensional growth and rough surface. In contrary to the nitrogen-rich condition, the metal-rich growth method has higher adatom mobility due to the excess metal species, which leads to the step-flow growth with two-dimensional surface morphology [55].

Unlike Ga and In, which are mobile at typical growth temperatures, the diffusion of N is, by orders of magnitude, slower. As a result, the growth temperature and the III/V ratio should be carefully chosen for efficient incorporation of adatoms into the film [56]. In particular, high temperature can dissociate In-N bonds preferentially leading to the composition fluctuation and carrier localization. The In-N dissociation temperature depends linearly on the In mole fraction [57].

1.5.3. InGaN Solar Cell (state-of-the-art)

The use of InGaN alloys for solar cell applications was first proposed in 2003 after the revision of InN bandgap [58]. Yang *et al.* and Jani *et al.* experimentally demonstrated InGaN solar cells for the first time in 2007 [25], [59]. The two main proposed structures are heterojunction and homojunction. Heterojunction cells can be categorized into single and double heterojunctions and multi-quantum wells.

I. Homojunction Devices

Homojunction solar cells with the structures of n-InGaN/p-InGaN and n-InGaN/i-InGaN/p-InGaN are appealing because there exists no piezoelectric polarization and band bending at the interface. However, due to the lack of native InGaN substrates, the crystal quality of thick InGaN in homojunction solar cells are generally inferior to those in heterojunction solar cells sandwiched by p- and n-GaN layers. In addition, achieving high hole concentrations in InGaN films with high In contents is difficult. Multiple groups have successfully demonstrated InGaN homojunction solar cells with different In contents. The comparison of these devices, which have different bandgaps can be made by quoting their W_{OC} (bandgap-voltage offset) values. However, a complication arises from using different illumination sources to measure the I-V characteristics. The reported illumination sources

have different classes to replicate the AM1.5G spectrum while others are UV-deficient, monochromatic, and UV-enhanced lights. Yang *et al.* have reported the p-$In_{0.18}Ga_{0.82}N$/n-$In_{0.15}Ga_{0.85}N$ grown via MOCVD with a V_{OC} of 0.43 V, J_{SC} of 3.4×10^{-2} mA/cm^2, and fill factor (FF) of 57% under a 360 nm illumination [59]. Such a low J_{SC} value is due to the use of the monochromatic illumination source. Although it is expected that the J_{SC} increases with increasing the In content (better utilization of solar spectrum), the J_{SC} and, consequently, the V_{OC} reduce mostly due to the low hole concentration of InGaN layers. At high In contents, the critical thickness of the film reduces to a few monolayers [60]. Misra *et al*. reported a high In content (~31%) solar cell grown via MBE with a photovoltaic response (V_{OC} of 0.55 V and J_{SC} of 0.24 mA/cm^2 under AM0 illumination) [61]. The highest reported In content pn homojunction solar cell has an In content of ~39% with a poor PV response [62].

II. Heterojunction Devices

The high-performance InGaN solar cells have heterojunction structures (single and double heterojunction and MQW). Jani *et al.* have reported the first p-i-n DHJ cell with a V_{OC} of 2.4 V and quantum efficiency of 60% grown via MOCVD [25]. In addition, Jani *et al.* have shown a single heterojunction (SHJ) solar cell (p-GaN/p-InGaN/n-InGaN) grown via MOCVD on sapphire with a V_{OC} of 2.1.0 V and corresponding W_{OC} of 0.4 V (bandgap of 2.8 eV) [63]. However, the devices grown on free-standing GaN substrates show better performances. Kuwahara *et al.* have shown that DHJ cell grown on a free-standing GaN substrate has a better series resistance and V_{OC} (efficiency of 1.41%) compared to the same sample grown on a *c*-plane sapphire substrate with an efficiency of 0.98% [64]. A high-efficiency DHJ solar cell is also reported by Matioli *et al.* with an efficiency of 1.57%, V_{OC}

= 2.23 V, FF = 61%, and J_{SC} of 1.59 mA/cm^2 [65]. MQW structures with multiple strained InGaN absorbing layers have shown higher J_{SC} and V_{OC} values compared to the SHJ and DHJ cells. Nevertheless, the V_{OC} values of MQW structures, which is mainly related to the bandgap, are comparable to those of HJ cells. Moreover, the theoretical simulation showed that the MQW is a promising design for PV applications, providing a better compromise between photon-absorption and electronic transport [65]. Farrell *et al.* revealed that the efficiency of ~2.3% could be achieved by roughening of the p-GaN top contact layer of a 30x $In_{0.28}Ga_{0.72}N$/GaN MQW, which extends the external quantum efficiency (EQE) to 520 nm [29]. Young *et al.* demonstrated MQW solar cells with EQE values up to 60%, V_{OC} values up to 2.28 V, FF values up to 80%, and conversion efficiencies up to 2.4%, under one-sun AM0 illumination. Young *et al.* have improved the performance of the $In_{0.2}Ga_{0.8}N$ (3.0 nm)/GaN (4.0 nm) solar cell by utilizing optical trapping techniques (front-side anti-reflective coating (SiO_2/Ta_2O_5) and a back-side dichroic mirror (SiO_2/Ta_2O_5)), showing an efficiency of 3.33% under 30x concentration of AM0 illumination (see Fig. 5(a)) [66]. In addition, there are multiple attempts to grow InGaN solar cells on unconventional substrates, such as *r*–sapphire and Si [67], [68]. However, no significant improvement was reported.

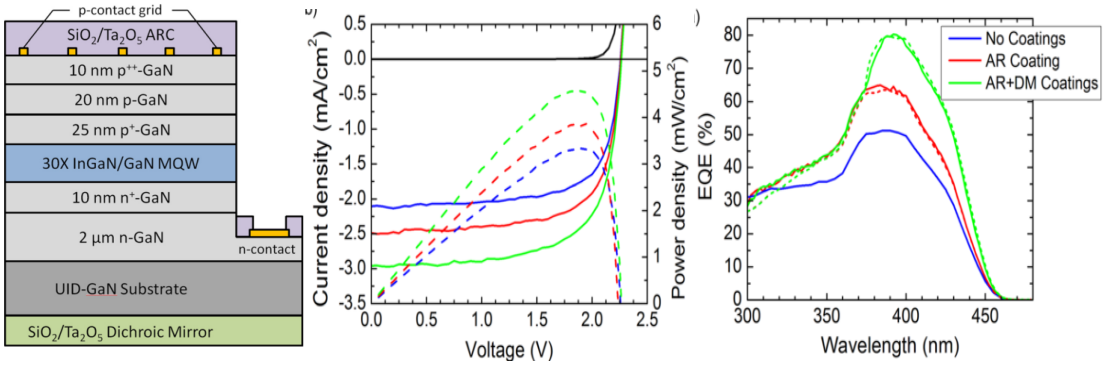

(a) (b) (c)

Figure 5. (a) A device schematic of a 30x $In_{0.2}Ga_{0.8}N$/GaN solar cell [66]. (b) J-V curves under one-sun AM0 illumination. (c) EQE spectra presented by Zhang *et al.* [66].

All the reported conversation efficiencies of InGaN solar cells are quite low due to the use of low In contents, which means that the InGaN solar cell can utilize a small portion of the solar spectrum (short wavelength regime). Thus, the InGaN solar cell, in its current state, can be used as a complement to improve the performance of existing PV systems (such as Si solar cells or photo-thermal hybrid systems (PV-T)).

Due to all the mentioned challenges, achieving high-efficiency InGaN solar cells requires significant progress in the areas of crystal quality with low defect density, high p-type doping, heteroepitaxial growth, and device design. This report seeks to address some of those challenges by using a low-temperature growth method with a shutter technique (MME). This growth method showed high hole concentrations of GaN films (more than 1×10^{20} cm^{-3}) while maintaining good crystal quality. Also, this technique is applied to achieve pn homojunction tunnel diodes to enable tunnel contacted InGaN solar cells and MJ InGaN-based solar cells.

1.6. Molecular Beam Epitaxy

The growth of III-nitride-based films can be achieved by different methods, such as MOCVD, MBE, and HVPE. The MOCVD uses metalorganic gases (*e.g.*, TMGa, TMAl,

and TMIn) as group III precursors and ammonia (NH_3) as the nitrogen supply. MOCVD does not need a low vacuum environment but only high purity gasses to produce pure chemical reactions. The typical growth temperatures are ~1,100 °C for GaN and 475 to 650 °C for InN, which can reach high growth rates (more than 2 µm/h).

Unlike MOCVD, MBE uses solid sources where materials are evaporated and deposited on the substrate. The growth requires an ultra-high vacuum environment (10^{-10} - 10^{-11} Torr) to satisfy the purity of the material (see Fig. 6). MBE growth method allows precise control of layer thickness, interface abruptness, and doping concentration with a lower density of defects. In addition, MBE can be used to grow different nanostructures with good homogeneity and crystalline perfection. Low growth rates and difficulties in maintaining a low vacuum pressure are the main disadvantages of this technique. However, recently, high growth rates (up to ~9.8 um/h) have been demonstrated by MBE, which makes MBE appealing for mass-production [69].

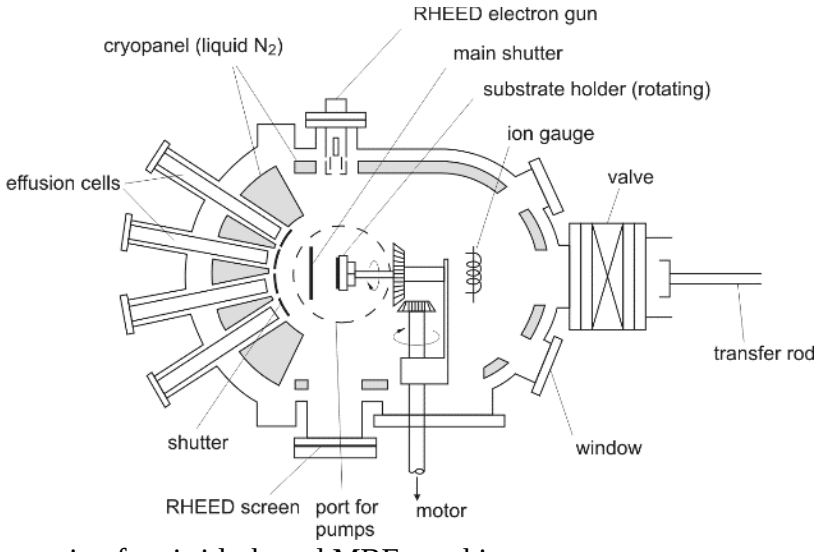

Figure 6. A schematic of a nitride-based MBE machine.

The group-III metal sources and dopants are introduced to the substrate via effusion cells. Veeco PBN tubular crucibles with single and dual filaments were used to evaporate the metals and dopants. It is worth mentioning that the evaporation of Mg can be

challenging. The conical Knudsen evaporator for Mg, which is typically used in MBE, shows less stable fluxes. Thus, in this work, an Sb effusion cell with a valved cracker positioner was modified to be used as the Mg source for better flux stability and Mg incorporation [70].

Two main nitrogen sources in MBE are NH_3 (which is decomposed on the substrate by pyrolysis) and N_2. Active nitrogen can be introduced by two main methods: RF plasma and laser-induced plasma. A few *in-situ* diagnostic methods were used to determine the state of the chamber: pressure sensors, residual gas analyzers (RGA), reflection high energy electron diffraction (RHEED), and thermocouples (TCs). By using the aforementioned methods, various aspects of temperature, chemical composition, pressure, and crystallographic structure can be determined. RHEED consists of a collimated electron beam produced by an electron gun (several microamps with 20 KeV of energy) which is directed towards the sample surface at a glancing angle (few degrees). The diffracted beams, which depend on the crystalline structure of the surface (less than 2 nm depth), are then visible on a phosphorus screen. RGA is a mass spectrometer used to measure the quantities of individual species of a specific gas and can be useful for a vacuum leak check and desorption mass spectroscopy to study the surface kinetics.

The growth of In-rich InGaN films requires a low growth temperature as the dissociation temperature of InN is low, making the MBE growth method appropriate for growing high-quality InGaN films. In order to obtain high quality and single phase InGaN films throughout the miscibility gap via MBE, precise control of growth temperature and III/V are necessary [71]. It is shown that for the growth of high In content InGaN films there exists a significant trade-off between improved crystal quality and compositional

homogeneity at low growth temperatures vs. improved defect densities at high growth temperatures (~600–630 °C) [72]. Metal-rich growth (III/V>1) leads to a 2-D growth mode which results in films with smooth surfaces but with compositional fluctuation and metal droplets on the surface [72], [73]. In contrary, N-rich growth (III/V<1) favors uniform alloy compositions with excellent uniformity and high optical quality with bright band edge photoluminescence but leads to a 3-D growth mode with low adatom mobility [74], [75].

Metal modulated epitaxy (MME) was suggested to utilize both growth methods (metal-rich and nitrogen-rich). MME alternates between N-rich growth and metal-rich growth by shuttering the metals and keeping the nitrogen flux constant. The details of this shuttered technique have been explored in a previous publication [76]. When the metal shutters are opened the metal adlayers form on the surface and then get consumed into the film while the metal shutters are closed (just nitrogen species impinge on the surface). In addition to the high hole concentrations achieved via MME, the MME technique has shown promising advances in the growth of InGaN films throughout the miscibility gap with high material and optical qualities [51], [77].

1.7. Objectives and Scope of the Dissertation

Despite the tremendous advancement in III-V-based PV cells in recent years, significant progress is still needed in the area of high-efficiency PV cells with high (*i.e.*, III-N) and low bandgap (*i.e.*, III-Sb) materials or so-called materials with extreme bandgaps. The mentioned PV cells can be used for high temperature applications such as photovoltaic thermal (PVT) and thermophotovoltaic (TPV) systems. The objective of this research is to realize advances in design, growth, and fabrication for high-efficiency InGaN-based and III-Sb-based solar cells. The research objectives and accomplishments

presented in this dissertation are categorized as follows: in chapter 2, the MBE growth, crystal quality, and device performance of $Al_xGa_{1-x}Sb$ solar cells grown on non-native GaAs substrates are presented. The focus of the work was on the optimization of the growth of $Al_xGa_{1-x}Sb$ on GaAs (001) substrates to minimize the threading dislocation density (TDD) that resulted from a large lattice mismatch between GaSb and GaAs. By utilizing optimum MBE growth conditions, $Al_xGa_{1-x}Sb$ solar cells with different Al compositions are investigated and compared to control cells grown on lattice-matched GaSb substrates. GaSb, $Al_{0.15}Ga_{0.85}Sb$, and $Al_{0.5}Ga_{0.5}Sb$ solar cells grown on GaAs substrates depict open-circuit voltages of 0.16, 0.17, and 0.35 V, respectively. Moreover, the lattice-mismatched cells demonstrate a promising carrier collection with a comparable spectral response to lattice-matched control cells grown on GaSb substrates.

In chapter 3, the performance of $Al_xGa_{1-x}Sb$ (x=0, 0.15, and 0.5) single-junction solar cells over a temperature range of 25–250 °C was explored. The dark current-voltage and external quantum efficiency measurements were acquired at different temperatures. Correlations between numerical and experimental results are made to draw conclusions about the thermal behavior of the cells. It is shown that, although the bandgaps decrease linearly with temperature, leading to a decrease of V_{OC}s, the J_{SC} values decrease with non-linear trends. The temperature-dependence of dark current densities were extracted by fitting the dark I-V curves to single- and double-diode models to give an insight into the effect of intrinsic carrier concentration (n_i) on the performance of the cells. We find that n_i has a significant impact on the temperature-dependent performance of the cells. These results could lay a groundwork for future Sb-based photovoltaic systems that operate at high temperatures.

In chapter 4, the temperature-dependent DC and AC analysis of InGaN/GaN multi-quantum-well (MQW) solar cells with different numbers of quantum wells and barrier thicknesses were investigated. The carrier transport at elevated temperature is shown to be dominated by thermionic emission rather than tunneling but is limited by recombination outside the depletion region. Accurate temperature-dependent AC characteristics of the cells at high injections are presented by implementing an accurate AC circuit model. Correlations between the AC analysis and carrier transport are made to provide insights into optimal cell design.

In chapter 5, GaN and AlGaN homojunction tunnel diodes with different doping profiles at the junctions were investigated. By utilizing heavily doped GaN: Mg films at the junction, various GaN tunnel diodes were prepared to show negative differential resistance (NDR) and Zener characteristics. A tunnel diode with an Mg δ-doped interlayer at the junction shows a high current density of 318 A/cm^2 (~24 A/cm^2) at 1.28 V (-0.1 V), which are the highest reported values for GaN tunnel diodes in the literature. Finally, by using metal modulated epitaxy (MME) growth method to grow a highly doped AlGaN: Mg film, the first AlGaN homojunction tunnel diode with Zenner characteristic is reported.

In chapter 6, the GaN tunnel junctions (TJs) were incorporated to InGaN MQW solar cells to replace the resistive p-GaN contact layers. Extremely high doped GaN p–n tunnel contacts to InGaN solar cells are demonstrated, in which the TJs were grown by MBE on top of active solar cell regions grown by MOCVD. The effects of Mg and Si doping concentrations on characteristics of the solar cells are studied, showing improved turn-on voltage and R_S values. The highest doped solar cell with a tunnel contact has an open-

circuit voltage of ~2.2 V, similar to that of the control solar cell fabricated using indium tin oxide (ITO).

CHAPTER 2

DESIGN AND DEVELOPMENT OF SB-BASED CELLS GROWN ON GAAS SUBSTRATE

2.1. Introduction

Antimony (Sb)-based compound semiconductors have typically been used for TPV applications for temperatures from ~1000 to ~1800 K, corresponding to the bandgaps between ~0.42 to ~0.77 eV [11]. In addition, different band alignments, including type II staggered and broken band, are possible while growing on nearly lattice-matched substrates (*e.g.,* InSb and GaSb).

Sb-based alloys cover a wide range of bandgap values, from approximately 0.1 (InAsSb) up to 2.2 eV (AlAsSb), which makes them suitable for MJ PV applications. MJ solar cells (*e.g.*, InGaP/GaAs/Ge with bandgaps of 1.85/1.4/0.66 eV) suffer from poor long-wavelength response, due to the unavailability of narrow bandgap materials (other than Ge) lattice matched to conventional substrates (InP and GaAs) [78], [79]. Thus, the use of multiple subcells with narrow bandgaps while using GaAs-based upper cells can dramatically increase the carrier collection efficiency (both under one-sun and high illumination) [80], [81]. Table 3 provides optimal bandgaps for the subcells in MJ solar cells, including three- and four-junction solar cells, deduced from detailed balance calculations [82], [83]. Presently, the highest conversion efficiency reported is approximately 46% at a concentration of 508 suns using a four-junction device, consisting of an InGaP/GaAs top stack bonded to an InGaAsP/InGaAs lattice matched to InP [8]. Recently, a five-junction solar cell comprised of a triple-junction GaAs-based cell

mechanically stacked on a dual-junction GaSb/InGaAsSb cell was reported with an implied cell efficiency of 44.5% [84].

TABLE 3. DETAILED BALANCE EFFICIENCIES AND OPTIMUM BANDGAPS (E_G) FOR ONE-SUN AND 500-SUNS SERIES-CONNECTED TANDEM SOLAR CELL.

E_G1 (eV)	E_G2 (eV)	E_G3 (eV)	E_G4 (eV)	E_G5 (eV)	η (%)
1 sun (AM1.5D)					
0.92	1.4	2.02	-	-	51.3
0.69	1.13	1.57	2.15	-	55.3
0.69	1.11	1.41	1.81	2.33	57.7
500 suns (AM1.5D)					
1.57	0.93	-	-	-	47.2
0.93	1.34	1.86	-	-	53.0
0.70	1.04	1.44	1.94	-	56.8

Overall, for higher efficiency solar cells (either under one-sun or concentration), it is beneficial to have materials with bandgaps between 0.4 and 1.6 eV (depending on the number of junctions and the concentration ratio). These materials mainly include InGaN(Sb)As (dilute nitride-based) grown on GaAs substrates and Al(In)GaAsSb (Sb-based) grown on GaSb substrates. Other material systems such as InGaN grown on SiC substrates and InGaAs grown on InP, GaAs, and Ge substrates are also investigated.

Dilute nitrides are promising candidates for additional lower bandgap cells due to their flexible bandgap and ability to be grown lattice-matched to GaAs substrates [85]. Dilute nitride solar cells generally suffer from low minority carrier diffusion length coupled with a narrow depletion width due to defects associated with high nitrogen incorporation [86]. Recent material improvements have led to a high-efficiency lattice-matched solar cell, grown on GaAs, with a dilute nitride subcell (InGaP/GaAs/InGaNAsSb (~1.0 eV)) and efficiency of ~44% [87]. However, achieving even narrower bandgap dilute nitride-based solar cells (E_g < 1 eV) is still challenging, mainly due to difficulties in the incorporation of

Sb and As. Alternative candidates, such as III-Sb, can potentially solve this issue. The narrow bandgap offered by this material system can increase the photon conversion efficiency of multi-junction solar cells for longer wavelengths.

Despite this potential, the growth of Sb-based alloys on lattice-matched GaSb substrates has some disadvantages such as the high cost of GaSb wafers and the lack of good substrate-removal chemistry required for inverted devices [88]. In order to address these issues, Sb-based alloys can be grown on alternative substrates, such as GaAs [89]. There have been multiple approaches to achieve GaSb on GaAs, including wafer bonding and using different metamorphic buffer layers, such as superlattices and compositionally graded layers [90]–[93]. However, these methods are not commercially attractive and can introduce complexity into the device processing.

In this report, we demonstrate an alternative metamorphic method in which high-quality GaSb layers are grown on GaAs. To investigate the potential of such metamorphic technique for the growth of Sb-based subcells, we grew $Al_xGa_{1-x}Sb$ single-junction solar cells on GaAs substrates. $Al_xGa_{1-x}Sb$ absorbers with three Al compositions of 0, 0.15, and 0.50 were chosen based on the optimum bandgaps for multi-junction solar cells from detailed balance considerations [82]. The objective of this study is to compare $Al_xGa_{1-x}Sb$ cells grown on lattice-matched with those on highly lattice-mismatched GaAs substrates.

2.2. Experimental Details

Samples were grown on semi-insulating GaAs (001) substrates using an MBE Veeco GEN III system equipped with As and Sb valved crackers and Ga and Al effusion cells. The crystal quality of GaSb film grown on GaAs was investigated by high-resolution transmission electron microscopy (TEM). High-quality strain-relieved GaSb layer was

grown on GaAs through the formation of interfacial misfit dislocations (IMF) confined to the hetero-epitaxial interface. This method allows instantaneous strain accommodation at the GaSb/GaAs hetero-epitaxial interface without using thick metamorphic buffers. This makes it possible to integrate GaSb-based subcells with GaAs-based cells and take advantage of the long wavelength absorption of GaSb-based active regions. A detailed description of the growth procedure is discussed in our earlier work [94]. Previously, an AlGaSb/GaSb edge-emitting laser has been grown on GaAs with this method and showed promising results, comparable to the devices grown on GaSb substrate [95]. Also, it is shown in this work that using an AlAsSb layer on the GaSb/GaAs can further reduce the TDD.

To investigate the performance of solar cells made with the growth mentioned above methods, two sets of samples with $Al_xGa_{1-x}Sb$ (x=0.15 and 0.50) and GaSb active layers were grown, fabricated, and characterized. The chosen Al mole fractions (x) in the base and emitter are 0.15 and 0.50 for Sample A and B, respectively. Sample A and B were grown on GaAs substrates. The typical device structure is shown in Fig. 7. The $AlAs_ySb_{1-y}$ (y=0.08) layers were used as a back surface field (BSF) and as window layers to reduce the impact of surface recombination on the open-circuit voltage (V_{OC}) and the short-circuit current density (J_{SC}). The GaSb cell (Sample IMF) was similarly grown on a GaAs substrate, except the BSF and window layers were used to investigate the effect of $AlAs_ySb_{1-y}$ as a dislocation-blocking layer on the cell performance. The photovoltaic responses of all the samples were then compared with the same size control cells. The control cells have the same structure as the samples above but were grown on lattice-matched n-GaSb (001) substrates.

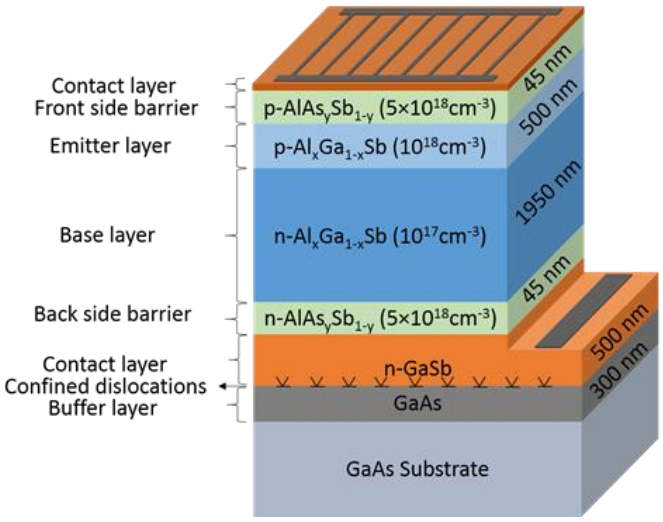

Figure 7. A schematic device structure of an $Al_xGa_{1-x}Sb$ cell grown on a GaAs substrate with a 20 nm GaSb hole-contact layer (x=0.15 and 0.50). GaSb cell (x=0) used in this study has a similar structure except for the front (window) and back (BSF) side barriers.

Rectangular mesas (2.2 mm × 2.8 mm) were defined by photolithography, and an inductively coupled plasma etching process with BCl_3 and Cl_2 gases was used to electrically isolate individual cells. Ti(500 Å)/Pt(500 Å)/Au(3000 Å) and Ni(390 Å)/Ge(590 Å)/Au(233 Å)/Pt(476 Å)/Au(2000 Å) layer stacks were deposited using e-beam evaporation as contacts to p-GaSb and n-GaSb, respectively, and then annealed for 40 seconds at 290 °C under an N_2 rich atmosphere. As depicted in Fig. 7, lateral rear contacts were used for the samples grown on GaAs to avoid contacting the devices through the defective GaSb/GaAs interface. For the samples grown on GaSb, rear contacts were used on the backside of the n-GaSb substrates. Both contacts demonstrated ohmic behavior, measured using transmission line measurement patterns. It is widely known that achieving a low resistivity n-GaSb contact is challenging due to multiple reasons. Elemental Te, used as an n-type dopant, has a high vapor pressure which can cause memory effects and complicated reactions with Ga [96], [97]. In addition, the surface of GaSb exhibits Fermi level pinning near the valence band, causing a broad and high Schottky barrier [98].

Despite these challenges, the n-contact shows a promising resistivity of ~10^{-5} Ω.cm^2 due to the increased activation efficiency of Te dopants by the optimization of the annealing process.

The light J-V characteristics were measured in-house using a continuous Oriel class A solar simulator equipped with a Xenon ARC lamp (AM1.5G). The intensity of the Xenon lamp was adjusted using a Si reference cell to set the lamp intensity equal to one-sun. Also, the external quantum efficiency (EQE) was measured by a PVMeasurements QEX10 equipped with a dual grating monochromator and monochromatic probe light with long wavelength detection capability. Reflection losses were also acquired with a dual-beam spectrophotometer equipped with an integrating sphere.

2.3. Results and Discussion

2.3.1. Crystal Quality

The cross-sectional electron micrograph of the GaSb/GaAs interface illustrates the extent of relaxation and the presence of periodic misfit dislocations, as shown in Fig. 8(a). Figure 8(b) shows that these misfit dislocations are purely 90° dislocations based on the Burgers vector analysis. The interfacial misfit dislocations are spaced at 13 GaSb lattice sites or 14 GaAs lattice sites with a spacing of ~5.5 nm. This spacing of the dislocations is the principal mechanism for the relaxation of the GaSb layer on GaAs [99]. Thus, the presence of misfit dislocations can be attributed to the large lattice mismatch (*f*) between GaSb and GaAs (f=($\Delta a_0/a$)=7.8%), where a represents the lattice constants. The combination of the large lattice mismatch between GaAs and GaSb along with the preference for GaSb on GaAs to undergo spontaneous plastic relaxation results in the creation of pure edge dislocations localized at the interface along the [110] and [1$\bar{1}$0]

gliding vectors with a periodicity of ($|b|/\varepsilon_{xx}$) [100], where b is Burgers vector and ε_{xx} is an in-plane strain. The subsequent growth of GaSb happens after complete relaxation, leading to a lower TDD in the GaSb epilayer. There is, however, a significant density of residual threading dislocations (TDs) despite the formation of the IMF dislocations. The mechanism for the formation of such TDs is attributed to the coalescence of the GaSb islands, with the coalescence point leading to the creation of 60º misfit dislocations that can thread into the GaSb and possibly the subsequent epilayers (such as $Al_xGa_{1-x}Sb$). In the epitaxial growth of Al-containing GaSb on GaSb/GaAs, the small net mismatch between AlGaSb and GaSb causes a slight increase in the TDD. For example, extracted TDD from cross-sectional TEM images of an $Al_{0.15}Ga_{0.85}Sb$/GaSb/GaAs sample (not presented here) depicts values of ~7×10^8 to ~9×10^8 cm^{-2}. The $Al_xGa_{1-x}Sb$ layers could also be grown fully lattice matched to GaSb with the inclusion of arsenic in the alloys; however, we have observed that for the layer thicknesses used, there is not a significant difference between the electrical performance of diodes with $Al_xGa_{1-x}Sb$ layers compared to those with $Al_xGa_{1-x}As_ySb_{1-y}$ layers. This is due to the fact that the $Al_xGa_{1-x}Sb$ layers are predominantly pseudomorphic with some degree of relaxation.

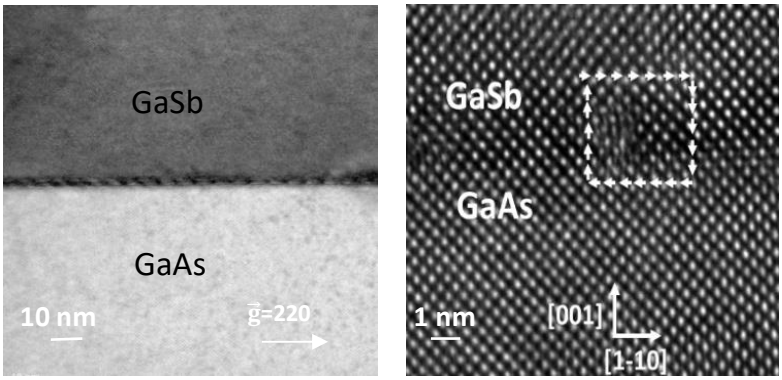

(a) (b)

Figure 8. A two-beam bright-field cross-sectional TEM image of GaSb/GaAs showing interfacial misfit dislocations (IMF) at the GaSb/GaAs interface. (b) A high-resolution TEM image of the GaSb/GaAs interface with a periodic array of Lomer dislocations (the Burgers circuit is shown around the misfit dislocations).

The presence of dislocations has a detrimental effect on solar cell performance by increasing the dark current density (J_0) and reducing the V_{OC} mostly due to non-radiative recombination centers. Therefore, it is beneficial to reduce J_0 by improving material quality. In an effort to do that, the TDD was further reduced by forming an $AlAs_ySb_{1-y}$ layer on top of the GaSb/GaAs interface to prevent dislocations at the $AlAs_ySb_{1-y}$/GaSb interface from propagating to the surface. A similar result was achieved by Katz *et al.* in an InGaSb/AlSb film [101].

In order to study the effect of blocking layer on TDD and establish a range for TDD values, we have prepared three samples with different GaSb buffer layer thicknesses (100, 250, and 500 nm) followed by an $AlAs_ySb_{1-y}$ (y=0) blocking layer grown on GaAs substrate. Figure 9 shows the schematics of the grown samples along with their TEM images. The TDD was calculated from the plan-view TEM images. Further inspection shows that the TDD values measured in this study are highly reproducible. The sample without the AlSb blocking layer (Sample I) has a TDD of 1.3×10^8 cm^{-2}, which is typical for GaSb layers grown on GaAs substrates with arrays of IMF dislocations. Sample II, III,

and IV show that with the insertion of AlSb, the TDD is reduced. This is mainly attributed to the difference in the mechanical stiffnesses of GaSb and AlSb, which controls the propagation of TDs. The net force on the dislocations below the AlSb/GaSb interface is repulsive leading to the prevention of dislocations from being drawn to the surface [101], [102]. In addition, it is evident that as the thickness of the GaSb buffer layer increases to 500 nm the TDD reduces to 3.6×10^{7} cm^{-2} (Sample IV).

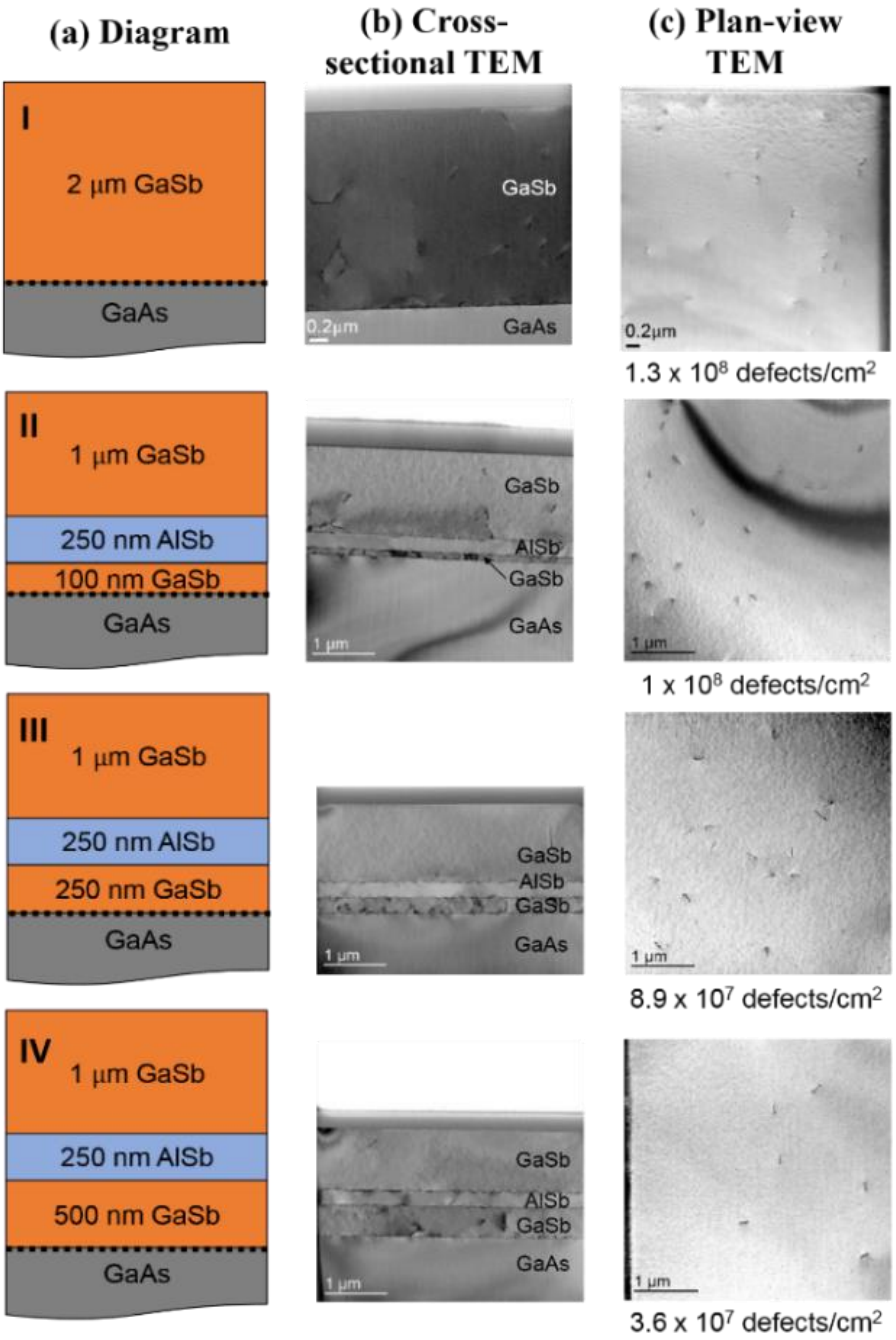

Figure 9. (a) Schematic structures of GaSb grown on GaAs substrates to investigate the effect of AlSb blocking layer on the TDD. (b) Cross-sectional TEM images with $\vec{g}$=(220). (c) Plan-view TEM images.

2.3.2 Device Performance

I. GaSb/GaAs Solar Cell

An additional GaSb/GaAs cell (Sample IMF-BL) was prepared by the inclusion of the $AlAs_ySb_{1-y}$ (y=0) layer on the GaSb/GaAs to study the effect of the blocking layer (BL) on the performance of the GaSb (x=0) cell. As mentioned earlier, the BSF and window layers were not used in the GaSb cells to rule out their effects on the cell performance analysis. The control cell that was grown on the lattice-matched (LM) GaSb substrate has no BL (Control LM).

Figure 10(a) depicts the light J-V, dark J-V, and EQE of the best-performing GaSb cells. Sample IMF (without the BL) shows a V_{OC} of 0.1 V and a J_{SC} of 19.7 mA/cm^2 while Sample IMF-BL exhibits improved V_{OC} of 0.16 V and J_{SC} of 21.7 mA/cm^2 (see Table 4). Although Sample IMF and IMF-BL exhibit shunting issues, it is clear that Sample IMF-BL has higher V_{OC} and J_{SC} values, which can be correlated to its improved crystal quality and fewer SRH recombination centers that resulted from the inclusion of the AlSb BL. The difference in the dark current values also reflects material-related differences between Sample IMF and IMF-BL, see of Fig. 9. The dark current densities of Sample IMF, Sample IMF-BL, and Control LM are ~212, ~48, and ~8 mA/cm^2 at -1.0 V, respectively. The shunt resistances extracted from the dark J-V curves are ~13 and ~100 Ω·cm^2 for Sample IMF and IMF-BL, respectively, indicating a higher recombination rate for the sample without the BL. The combined effects of leakage current and shunting due to the formation of defects have a detrimental effect on the J_{SC} and the V_{OC} of the lattice-mismatched samples. However, these effects are moderated by the implementation of the BL.

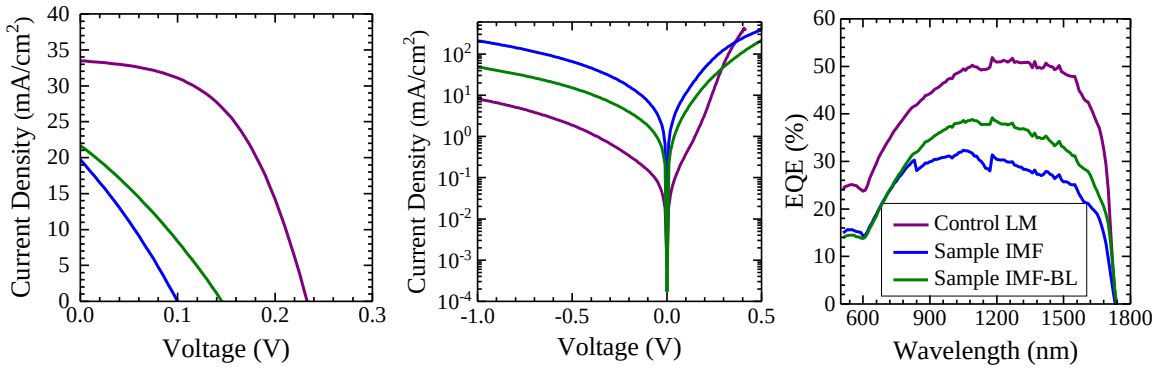

Figure 10. (a) Light J-V, (b) dark J-V, and (c) EQE characteristics of Control LM, Sample IMF, and Sample IMF-BL.

TABLE 4. ELECTRICAL CHARACTERISTICS OF GASB/GAAS SAMPLES AND GASB/GASB CONTROL CELL UNDER ONE-SUN ILLUMINATION.

ID	Substrate	J_{SC} (mA/cm^2)	V_{OC} (V)	FF (%)	η (%)	W_{OC} (V)
Control LM	GaSb	33.5	0.23	50	3.9	0.49
Sample IMF	GaAs	19.7	0.1	29	0.6	0.62
Sample IMF-BL	GaAs	21.7	0.16	28	1.0	0.56

The EQE of Sample IMF-BL is higher than Sample IMF at wavelengths above ~800 nm, indicating carrier collection improvement at long wavelengths. The long wavelength photons can penetrate further into the device and be absorbed near the defective GaSb/GaAs interface. Thus, the increase in the EQE shows that the sample with the BL has a lower density of SRH recombination centers above the GaSb/GaAs interface, which means an increase in the SRH lifetime. At shorter wavelengths, below ~800 nm, most of the loss originates from the surface reflection and absorption in the GaSb capping layer and, as a result, the EQE profiles are similar. However, the samples grown on GaAs have lower EQE values compared to the control cell throughout the studied wavelength range. The difference in the EQE values between the control cell and Sample IMF-BL is less than

~15% throughout the entire wavelength range, which makes further growth optimization of the GaSb/GaAs interface and the BL necessary.

These results show that GaSb-based cell performance can be improved by growing GaSb on GaAs using IMF dislocations and incorporating the AlSb layer as a BL on the GaSb/GaAs layer. By adopting a similar platform and considering the similarities in the material properties of $Al_xGa_{1-x}Sb$ (x=0.15 and 0.50) and GaSb, we expect the AlGaSb cells (Sample A and B) with $AlAs_ySb_{1-y}$ (y=0.08) layers to have TDDs in the range of 5×10^7 to 5×10^8 cm^{-2}, depending on the Al content (x) and thicknesses of the $AlAs_ySb_{1-y}$ and GaSb buffer layers. It is worth mentioning that the analysis of the $Al_xGa_{1-x}Sb$/GaSb/GaAs structures using plan-view and cross-sectional TEM images resulted in unreliable TDD counts mainly due to oxidation of the Al-containing layers during sample preparation. The mentioned $AlAs_{0.08}Sb_{0.92}$ layer on top of the GaSb (500 nm)/GaAs stack acts as a BL and a backside barrier. The device performance of AlGaSb/GaAs solar cells is discussed below.

II. AlGaSb/GaAs Solar Cell

Figure 11 and Table 5 show electrical characteristics of $Al_xGa_{1-x}Sb$ cells (x=0.15 and 0.50). Control cells have bandgap-voltage offsets (W_{OC}) of 0.49 and 0.85 V for the 15% and 50% Al contents, respectively. Sample A and B have higher W_{OC} values of 0.68 and 1.05 V—higher than the 0.4 V W_{OC} that is characteristic of mature technologies [103]. The increased W_{OC} with increasing Al composition is most likely due to increased point defects and/or dislocations. Moreover, the transition from GaSb to GaAs substrate results in increasing W_{OC} given the recombination-active nature of defects in lattice-mismatched solar cells. The effect of transitioning from GaSb to GaAs substrate results in a reduction

of J_{SC} by 5% to 10%. This could be due to the reduced shunt resistances of Samples, as their slopes at short circuit are significantly higher than their Control counterparts.

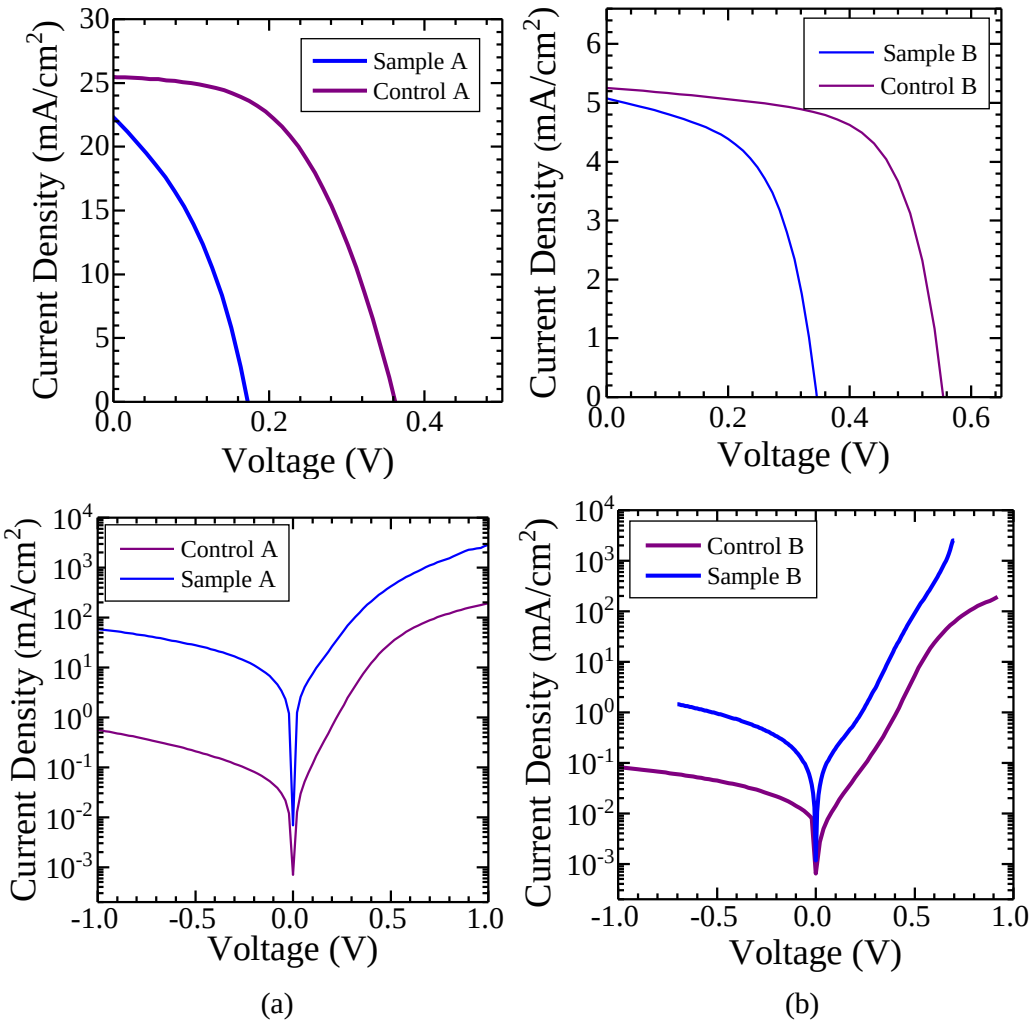

Figure 11. Light and dark J-V characteristics of the solar cells: (a) $Al_{0.15}Ga_{0.85}Sb$ and (b) $Al_{0.5}Ga_{0.5}Sb$.

TABLE 5. ELECTRICAL CHARACTERISTICS OF $AL_XGA_{1-X}SB$/GAAS SAMPLES AND $AL_XGA_{1-X}SB$/GASB CONTROL CELLS UNDER ONE-SUN ILLUMINATION.

ID	Al (%)	J_{SC} (mA/cm^2)	V_{OC} (V)	FF (%)	η (%)	W_{OC} (V)
Sample A	15	22.7	0.17	37	1.43	0.68
Control A	15	25.5	0.36	52	4.76	0.49
Sample A	50	5.1	0.35	54	0.97	1.05
Control B	50	5.2	0.55	66	1.19	0.85

The EQE and corresponding loss mechanisms of all the cells are depicted in Fig. 12. Control cells demonstrate higher EQE compared to their Sample counterparts. Peak EQE values for Sample A and B are ~30% and ~13%, respectively, while Control A and B have peak EQE values of ~35% and ~20%, respectively. The difference in EQE caused by the Al composition could be due to decreased absorptivity in the indirect band $Al_{0.5}Ga_{0.5}Sb$, [12], and reduced minority carrier lifetime. It is shown that the top surface reflection losses make up the majority of the optical losses, as these devices had no antireflection coating. In the short-wavelength range, the 20-nm-thick GaSb cap absorbs most of the remaining light. This absorption loss is calculated based on the extinction coefficient data provided by Ferrini *et al.* [104]. The GaSb capping layer was not chemically etched, due to the strong oxidation and roughening of the $AlAs_{0.08}Sb_{0.92}$ etch-stop window layer during the wet-etch process [105]. Parasitic losses account for other loss mechanisms, which are mostly transmission loss and loss of generated carriers due to recombination, mainly in the absorber.

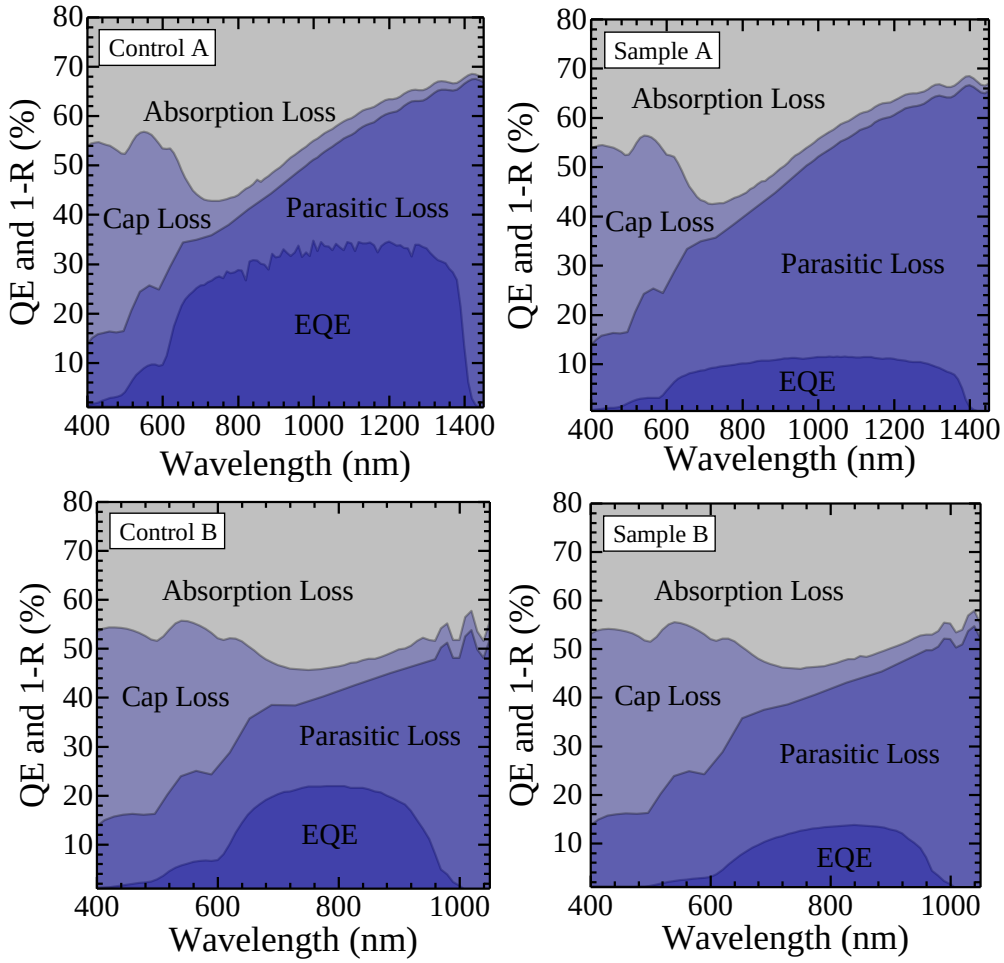

Figure 12. EQE and total absorbance (1-reflectance) of Sample A and B and Control A and B. Colored areas denote distinct current loss mechanisms.

To further study the effect of dislocations on the solar cell performance, the dark J-V characteristics were fit with a single-diode model. The fitting parameters of the $Al_{0.15}Ga_{0.85}Sb$ cells are presented in Table 6 (the results of the $Al_{0.5}Ga_{0.5}Sb$ cells are not presented here). The slopes at the short circuit of Control A and Sample A were fit with R_{SH} of ~15.10 and ~0.06 $K\Omega \cdot cm^2$, respectively, which indicate that the performance of the lattice-mismatched cell is limited by shunting (SRH recombination centers in bulk). The slopes around the open circuit of Control A and Sample A correspond to series resistance (R_S) values of 1.7 and 0.7 $\Omega \cdot cm^2$, respectively, suggesting the existence of carrier transport issues in both cells. Suns-V_{OC} measurement of Control A confirms this finding, as the

pseudo-fill factor (FF_0≈60%) is larger than the device fill factor (FF≈52%). This FF loss may originate from poor passivation at the $Al_xGa_{1-x}Sb/AlAs_{0.08}Sb_{0.92}$ interfaces, contact resistance, and high sheet resistance of the n-GaSb contact layer. The difference between the series resistance values is small; thus, the R_S cannot be the main contributor to the lower performance of Sample A. The ideality factors (n) of Sample A and Control A show values of 1.2 and 1.7, respectively. The low ideality factor is mostly attributed to the SRH recombination (limited by minority carriers). The dark current densities of Sample A and Control A, which quantify the minority carrier recombination in bulk and at the surface, were extracted to be 3.2×10^{-5} and 1.2×10^{-7} mA/cm^2, respectively. The differences in the J_0 and R_{SH} values of these two solar cells strongly suggest that the main limiting factor in the V_{OC} and efficiency (η) is the recombination centers, acting as shunting paths.

TABLE 6. SINGLE-DIODE PARAMETERS OF SAMPLE A AND CONTROL A EXTRACTED FROM THE DARK J-V CURVES.

ID	J_0 (mA/cm^2)	n	R_S (Ω.cm^2)	R_{Sh} (Ω.cm^2)
Sample A	3.2×10^{-5}	1.2	0.7	0.06
Control A	1.2×0^{-7}	1.7	1.7	15.10

Capacitance-voltage (C-V) measurements were performed (not shown here) to calculate the depletion-region widths of the $Al_{0.15}Ga_{0.85}Sb$ solar cells, which show both cells are fully depleted. Thus, the dark current density (J_0) can be represented (based on the Sah-Noyce-Shockley theory) by [45]:

$$J_0 = qn_iWD/2L^2, \quad (2.1)$$

where n_i is the intrinsic carrier concentration, W is the depletion width, D is the diffusion coefficient of the n-GaSb layer (because most of the depletion region is in the n-GaSb base layer), and L is the effective minority carrier diffusion length. By assuming that the diffusion length is recombination limited, the resulting L can be expressed as [106]

$$L = \sqrt{4/(\pi^3 N_d)}, \tag{2.2}$$

where N_d is the average dislocation density. Finally, the V_{OC} can be calculated by

$$V_{OC} = (nkT/q)\ln[J_{SC}/J_0 + 1]. \tag{2.3}$$

Based on the reported empirical data [12] and assuming a TDD of ~5×10^8 cm^{-2} for $Al_{0.15}Ga_{0.85}Sb$ on GaAs substrate and an ideality factor of 1.2, the V_{OC} is calculated to be ~0.2 V, which is close to the V_{OC} extracted from the light J-V curve of Sample A. However, the efficiency is expected to increase as the crystal quality improves through reduction of the TDD, as were experimentally demonstrated with GaAs-based solar cells grown on Si by Onno *et al.*, [44], and Yamaguchi *et al.* [107], [108]. For example, by reducing the TDD to 5×10^6 cm^{-2}, which is a projected realistic limit for metamorphic structures with high lattice-mismatches, the V_{OC} can be increased to ~0.35 V (assuming the same ideality factor).

In addition to the TDD reduction, the cell performance can be further improved by reducing the optical losses, particularly the reflection loss. In order to reduce the reflection loss highly transparent textured polydimethylsiloxane (PDMS) layers were applied to the top surface of the cells (on top of the metal fingers). The PDMS layers carried a random-pyramid texture, with characteristic feature sizes of approximately 5 µm, copied from an alkaline-etched silicon wafer using UV-nanoimprint lithography (UV-NIL) technique. The PDMS layer acts as an antireflection coating in two ways. First, incident light is scattered downward as it undergoes multiple hits at the random pyramid facets, thus improving in-coupling of the light. The random base angle, positions, and height of the pyramids provide excellent light trapping, as demonstrated in our earlier work [109]. Second, the PDMS layer has a favorable refractive index (n=1.42) that reduces the refractive index contrast between

the $Al_xGa_{1-x}Sb$ solar cell and air [110]. The PDMS scattering layers were attached to the top of the devices using index-matching fluid. Complete details of the preparation methods of the PDMS scattering layer used in this work are discussed elsewhere [111]. Figure 13 shows EQE and 1-R spectra of $Al_{0.15}Ga_{0.85}Sb$ devices, with and without the PDMS scattering layer. Table 7 shows the measured light J-V parameters of the $Al_{0.15}Ga_{0.85}Sb$ cells with the PDMS layers ($Al_{0.5}Ga_{0.5}Sb$ samples are not discussed here). For both Sample A and Control A, the reflectance loss reduced from 29.5 mA/cm^2 without the PDMS scattering layer case to 15.4 mA/cm^2 with it. With the reduction in reflectance, there is extra 14.1 mA/cm^2 to be gained in terms of $J_{SC,}$ but we note that the J_{SC} of Control A improved from 25.5 mA/cm^2 to 31.0 mA/cm^2, which is only 5.5 mA/cm^2 improvement. The rest of the 8.6 mA/cm^2 contributes to parasitic loss as seen from the EQE and 1-R plots in Fig. 13. Similarly, Sample A shows only 15% enhancement in its J_{SC}. The increase in the J_{SC} was not accompanied by an increase in the V_{OC} and FF for both Sample A and Control A.

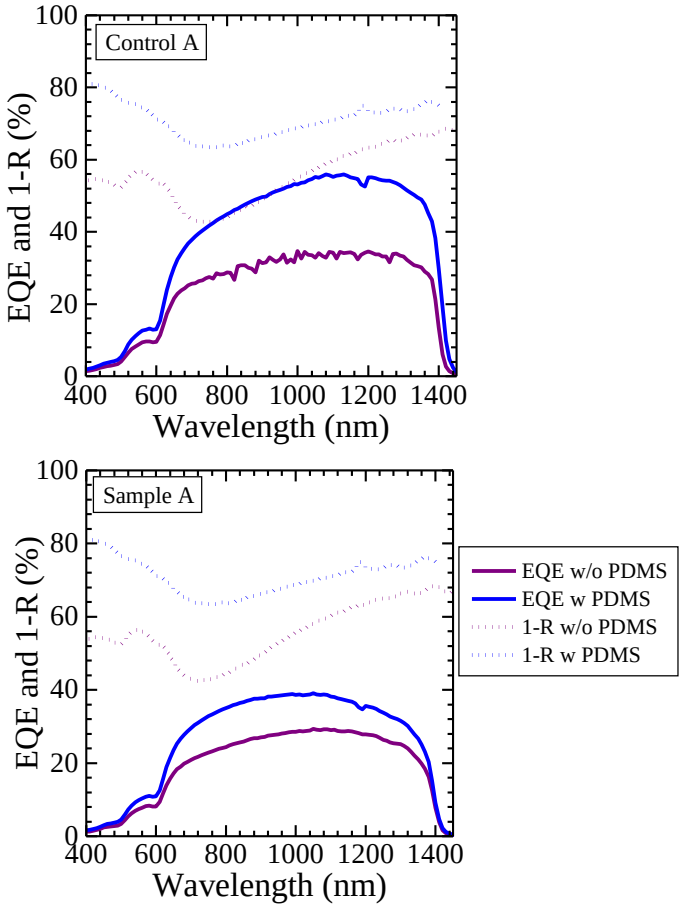

Figure 13. EQE and total absorbance (1-reflectance) of the $Al_{0.15}Ga_{0.85}Sb$ samples with and without the PDMS scattering layers. "w/o" stands for "without" and "w" stands for "with".

TABLE 7. LIGHT J-V CHARACTERISTICS OF THE $AL_{0.15}GA_{0.85}SB$ DEVICES WITH THE PDMS SCATTERING LAYERS.

Sample ID	J_{SC} (mA/cm^2)	V_{OC} (V)	FF (%)	η (%)	W_{OC} (V)
Sample A	26.1	0.18	38	1.78	0.67
Control A	31.0	0.38	54	6.36	0.47

2.4. Conclusion

The growth, fabrication, and electrical characterization of $Al_xGa_{1-x}Sb$/GaAs solar cells with 0, 0.15, and 0.50 Al contents have been demonstrated. Although the crystal deterioration and the high density of SRH recombination centers limit the performance of solar cells, the highly lattice-mismatched devices show photovoltaic responses comparable to that of the lattice-matched devices. This improvement was achieved by optimizing the

growth conditions of GaSb on GaAs and implementing the $AlAs_ySb_{1-y}$ dislocation-blocking layer on the GaSb/GaAs layer, which led to low TDDs and, consequently, increased V_{OC} values.

CHAPTER 3

TEMPERATURE DEPENDENCE OF ALGASB SOLAR CELLS

3.1. Introduction

There are different photovoltaic-based systems that operate at elevated temperature regimes, such as photovoltaic-thermal (PV-T) hybrid solar collectors and thermophotovoltaic (TPV) systems. The PV-T system can utilize both electrical and thermal collectors to provide dispatchable energy storage [112]. In most of the high-efficiency solar cell cells, a high portion of incoming photons will be dissipated into heat. Thus, introducing an efficient PV-T system requires the development of cells that can absorb photons in the long wavelength regime (near-IR) and operate at high temperatures with long-term durability. Sb-based alloys offer a wide range of tunable bandgap values, ranging from ~0.1 to ~1.6 eV, which makes them suitable for high-temperature multi-junction bottoming cells to increase the carrier collection efficiency through extending the absorption band edge [113], [114].

TPV systems are prominently designed to convert thermal radiation into electrical power. The cells used in TPV systems are typically exposed to high temperatures, where the cells are separated by an optical filter (such as glass or quartz tubes) from a radiator operating at temperatures (T) between 1100 to 2200 K which corresponds to emission wavelengths of ~1.3 to ~2.6 μm) [115]. There are numerous experimental studies showing efficiencies of ~1 to ~11% for TPV systems at room temperature [116], [117]. However, Yugami *et al.* have shown that the maximum theoretical efficiency of ~24% is achievable [118]. Sb-based alloys, such as GaSb, are among the narrow bandgap (E_g) materials with the potential to

achieve high efficiencies in TPV systems due to their high absorption coefficient, high radiation resistance, and low effective electron mass [119], [120], [121].

The development of GaSb-based PV cells for the mentioned applications requires an understanding of the limiting factors in the device performance at high temperatures. For example, the performance of solar cells degrades as temperature increases, mainly due to the reduction of open-circuit voltage (V_{OC}) originating from an increase in the dark current density (J_0) [14], [122], [123]. In addition, long-term durability can introduce more challenges in designing cells that can operate at high temperatures. Thus, it is important to carefully investigate the effect of temperature on cell parameters to be able to develop efficient PV-T and TPV systems.

This work investigates the thermal robustness and temperature-dependent behavior of GaSb and Al-containing GaSb single-junction PV cells. First, building on the work of Fraas *et al.*, we discuss the mechanisms which derive the temperature-dependent V_{OC}, short-circuit current density (J_{SC}), and fill factor (FF) of the GaSb cell [124]. Second, numerical device simulation of the GaSb cell at different operating temperatures is carried out to assess the experimental results. Finally, we study the effect of temperature on wider bandgap $Al_xGa_{1-x}Sb$ cells with two Al mole fractions of 0.15 and 0.50. $Al_xGa_{1-x}Sb$ can be used for multi-junction solar cell applications and can serve as a window or back surface field (BSF) layer in narrow bandgap Sb-based cells.

3.2. Experimental Details

$Al_xGa_{1-x}Sb$ single-junction cells (x = 0, 0.15, and 0.50) were grown using a molecular beam epitaxy (MBE) system equipped with Sb and As valved crackers and Ga and Al effusion cells. First, a 500-nm-thick homo-epitaxial GaSb layer was grown at 485 °C on

an n-GaSb (001) substrate that was previously deoxidized under Sb_2-rich flux. The BSF layer consists of a 45-nm-thick Te-doped n-$AlAs_{0.08}Sb_{0.92}$ layer grown on the n-GaSb buffer layer. The active pn region was subsequently grown, consisting of a 1950-nm-thick n-$Al_xGa_{1-x}Sb$ base layer and a 500-nm-thick p-$Al_xGa_{1-x}Sb$ emitter layer. After the active region, a Be-doped 45-nm-thick p-$AlAs_{0.08}Sb_{0.92}$ was grown as the window layer. Finally, the structure was capped with a highly p-doped GaSb contact layer with a thickness of 20 nm. The carrier concentrations in the n- and p-$AlAs_{0.08}Sb_{0.92}$, p-$Al_xGa_{1-x}Sb$, and n-$Al_xGa_{1-x}Sb$ layers were 5×10^{18}, 1×10^{18}, and 1×10^{17} cm^{-3}, respectively. $AlAs_{0.08}Sb_{0.92}$ layers were used to reduce the surface recombination through carrier confinement. Al compositions of 0, 0.15, and 0.50 were chosen based on the optimum bandgaps for multijunction solar cells deduced from detailed balance calculations [82]. A detailed description of the growth procedure used in this work is discussed elsewhere [113]. It is worth mentioning that the growth temperatures used, in this work, were above the operating temperatures (25 - 250 °C), where the thermal stability of the cells was tested. The schematic structure of the cells is shown in Fig. 14.

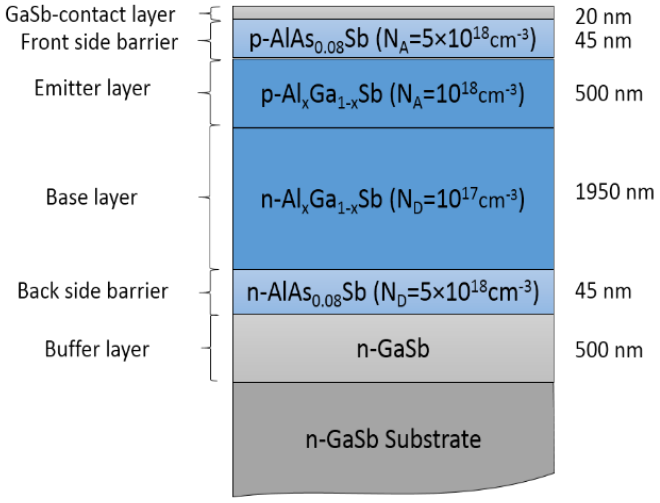

Figure 14. A schematic device structure of a $Al_xGa_{1-x}Sb$ cell grown on a GaSb substrate with a 20-nm-thick p-GaSb hole-contact layer on top (x = 0, 0.15, and 0.50).

Although both n-on-p and p-on-n structures are feasible, the p-on-n configuration is preferable. There are major differences between these two configurations, such as absorption coefficients, carrier transport, and minority carrier lifetimes. For example, the free carrier absorption in p-GaSb is higher than the n-GaSb, leading to a higher parasitic loss in the substrate and base region [120]. Thus, the n-GaSb substrate was used to increase the upper limit of operating temperature by reducing the possible parasitic losses.

The grown structures were fabricated into cells by defining mesas (0.5×0.5 cm^2) using photolithography and inductively coupled plasma etching processes. Ni(390 Å)/Ge(590 Å)/Au(233 Å)/Pt(476 Å)/Au(2000 Å) and Ti(500 Å)/Pt(500 Å)/Au(3000 Å) contact layer stacks were deposited using e-beam evaporation as contacts to n-GaSb and p-GaSb layers, respectively. No antireflection coating or current spreading layer was used. Contacts were annealed for 40 seconds at 290 °C under an N_2 rich environment. Both n- and p-contacts demonstrated ohmic behavior with low contact resistances, confirmed by transmission line measurement patterns. These contacts showed perfect durability after high temperature testing at temperatures above 300 °C. However, the long-term reliability of the metal contacts should be determined in future works. It is worth mentioning that the GaSb cap layer was not etched due to the strong oxidation and roughening of the $AlAs_{0.08}Sb_{0.92}$ etch-stop window layer during the wet-etch process [105].

The HFS600E-PB4 heating stage, made by Linkam Scientific Instrument, was used to measure the temperature-dependent performance of the $Al_xGa_{1-x}Sb$ PV cells. This stage is capable of reaching 600 °C. The temperature of the stage was monitored using a thermistor (TR). All the measurements were performed in an uncontrolled air environment. We observed a slight discrepancy between the TR temperature and the actual temperature of

the cell. However, this difference was found to be negligible (<3 °C). Thus, all the temperatures presented in this report correspond to the TR temperatures. Temperature-dependent behavior of some other III–V solar cells have already been demonstrated using this hot stage [125]–[127]. The temperature-dependent external quantum efficiency (EQE) was collected using a PV Measurements QEX10 equipped with a dual grating monochromator and monochromatic probe light with long wavelength detection capability up to 1750 nm. The temperature-dependent one-sun light J–V characteristics of the devices were performed by an Oriel class A solar simulator equipped with a Xenon ARC lamp. The J-V curves were acquired using a Keithley model 2400 source-meter. The AM1.5G spectrum with an irradiation intensity of 1 $kW.m^{-2}$, was considered in this work, as the reference spectrum. The J_{SC}, V_{OC}, FF, and efficiency (η) were extracted directly from the light J-V data. The intensity of the Xenon lamp was adjusted to match one-sun intensity using a Si reference cell. Although the integrated spectral irradiance of the solar simulator used in this work is similar to the AM1.5G irradiation intensity, their spectral irradiance distributions and, thus, the extracted dJ_{SC}/dT values are slightly different. The temperature was increased from 25 (room temperature) to 250 °C with intervals of 25 °C and a ramp rate of 20 °C/min. The measurements were performed ~5 minutes after the temperature stabilization at each step. Extra care was given to perform the temperature-dependent electrical measurements on the same best-performing cell of each device.

3.3. Results and Discussion

3.3.1. Solar Cell Parameters

Unlike some solar cells, such as perovskite [128], generally, bandgaps of solar cells decrease with temperature, including Sb-based solar cells. The temperature-dependent

bandgap in semiconductors can be described using a semi-empirical model provided by Varshni [14]:

$$E_g(T) = E_g(0) - \frac{\alpha T^2}{(\beta - T)} \tag{3.1}$$

where $E_g(0)$ is a bandgap value at T = 0 K. The α and β are constant values, which are unique for each material. The temperature-dependence of the bandgap is attributed to the electron-phonon interaction and, to a lesser degree, the thermal expansion of the lattice with temperature [129]. Varshni's values for GaSb reported by Vurgaftman *et al.* are $\alpha = 0.417$ meV/K, $\beta = 140$ K, and $E_g(0) = 0.812$ eV [130]. The $E_g(0)$ was determined by Wu *et al.* from extrapolating the temperature-dependent photoluminescence data of high-quality GaSb samples [131].

Dark current density, J_0, is an important parameter in understanding the minority carrier recombination mechanisms in the cell. Typically, J_0 increases exponentially with temperature and, thus, negatively impacts the device performance, particularly the V_{OC}. Based on the analytical drift-diffusion model, the total dark current density in the device can be summarized into two components: (1) dark current density in bulk and at the surface of the quasi-natural regions (J_{01}) and (2) dark current density in the depletion region (J_{02}). J_{01} can be represented as follows [132], [133]:

$$J_{01} = \frac{qD_e {n_i}^2}{L_e N_A} \times \frac{S_e \cosh\left(\frac{W_p}{L_e}\right) + \frac{D_e}{L_e}\sinh\left(\frac{W_p}{L_e}\right)}{\frac{D_e}{L_e}\cosh\left(\frac{W_p}{L_e}\right) + S_e \sinh\left(\frac{W_p}{L_e}\right)} + q\frac{D_h {n_i}^2}{L_h N_D} \times \frac{S_h \cosh\left(\frac{W_n}{L_h}\right) + \frac{D_h}{L_h}\sinh\left(\frac{W_n}{L_h}\right)}{\frac{D_h}{L_h}\cosh\left(\frac{W_n}{L_h}\right) + S_h \sinh\left(\frac{W_n}{L_h}\right)}. \tag{3.2}$$

The first term corresponds to the J_0 in the p-type emitter and the second term corresponds to the J_0 in the n-type base region. The q is the electron charge. $D_{e,h}$, $L_{e,h}$, and $N_{A,D}$ are the diffusion coefficients, minority carrier diffusion lengths, and acceptor/donor

concentrations in p- and n-type regions, respectively. $S_{e,h}$ is the surface recombination velocities at emitter-window and base-BSF interfaces, respectively. $W_{p,n}$ is the thickness of p- and n-type quasi-neutral regions, respectively.

The dark current density in the junction can be represented (based on the Sah-Noyce-Shockley theory) by a simplified form as [45]

$$J_{02} = \frac{qn_i WD}{2L^2}, \tag{3.3}$$

where W is the depletion width, L is the effective minority carrier diffusion length, and D is the diffusion coefficient. As shown, J_{01} and J_{02} values are strongly affected by $n_i(T)$. The relative importance of the J_{01} and J_{02} depends mostly on the device structure and the bandgap of the active layer. By considering the fact that the n_i term is proportional to the effective density of states in the conduction and valance bands and exponentially to the bandgap, the J_{01} and J_{02} terms can be rewritten as a function of temperature and the bandgap by

$$J_{01}(T) = CT^3 \exp\left(\frac{-E_g(T)}{kT}\right) \tag{3.4}$$

$$J_{02}(T) = C'T^{\frac{3}{2}} \exp\left(\frac{-E_g(T)}{2kT}\right). \tag{3.5}$$

These expressions show that by increasing temperature and, consequently, reducing the bandgap of the cell, both J_0 values increase at different rates, leading to the reduction of V_{OC} and η. Different constant values of C and C' have been reported in the literature. Green proposed an empirical CT^3 value of ~1.5×10^5 A.cm^{-2}, derived from Shockley's expression [133]. Fan reported a C value of 5.0×10^{-2} A.cm^{-2}.K^{-3}, based on empirical values [134]. Loferski proposed a model in which the CT^3 value is dependent on the diffusion length of

the material [135]. Particularly, Fraas *et al.* have determined a C value of ~1.84×10^{-3} $A.cm^{-2}.K^{-3}$ for GaSb [136]. In this work, we extend the Fraas study to the $Al_xGa_{1-x}Sb$ ternary system and show that C and C' values have a dependency on the saturation current density.

Another useful parameter presented in this work, which compares the performance of solar cells with different bandgaps, is the bandgap-voltage offset (W_{OC}). This value is related to J_0, J_{SC}, and E_g parameters. When W_{OC} becomes zero, V_{OC} approaches its theoretical value [80]. It is worth mentioning that the commonly accepted W_{OC} value for III-V solar cells is ~0.4 V. Finally, the experimental FF values were calculated from the ratio of maximum output power densities to the product of V_{OC} and J_{SC} values.

3.3.2. Temperature-dependence of GaSb Cell

I. Experimental Results

Figure 15 shows the light J-V characteristics of the GaSb cell from 25 to 175 °C, including the measurement taken after the high temperature cycling (post 25 °C). The V_{OC} reduces with temperature at a rate of ~1.6 mV/°C. As mentioned before, most solar cells exhibit a decrease in bandgap with temperature leading to an increase in J_{SC}. However, J_{SC} with temperature in the GaSb cell shows an opposite trend (a non-linear decline with temperature). There are two convuloted reasons for the descending pattern of the J_{SC} with temperature. On the one hand, carrier collection is reduced by (1) parasitic absorption due to bandgap redshift of the GaSb cap layer and, with a lesser degree, the $AlAs_{0.08}Sb_{0.92}$ window layer and (2) temperature-dependent free carrier absorption of the Sb-based layers, which increases with temperature [137], [138]. On the other hand, photon absorption should increase due to the reduction of the active layer bandgap as the absorbable photon density increases. However, the presence of atmospheric bands in the solar spectrum at

long wavelengths may be limiting this common trend. Atmospheric bands are mainly originated from the absorption of CO_2 and H_2O molecules and from Rayleigh scattering in the atmosphere [139]. Figure 16 shows the photon flux density of the AM1.5G solar spectrum, maximum achievable J_{SC} (with 100% collection efficiency), and the temperature-dependent bandgaps of the $Al_xGa_{1-x}Sb$ cells (x = 0, 0.15, and 0.50). As shown, the GaSb bandgap falls near one of the atmospheric bands. In particular, from E_g(25 °C) ~0.72 eV to E_g(175 °C) ~0.67 eV, the photon flux density reduces from ~1.7×10^{18} photons.m^{-2}.eV^{-1} to a negligible amount. Therefore, the maximum attainable J_{SC} remains unchanged in this spectral region. This effect, combined with the previously mentioned loss mechanisms, is responsible for the reduction of the J_{SC} with temperature. As a result, the efficiency of the GaSb cell decreases continuously up to 175 °C and above 200 °C, the cell shows no photovoltaic response, which indicates that the upper temperature limit for this cell is ~200 °C. Fortunately, the temperature limit can be further increased by using higher irradiation intensities, where J_{SC} and V_{OC} values can be increased. For example, at 100-sun concentration, the upper temperature limit of the GaSb cell (assuming the ideality factor (n) of 1) can be increased to ~360 °C. This temperature regime makes GaSb-based cells attractive for the space applications, as suggested by Teofilo *et al*. and for some PV-T systems [115]. Moreover, the cell shows good durability as the post 25 °C curve overlaps the 25 °C J-V curve. The extracted cell parameters (V_{OC}, J_{SC}, W_{OC}, and FF) are presented in Fig. 17 and summarized in Table 8.

TABLE 8. LIGHT J-V VALUES AND SINGLE-DIODE PARAMETERS OF THE GASB CELL EXTRACTED FROM THE DARK J-V CURVES.

Temp (°C)	V_{OC} (V)	J_{SC} (mA/cm^2)	FF (%)	η (%)	J_0 (mA/cm^2)	n	R_{SH} (Ω.cm^2)	R_S (Ω.cm^2)
25	0.275	22	51	3.1	4.50×10^{-5}	1.6	199	3.8
75	0.195	21.8	42	1.8	5.22×10^{-4}	1.6	86	4.0
125	0.105	18.9	31	0.6	2.66×10^{-3}	1.5	25	4.3
175	0.035	11	25	0.1	1.66×10^{-2}	1.6	10	3.7
Post 25	0.275	21.6	52	3.1	4.6×10^{-6}	1.6	210	3.5

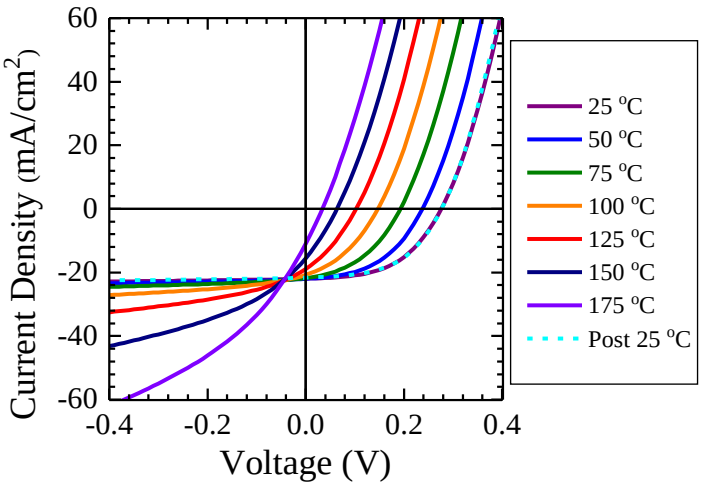

Figure 15. Light J-V characteristics of the GaSb cell as a function of temperature.

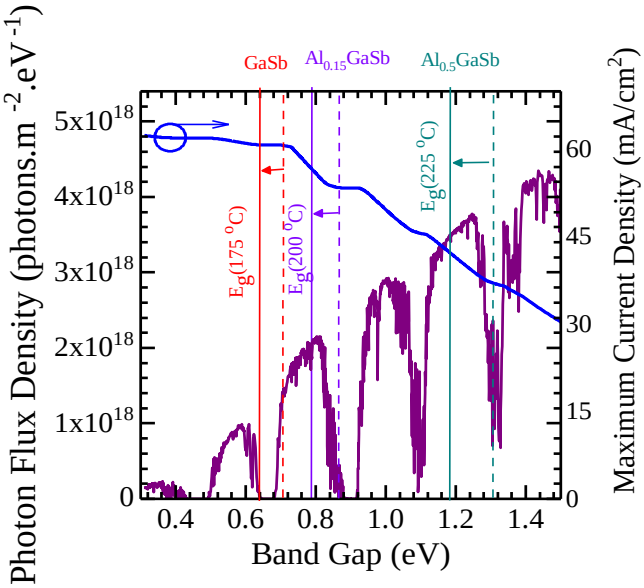

Figure 16. The photon flux density of AM1.5G solar spectrum and maximum achievable J_{SC} with a collection efficiency of one vs. bandgap. The dashed lines show the bandgap values at 25 °C and the solid lines represent the bandgap values at elevated temperatures.

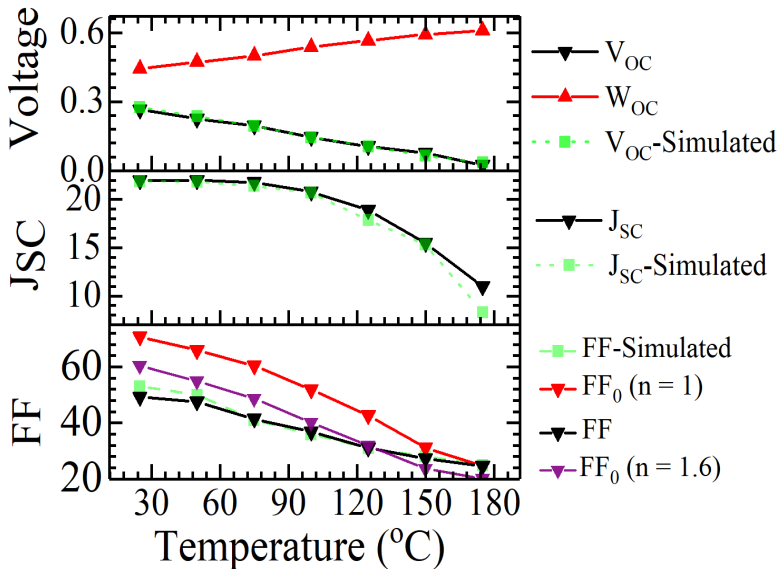

Figure 17. Numerical and experimental temperature-dependent characteristics of the GaSb cell (W_{OC}, V_{OC} (V), J_{SC} (mA/cm^2), and FF (%)). The ideal fill factor (FF_0) with different ideality factors are presented for the comparison.

Table 9 lists the temperature sensitivities of these parameters (dV_{OC}/dT, dJ_{SC}/dT, dJ^2_{SC}/dT^2, dW_{OC}/dT, and dFF/dT). All the temperature sensitivities are calculated by a linear fitting except for the $J_{SC}(T)$ temperature sensitivity, which is extracted by using a second-degree polynomial. Nevertheless, this non-linearity has a negligible effect on the V_{OC} linear trend. It is worth mentioning that these rates are underestimations of an ideal GaSb cell since other parameters such as resistances and crystal quality affect the overall cell performance [14]. For example, the ideal fill factor (FF_0) (assuming n = 1), which does not consider the resistive losses, shows a higher value than the device FF. The FF_0 can be represented as a function of normalized v_{oc} (qV_{OC}/kT) by

$$FF_0 = \frac{v_{oc} - \ln(v_{oc} + 0.72)}{v_{oc} + 1}. \quad (3.6)$$

This implies that series resistance (R_S) has an impact on the carrier collection efficiency at different temperatures.

TABLE 9. TEMPERATURE SENSITIVITIES OF THE $AL_XGA_{1-X}SB$ CELL PARAMETERS (X = 0, 0.15, AND 0.50) [130], [131] (THE BANDGAPS ARE EXTRACTED FROM THE EQE MEASUREMENTS).

Active region	dV_{OC}/dT (mV/ °C)	dJ^2_{SC}/dT^2 (mA.cm^{-2} .°C $^{-2}$)×10^{-3}	dJ_{SC}/dT (mA.cm^{-2} ·°C $^{-1}$)	dW_{OC}/dT (mV/ °C)	dFF/dT (%/°C)
GaSb	1.6	0.8	0.5	1.3	0.178
$Al_{0.15}Ga_{0.85}Sb$	1.9	0.7	0.1	1.5	0.175
$Al_{0.5}Ga_{0.5}Sb$	2.3	0.08	0.02	1.8	0.168

The temperature-dependent dark J-V characteristics of the GaSb cell, shown in Fig. 18 and Table 8, exhibit a single diode behavior at all temperatures. The cell shows n values of ~1.6 at all temperatures and the J_0 value exponentially increases with temperature from 25 to 175 °C. The low J_0 value of 4.5×10^{-5} mA/cm^2 at room temperature can be attributed to a low density of defects and the $AlAs_{0.08}Sb_{0.92}$ passivation layers that suppress the minority carrier diffusion to the GaSb surfaces.

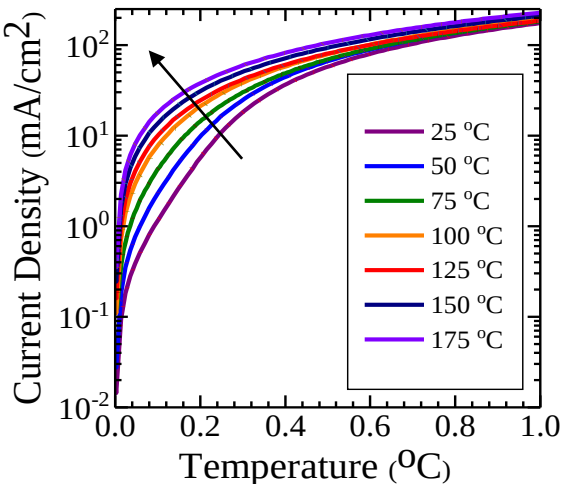

Figure 18. Dark J-V(T) characteristics of the GaSb cell fitted with a single-diode model.

The J_0 values were then compared to Eq. 3.4 and Eq. 3.5 in order to understand the dominant factor that results in an increase of J_0 with temperature. It was found that J_0 linearly depends on the $T^{3/2}\exp(-E_g(T)/2kT)$ term of Eq. 3.5 with a C′ value of ~1.1×10^{-2} mA.cm^{-2}.K$^{-3/2}$. The agreement between the temperature-dependent J_0 extracted from the

dark J-V curves, and the temperature-dependent J_0 calculated from Eq. 3.5, suggests a strong correlation between the J_0 and n_i, as demonstrated in Fig. 19(a). In other words, the dark current is primarily affected by the temperature-dependent intrinsic carrier concentration, $n_i(T)$, due to the reduction of the narrow GaSb bandgap. In addition, this agreement implies that the minority carrier recombination occurs mostly in the depletion region. To corroborate this, a set of temperature-dependent capacitance-voltage (C-V) measurements were performed (not shown here) to calculate the depletion widths of the GaSb cell. The measurements show that the GaSb cell remains fully depleted with increasing temperature, even though the depletion width reduces with temperature. It is worth mentioning that the small differences between the J_0 values in Fig. 19(a) can be ascribed to other temperature-dependent factors, mainly the diffusion minority carrier lifetimes (see Eq. 3.5).

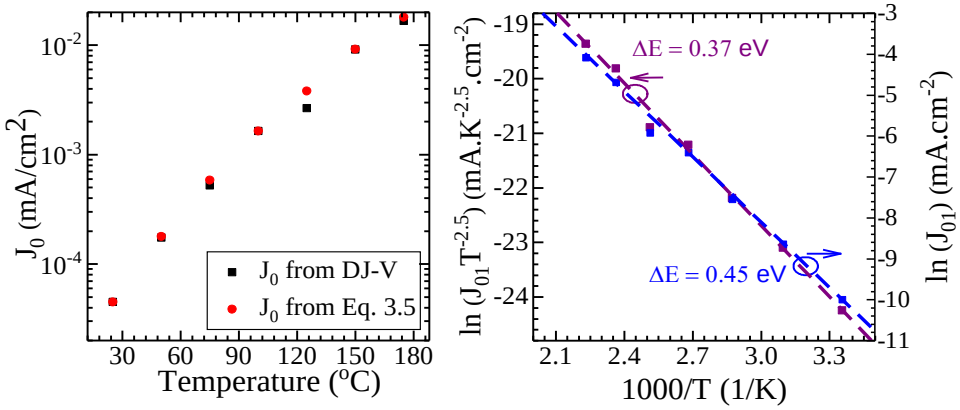

Figure 19. (a) Dark current density extracted from the temperature-dependent dark J-V curve compared to the dark current density derived from Eq. 3.5 for the GaSb cell. (b) $\ln(J_{01})$ and $\ln(J_{01}T^{-2.5})$ vs. 1000/T of the GaSb cell.

The J-V characteristics of the GaSb cell can be modeled by the well-known single-diode equation:

$$J = J_{01}[\exp\left(\frac{q(V - JR_S)}{n_1 kT}\right) - 1] + \frac{V - JR_s}{R_{SH}},$$
$$J_{01} = J_{001}\exp\left(\frac{-\Delta E}{kT}\right) \quad (3.7)$$

where ΔE and J_{001} are activation energy and exponential prefactor, respectively [140]. To further confirm the suggested transport mechanism, where the recombination mostly happens in the depletion region, plots of $\ln(J_{01}T^{-2.5})$ and $\ln(J_{01})$ vs. 1000/T were made in the temperature range of 25 to 175 °C, as shown in Fig. 19(b). If the current is controlled by the recombination in the depletion region through localized states, the ΔE extracted from Fig. 19(b) should be approximately equal to half of the GaSb bandgap [140], [141]. If the ΔE value is close to the bandgap, then the transport mechanism is controlled by diffusion [142]. The extracted ΔE value of 0.37 eV, which is close to half of GaSb bandgap, confirms that the generation-recombination in the depletion region dominates the carrier transport in the GaSb cell. It is worth mentioning that if the interface recombination is a dominant factor in carrier transport, then Fig. 19(b) should yield a ΔE value of close to the built-in potential, which is not the case.

The R_{SH}, which is caused by the leakage across the pn junction, slightly changes with temperature. This indicates that the R_{SH} does not play an important role in the V_{OC} reduction. The dependence of the J_0 on the $n_i(T)$ and the slight change of the R_{SH} with temperature confirm that the device performance is impacted mainly by carrier transport issues across the junction rather than shunting issues.

Figure 20 shows the temperature-dependent EQE with three notable trends. First, the long cutoff wavelength increases towards longer wavelengths by temperature. This transition is directly related to the redshift in the absorption band edge, caused by the

shrinkage of the bandgap. Second, the J_{SC} extracted from the EQE(T) reduces with a non-linear trend, similar to the J_{SC} from the light J-V curves. The peak EQE of ~42% at room temperature, with corresponding internal quantum efficiency (IQE) of ~70%, reduces to ~11% at 175 °C. The room temperature EQE has almost the same profile after the high temperature cycling, which again, shows the thermal robustness of the cell. Third, the blue wavelength response drops with temperature, which can be ascribed to the absorption in the 20-nm-thick p-GaSb contact layer. The severe EQE degradation in the short wavelength regimes can be due to the thick GaSb contact layer and the high bandgap of $AlAs_{0.08}Sb_{0.92}$ compared to the GaSb contact layer and GaSb active layer making the window layer to act as a diffusion barrier to minority carriers.

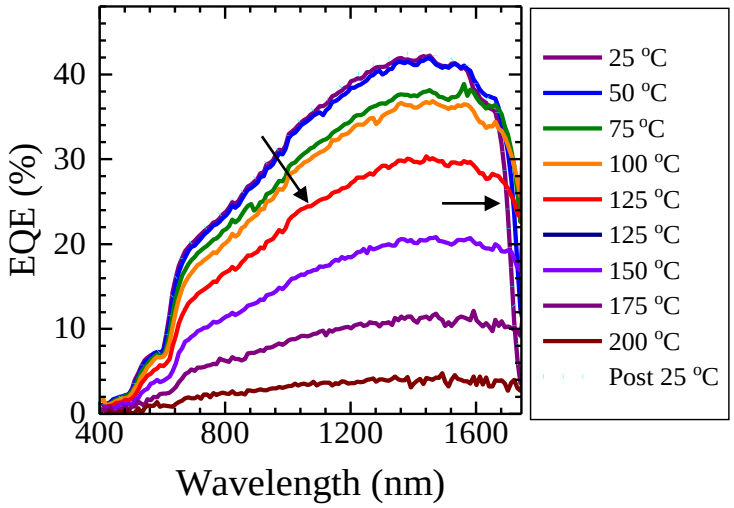

Figure 20. Temperature-dependent EQE of the GaSb cell. (Note: the data above 1750 nm is not available due to limitations of the EQE tool.)

The temperature-dependent bandgaps of the GaSb active layer were extracted from the inflection point of the EQE(T) plots (at the long wavelength regime). At room temperature, the bandgap value corresponds to ~0.717 eV which redshifts to ~0.645 eV at 175 °C. As shown in Fig. 21, the experimental temperature-dependent bandgaps were compared to the earlier determinations given by Bellani *et al.* (T<25 °C), Ghezzi *et al.* (T<25 °C),

Vurgaftman *et al.*, and Faars *et al.* [130], [136], [143], [144]. These results are in agreement with the values reported by Fraas *et al.*, with a maximum deviation of ~9 meV. A least-square fit of the data points (25 °C<T<100 °C) gives dE_g/dT of ~0.5 meV/°C and Varshni parameters of α ~0.67 meV/K and β ~344 K.

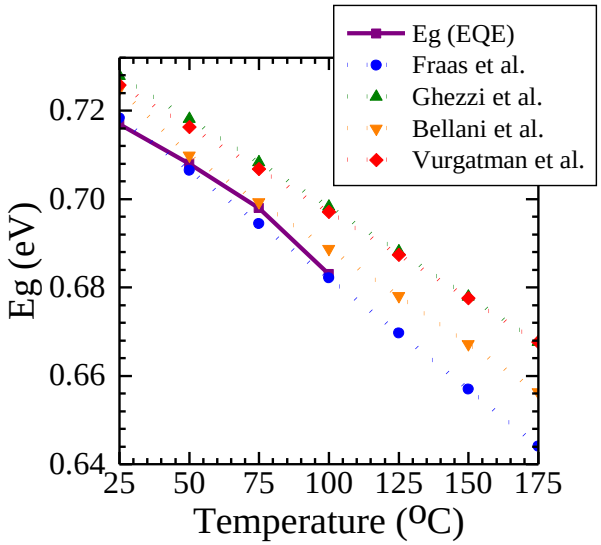

Figure 21. Temperature-dependence of the GaSb bandgap. The bandgap values are derived from the EQE measurements and compared to the models proposed by Bellani *et al.*, [145], Ghezzi *et al.* [146], Vurgaftman *et al.*, [130], and Faars *et al.* [136] (all based on Varshni's semi-empirical model). The bandgap values found in this work are not presented for T > 100 °C, due to limitations of the EQE tool.

II. Modeling and Material Parameters

The temperature-dependent device performance of the GaSb cell was modeled using Silvaco Atlas TCAD software [147]. The electron and hole mobilities (μ_e and μ_h, respectively) were calculated as a function of composition- and temperature-dependent coefficients using Caughey–Thomas empirical model [148]. All the reliable mobility models in the literature are fit to empirical Hall data [148]–[150]. However, for photovoltaic devices, drift mobility is a parameter that should be considered instead of the Hall mobility, given the drift-diffusion nature of solar cells. The difference between drift and Hall mobilities is found to be small for n-GaSb, [151], [152], and negligible for

heavily-doped p-GaSb [153]. Thus, in this work, the Hall mobility was used to model the temperature-dependent performance of the GaSb cell, even though this may cause some differences between the theoretical and experimental results. As mentioned, among all the available models for III-V alloys, Caughey–Thomas model fits well with the experimental data [154], and it is expressed as

$$\mu_i(N,T) = \mu_{min,i} + \frac{\mu_{max,i}(300K)\left(\frac{300K}{T}\right)^{\theta_{1,i}} - \mu_{min,i}}{1+\left(\frac{N}{N_{R,i}(300K)\left(\frac{T}{300K}\right)^{\theta_{2,i}}}\right)^{\gamma_i}}, \tag{3.8}$$

where i represents either electrons or holes and N is doping concentration. The $N_{R,i}$ is a doping concentration where the mobility reduces to half of the mobility at a low doping level and γ_i is a temperature independent fitting parameter. The values used in this study were taken from Martin *et al.*, [155], and are summarized in Table 10.

TABLE 10. VALUES USED FOR THE ELECTRON AND HOLE MOBILITIES [155].

Carrier type	$\mu_{max,i}$ ($cm^2.V^{-1}.s^{-1}$)	$\mu_{min,i}$ ($cm^2.V^{-1}.s^{-1}$)	$\theta_{1,i}$	$\theta_{2,i}$	γ_i
Electron	5650	1050	2.0	2.8	1.05
Hole	875	190	1.7	2.7	0.65

Accurate determination of n_i is important for modeling the temperature-dependent performance of narrow bandgap devices, due to the significant impact of n_i on V_{OC}. The n_i can be calculated by the following expression [156]

$$n_i = 2\left(\frac{2\pi m_0 kT}{h^2}\right)^{\frac{3}{2}} \cdot \left(m_{e,L}^{*\frac{3}{2}} \exp\left(\frac{-\Delta E_{\Gamma,L}}{kT}\right) + m_{e,\Gamma}^{*\frac{3}{2}}\right)^{\frac{1}{2}} \cdot \left(m_{h,l}^{*\frac{3}{2}} + m_{h,h}^{*\frac{3}{2}}\right)^{\frac{1}{2}} \cdot \exp\left(\frac{-E_g}{2kT}\right), \tag{3.9}$$

where $\Delta E_{\Gamma,L}$ is the energy difference between the minima of Γ and L bands with a value of ~0.08 eV [157]. The m_L^* and m_Γ^* are room temperature electron and hole density of states

effective masses at L and Γ bands, respectively, presented by Stollwerck *et al.* [156]. The n_i increases approximately from 1.4×10^{12} cm^{-3} at 25 °C to 5.3×10^{14} cm^{-3} at 175 °C, respectively. The values used in this work are slightly different from the values reported by Dutta *et al.* [158]. We speculate that this difference is related to the values of $\Delta E_{\Gamma,L}$, m_L^*, and m_Γ^*, which change with temperature.

Temperature-dependent recombination mechanisms such as radiative, Auger, and Shockley-Read-Hall (SRH) are also included in the numerical analysis. The radiative recombination is a band-to-band emission process, and its coefficient (B) can be extracted by [156], [159]

$$B = 5.8\times10^{-13}\sqrt{\varepsilon}\left(\frac{1}{m_h^*+m_e^*}\right)^3.\left(1+\frac{1}{m_h^*}+\frac{1}{m_e^*}\right).\left(\frac{300}{T}\right)^{\frac{3}{2}}E_g^2, \qquad (3.10)$$

where ε is the GaSb dielectric constant. The B values for GaSb are approximately 8.7×10^{-11}, 6.6×10^{-11}, 5.1×10^{-11}, and 4.0×10^{-11} cm^3/s at 25, 75, 125, and 175 °C, respectively. On the other hand, the Auger recombination is a fundamental non-radiative mechanism, unlike SRH and surface/interface recombinations, and directly relates to n_i and active area thickness, which increases with temperature. Under high bulk SRH lifetime and low surface recombination velocities, Auger recombination determines the effective lifetime and intrinsic limit to the cell performance [160]. Based on our simulations, the cell characteristics are well below their intrinsic limits, meaning the bulk and interface quality should be further improved in order for the cell to approach its intrinsic Auger-limited efficiency. The temperature-dependent Auger recombination model was adopted from Tian *et al.*, [161], with C_p values of 3.05×10^{-28}, 5.22×10^{-28}, 9.57×10^{-28}, and 1.1×10^{-27} cm^6/s and C_n values of 8.8×10^{-28}, 1.58×10^{-27}, 2.98×10^{-27}, and 3.45×10^{-27} cm^6/s at 25 , 75, 125, and

175 °C, respectively. The SRH trap-assisted lifetime, caused by defect states within the semiconductor can be expressed by [162]

$$\tau_{SRH<n,p>} = \frac{1}{\sigma N_t}\sqrt{\frac{m_{<n,p>}}{3k_B T}}, \tag{3.11}$$

where σ is the capture cross-section of the minority carriers and N_t is the density of traps, with values of 1.5×10^{-15} cm^2 and 1.17×10^{15} cm^{-3}, respectively. The k_B is the Boltzmann constant. The calculated temperature-dependent SRH lifetime values are 9.8, 9.1, 8.2, and 7.9 ns for $\tau_{SRH<n>}$ and 30.9, 28.6, 26.0, and 25.2 ns for $\tau_{SRH<p>}$ at 25, 75, 125, and 175 °C, respectively. The reduction of the SRH and Auger lifetime (increasing the Auger coefficients) values, in conjunction with the minority carrier mobilities at high temperatures, lead to the degradation of the minority carrier diffusion length, and eventually, the cell performance.

The absorption coefficient of GaSb at room temperature (25 °C) was taken from the dielectric model proposed by Adachi *et al.* [121], [163]. In order to incorporate temperature, a temperature-dependent absorption shifted model was adopted from Martin *et al.*, $\alpha(T) = \alpha(300\ K) + \Delta\alpha(T)$, [164]. The absorption edge displacement, $\Delta\alpha(T)$, can be expressed as

$$\Delta\alpha(T) = hc\frac{E_{g,300K} - E_g(T)}{E_{g,300K}E_g(T)}. \tag{3.12}$$

The *h* is the plank constant. This model indicates that as temperature increases the absorption band edge increases towards longer wavelengths. The temperature-dependent J-V curves of the GaSb cell were then modeled by considering the aforementioned parameters. The simulated results are in a good agreement with the experimental results,

as shown in Fig. 17 and Fig. 22. The simulation results show that even though the absorption band edge increases with temperature, the photocurrent decreases with a non-linear trend, similar to the experimental data. On the other hand, the absolute V_{OC} and FF temperature coefficients (dV_{OC}/dT and dFF/dT) change linearly with values of 1.6 mV/°C and 0.18 %/°C, respectively. The V_{OC} values are underestimated in the range of 25 to 100 °C and overestimated at 150 and 175 °C, as shown in Fig. 17. Similar inaccuracy was observed in the $J_{SC}(T)$ and FF. These discrepancies between the experimental and analytical results can be attributed to the inaccuracy of $n_i(T)$, $\alpha(T)$, and $\mu_i(T)$ models, which could be resolved by proposing more complex models. In general, the temperature-dependent results are well reproduced by the simulation, validating the used GaSb material parameters.

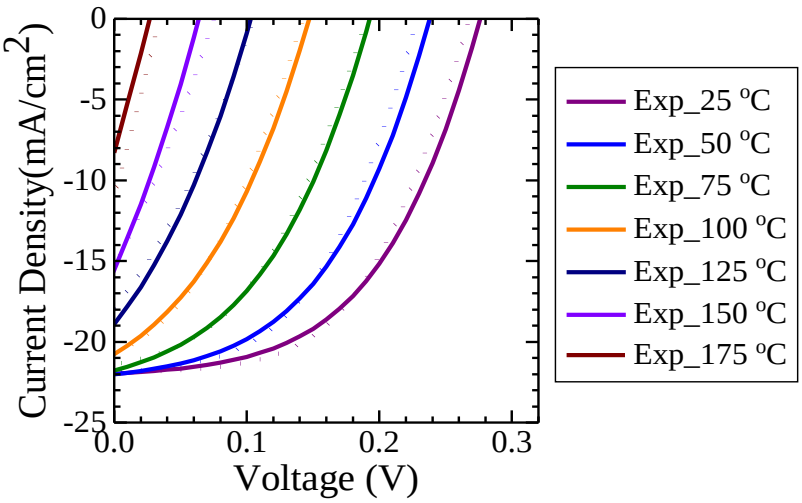

Figure 22. Simulated and experimental light J-V characteristics of the GaSb cell as a function of temperature under AM1.5G illumination with an irradiation intensity of 1 KW.m^{-2}. The dotted curves represent the simulation results."Exp" term stands for "experimental".

3.4. Temperature-dependence of $Al_xGa_{1-x}Sb$ Cell

Figure 23, Table 11, and Table 12 show the temperature-dependent light J-V characteristics of $Al_xGa_{1-x}Sb$ cells with the best total-area efficiencies. The $Al_{0.15}Ga_{0.85}Sb$

and $Al_{0.5}Ga_{0.5}Sb$ cells show V_{OC} values of 0.34 and 0.54 V, respectively, at room temperature, which decrease with the temperature at rates of 1.9 and 2.3 mV/°C, respectively.

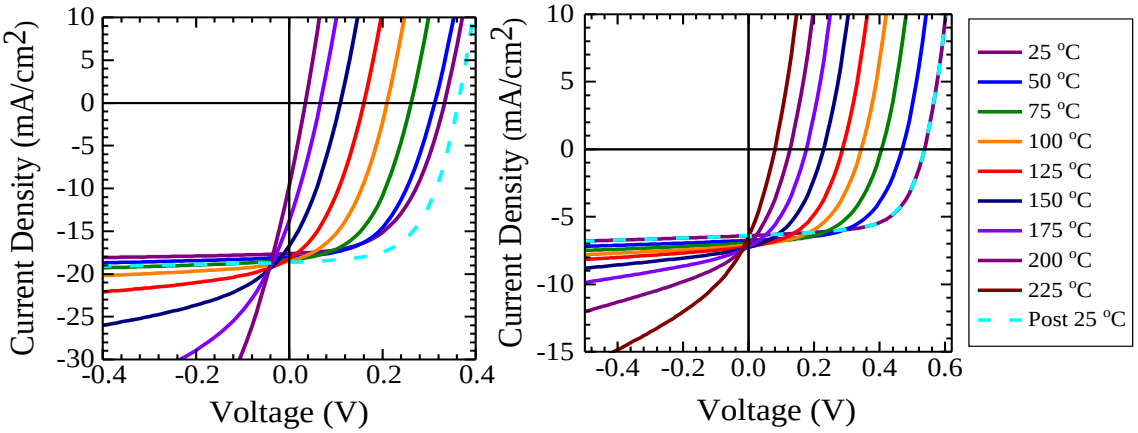

Figure 23. (a) Light J-V characteristics of the $Al_{0.15}Ga_{0.85}Sb$ and (b) $Al_{0.5}Ga_{0.5}Sb$ solar cells as a function of temperature under AM1.5G illumination with an irradiation intensity of 1 $kW.m^{-2}$.

TABLE 11. LIGHT J-V CHARACTERISTICS AND DIODE FITTING PARAMETERS EXTRACTED FROM DARK J-V CURVES OF THE $AL_{0.15}GA_{0.85}SB$ SOLAR CELL.

$Al_{0.15}Ga_{0.85}Sb$ Solar Cell

Temp (°C)	V_{OC} (V)	J_{SC} (mA/cm^2)	FF (%)	J_0 (mA/cm^2)	n	R_{SH} ($K\Omega.cm^2$)	R_S ($\Omega.cm^2$)
25	0.34	17.6	53	5.8×10^{-6}	1.6	3.50	6.7
75	0.27	18.5	48	4.5×10^{-5}	1.5	1.34	7.3
125	0.17	18.7	35	3.2×10^{-4}	1.4	0.20	6
175	0.11	13.8	28	1.8×10^{-3}	1.3	0.05	4.4
225	-	-	-	-	-	-	-
Post 25	0.35	18.6	59	1.4×10^{-6}	1.7	9.8	0.9

TABLE 12. LIGHT J-V CHARACTERISTICS AND DIODE FITTING PARAMETERS EXTRACTED FROM DARK J-V CURVES OF THE $AL_{0.5}GA_{0.5}SB$ SOLAR CELL.

$Al_{0.5}Ga_{0.5}Sb$ Solar Cell

Temp (°C)	V_{OC} (V)	J_{SC} (mA/cm^2)	FF (%)	J_{01} (mA/cm^2)	J_{02} (mA/cm^2)	n	R_{SH} ($K\Omega.cm^2$)	R_S ($\Omega.cm^2$)
25	0.54	6.4	63	1.2×10^{-8}	6.1×10^{-7}	1.6	2.9	45.50
75	0.41	6.9	54	4.7×10^{-7}	1.0×10^{-7}	1.6	3.9	30.10
125	0.29	7.2	47	1.3×10^{-5}	1.5×10^{-4}	1.6	8.9	3.50
175	0.18	7.2	38	1.1×10^{-4}	-	1.5	-	0.43
225	0.08	6.5	30	1.6×10^{-3}	-	1.7	-	0.15
Post 25	0.54	6.4	63	1.0×10^{-9}	6.2×10^{-7}	1.7	2.2	13

$J_{SC}(T)$ of both cells exhibits a non-linear trend, similar to the GaSb cell. However, unlike the GaSb cell, the J_{SC} value increases initially at low-temperatures as photon absorption increases and then reduces at elevated temperatures, where parasitic losses become more dominant, see Fig. 24. We notice that as Al content increases from 0.15 to 0.50, J_{SC} reduces dramatically, most likely because of the bandgap changing from direct to indirect at Al content of approximately 47% [130]. In general, the diffusion length is more prominent in indirect bandgap cells (such as $Al_{0.5}Ga_{0.5}Sb$) with an overall lower absorption coefficient compared to direct bandgap cells (such as $Al_{0.15}Ga_{0.85}Sb$). This means that in order to improve the J_{SC}, the absorber thickness of $Al_{0.5}Ga_{0.5}Sb$ should be further increased. It is noteworthy that as the Al mole fraction increases, the local maximum of $J_{SC}(T)$ moves towards higher temperature, and the absolute J_{SC} temperature coefficient reduces, as shown in Fig. 24.

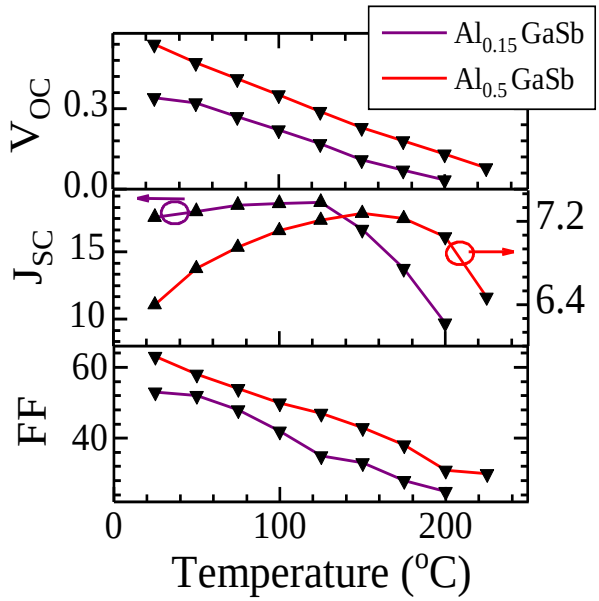

Figure 24. Temperature-dependent characteristics of the $Al_xGa_{1-x}Sb$ solar cells (x = 0.15 and 0.5).

The temperature-dependent dark J-V curves of the cells were fit with single- and double-diode models, as shown Fig. 25, Table 11, and Table 12. The $Al_{0.15}Ga_{0.85}Sb$ cell exhibits a single-diode behavior whereas the $Al_{0.5}Ga_{0.5}Sb$ cell shows a double-diode behavior at low-temperatures, which collapses to a single-diode mode at elevated temperatures due to the dominance of J_{01}.

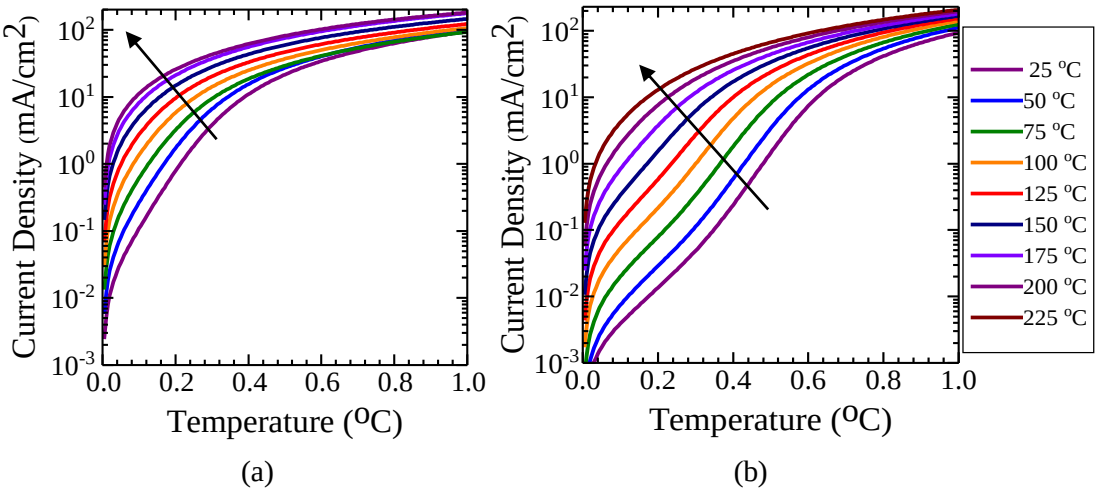

Figure 25. (a) Temperature-dependent dark J-V characteristics of the $Al_{0.15}Ga_{0.85}Sb$ and (b) $Al_{0.5}Ga_{0.5}Sb$ solar cells at different temperatures. (Note: the fitted curves are not shown here.)

In the $Al_{0.15}Ga_{0.85}Sb$ cell, the J_0 increases almost three orders of magnitude from 25 to 200 °C. The J_0 is coincident with Eq. 3.5, with an extracted C' value of ~1.1×10^{-2} $mA.cm^{-2}.K^{-1.5}$, which indicates that the thermally excited intrinsic carriers have the main impact on the J_0, similar to our finding for the GaSb cell. The slope around the short circuit was fit well with R_{SH} values of ~3.5 $K\Omega\cdot cm^2$ at 25 °C and ~50.0 $\Omega\cdot cm^2$ at 200 °C. However, the slope at the open circuit shows insensitivity of the R_S to temperature. Therefore, as temperature increases, (ohmic or non-ohmic) shunting issues and not carrier transport issues become the main limiting factors. In addition, the ideality factor slightly reduces from 1.6 to 1.3 by increasing temperature from 25 to 175 °C.

After the high temperature cycling (post 25 °C), V_{OC} and FF show 10 mV and 6 % increase, respectively, see Fig. 24. In addition, the R_{SH} increases to ~9.8 $K\Omega.cm^2$, and the R_S reduces to 0.9 $\Omega.cm^2$. The convex shape of the light J–V curve between –0.5 V and the maximum power point (MPP) at post 25 °C is a characteristic of improvement in the shunting issue, indicating a small deviation from complete repeatability of the cell. This performance improvement can be ascribed to the change in crystal quality. This change might be related to the reduction of point defects in the bulk and improvement of the interface passivation. Interestingly, after the temperature cycling, no dislocation annihilation was observed by transmission electron microscopy (not shown here). The cell was then exposed to additional high-temperature cycling, and neither performance improvement nor degradation was observed.

In $Al_{0.5}Ga_{0.5}Sb$ cell, J_{01} increases approximately five orders of magnitude from 25 to 225 °C. The first diode demonstrates an n_1 value of ~1.7 at all temperatures, which could indicate that the recombination mostly occurs in the bulk; however, n_2 dramatically

increases from 2.9 to 8.9, in the temperature range of 25 to 125 °C. The high n_2 value can be related to the tunneling through AlGaSb/AlAsSb interface states. It is also evident that by increasing the Al content, the J_0 reduces exponentially, leading to a linear increase of the V_{OC}. The V_{OC} and the upper limit of operating temperature can be further improved by eliminating the negative contributing factors to the J_0, mainly related to the material quality. Moreover, improving the J_{SC} can be achieved by different approaches, such as implementing photon recycling methods (*e.g.,* forming a reflector on the backside of the cell by Au/SiO_2 [165]), applying a temperature-resistant antireflection coating, removing the GaSb contact layer, and optimizing the effective thickness of the active layer.

As expected, the log cutoff wavelengths of the EQE curves of the $Al_{0.15}Ga_{0.85}Sb$ cell redshift with temperature, Fig. 26, (the $Al_{0.5}Ga_{0.5}Sb$ EQE results are not presented here as they have similar behaviors to their counterparts). The bandgap values of the $Al_{0.15}Ga_{0.85}Sb$ cell reduces linearly with temperature form ~0.87 eV at 25 ℃ to ~0.81 eV at 200 ℃, with a dE_g/dT of ~0.4 meV/℃. It is evident that between wavelengths of ~1100 to ~1450 nm the EQE first increases with temperature (until 125 ℃) as a result of carrier collection enhancement of the active layer, then, it reduces by increasing temperature, see Fig. 26. However, at wavelengths from ~600 to ~1000 nm, the EQE reduces with temperature. We speculate that this can be related to the thermal activation of the defect states and/or bandgap reduction of the upper epitaxial layers. The effects observed in the EQE curves are convoluted in the non-linear trend of the J_{SC} vs. temperature.

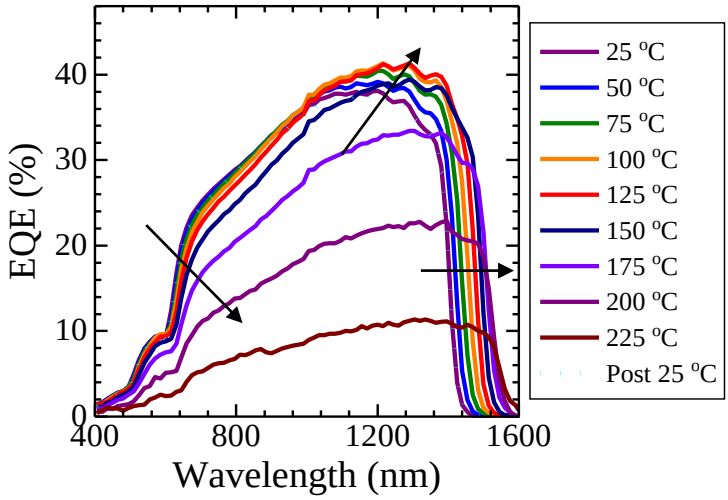

Figure 26. Temperature-dependent EQE characteristics of the $Al_{0.15}Ga_{0.85}Sb$ solar cell.

3.5. Conclusion

In this work, the high temperature characteristics of the single-junction $Al_xGa_{1-x}Sb$ cells with different Al contents (x = 0, 0.15, 0.50) over a temperature range of 25 to 250 °C have been presented. Temperature-dependent losses of the cells have been pointed out, and fundamental temperature coefficients have been calculated. Impacts of the absorption bands of the incident spectrum on the cell performance have also been highlighted. All the device characteristics showed degradation with temperature. It was shown that while the $Al_xGa_{1-x}Sb$ bandgap reduces with increasing temperature, the J_{SC} decreases with a non-linear trend. Also, based on the dark J-V analysis, it was found that the thermally excited intrinsic carriers dominate the performance degradation of the cells at different temperatures. The detrimental effect of J_0 on the cell performance is expected to be reduced by increasing the incoming light concentration as it increases the J_{SC}. In addition, multiple temperature cycles showed the long-term durability of the cells.

To perform a reliable numerical simulation of the GaSb cell performance at different operating temperatures, a set of temperature-dependent material parameters was proposed

in this study. The simulation results using the proposed parameters reproduced the findings from the light J-V(T) and EQE(T) measurements.

CHAPTER 4

DESIGN AND FABRICATION OF INGAN SOLAR CELLS FOR HIGH TEMPERATURE APPLICATIONS

4.1. Introduction

III-nitride-based compounds are widely used for optoelectronic applications. The indium gallium nitride (InGaN) alloy has emerged as a promising candidate for space and terrestrial photovoltaic (PV) applications due to its unique properties, such as a direct tunable bandgap covering the entire visible spectrum, high absorption coefficient, high carrier mobility, and high thermal and radiation resistance [3], [22], [166], [167].

III-nitride devices have shown operation up to 600 °C without any significant material or device degradation, in part due to their low intrinsic carrier concentration (n_i) and high bandgap [125], [168], [169]. In particular, InGaN can be used for concentrated solar power (CSP) and photovoltaic-thermal hybrid systems, which benefit from operation at elevated temperatures. However, InGaN solar cells suffer from numerous material issues such as lattice mismatch, polarization-induced electric fields, low p-type doping, and phase separation due to the immiscibility of GaN and InN [22]. In addition, the primary carrier extraction mechanism in a p-i-n InGaN solar cell is drift by means of the internal electric field, in part due to the short minority carrier diffusion length inherent in III-nitride compounds [47]–[49]. Thus, due to the mentioned constraints, InGaN MQW cells have demonstrated better performances [170] compared to the double hetero-junction and homo-junction devices [24]–[28], [30]. An MQW design allows a higher In incorporation than bulk, at the expense of lower carrier extraction. The carrier extraction, however, increases at high temperatures due to bandgap reduction and thermionic emission (TE).

The optimal MQW cell design must account for the tradeoff between photon absorption (*e.g.*, by increasing the number of QWs and In composition) and carrier extraction, which depends on the active region thickness, doping, and contact resistance. Specifically, the cell efficiency directly depends on the thicknesses of QBs and QWs as they change the effective bandgap and the cut-off wavelength. It is shown that by increasing the QW thickness (t_w), the absorption cut-off energy redshifts, which does not necessarily translate into an efficiency enhancement because of the reduction in electron-hole wavefunction overlap [171]. Further, thick QWs (higher than critical thickness) with high In composition lead to structural degradation due to strain relaxation and phase separation that can shunt the drift field. These combined effects make the InGaN solar cells with thick QWs have low efficiencies, regardless of operating temperature. In this study, the influence of QB thickness (t_b) and the number of QWs on the absorption, carrier collection, and AC and DC electrical characteristics at elevated temperatures are studied to draw a conclusion for optimum cell design.

4.2. Experimental Details

4.2.1. Device Fabrication Process of III-nitride Solar Cells

After the growth of the solar cell structures via MOCVD, they were processed into solar cells. Device fabrication was performed based on the standard nitride-based semiconductor processing techniques. There were three main steps for the realization and optimization of III-N solar cell fabrication: photolithography, metallization, and etching. Different mask sets were designed to optimize solar cell performance. Reliable ohmic contacts to n- and p-GaN with low resistivities at high temperatures (up to 500 ºC) were realized using CTLM patterns. This section details the fabrication process sequence of the InGaN solar cells designed for high temperature applications.

The fabrication process sequence is shown in Fig. 27. A standard surface cleaning was performed using Acetone followed by methanol and rinsed immediately via deionized water (DI) water. This process can remove contaminants and organic materials. Solar cell samples were then annealed for 5 minutes to remove moisture. After surface cleaning, photolithography technique was used to form mesa formation on the multi-quantum well solar cells. The photoresist (AZ4330) was then hard baked at 120 ºC for one minute. Mesa etch was then performed via an inductively coupled plasma (ICP) etch tool using BCl_3 (8 sccm)/Cl_2 (30 sccm)/Ar (5 sccm) chemistry for electrical isolation of the solar cells. The ICP technique provides the smooth sidewalls (verified via SEM) necessary to reduce surface recombination. The mesa dimension used in this study is 2.2×2.8 mm^2. The platen and coil powers used in this work were high (70 and 400 W, respectively) due to the strong bond strength of III-N materials. Next, the n-GaN contact layer (Ti/Al/Ni/Au with thicknesses of 150/2200/400/2000 Å) was deposited using the electron beam evaporation technique. The Ti and Al were chosen because of their low work function of ~4.33 and ~4.24 eV, respectively. Contacts were then annealed at 740 ºC for 2 minutes under an N_2 atmosphere via the rapid thermal pulse (RTP) tool to improve the ohmic conductivity. It is shown in this study that the Ti on top of the n-GaN forms a TiN layer leads to the formation of nitrogen vacancies which in turn act as donors at the semiconductor/metal interface. The heavily doped interface provides a thin depletion region leading to the reduction of the Schottky barrier and the enhancement of tunneling. The Au was used to improve the current spreading. In addition, the insertion of Ni between Al and Au prevents Au from penetrating into the Al layer and changing its work function. The annealed n-GaN contact layer shows resistivity values in the order of 1×10^{-4} $\Omega.cm^2$.

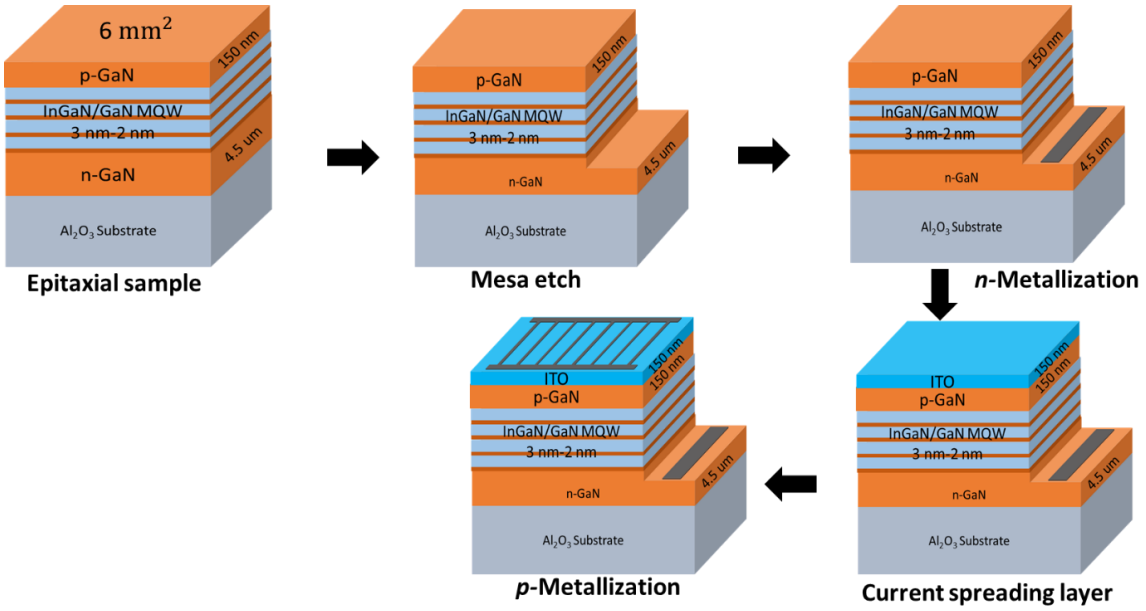

Figure 27. Fabrication sequence of InGaN MQW solar cell presented in this work.

As opposed to the low resistivity of an n-GaN contact, achieving an ohmic p-GaN contact is difficult due to the following possible factors: (1) High activation energy of GaN: Mg, (2) lack of metal contacts with high work functions (~5 eV), and (3) nitrogen vacancies in the p-GaN. Typically, Ni/Au is used as a contact to the p-GaN [172]. Ni acts as a diffusion barrier to Au and can activate the Mg dopants on the surface of the p-GaN. However, it is shown that the contact resistance can be further improved by depositing Ti/Pt/Au on p-GaN [173]. It has been proven that Ti reduces surface contamination when introduced to GaN [174]. Pt was chosen due to its high work function (5.65 eV), and Au was used as a capping layer for better probing and subsequent wire bonding. Further, Ti/Pt/Au is used as a thermally stable contact for InGaN [175]. In order to further improve the lateral conductivity of p-GaN, 150-nm thick indium-tin-oxide (ITO), was deposited on the p-GaN contact layer via e-beam evaporation. After deposition of ITO, the film was annealed at 500 ºC under N_2 flow for 2 minutes. The ITO resistivity and sheet resistance were measured to be ~5×10^{-2} Ω.cm^2 and ~28 Ω/sq, respectively. The thickness of ITO was

selected to increase the electrical conductance and reduce reflectivity and parasitic absorption of light. Figure 28 shows the calculated optical data (reflection, transmission, and absorption) of ITO film throughout the desired wavelength regime. After deposition of the ITO, Ti (15 nm)/Pt (12.5 nm)/Au (200 nm) was deposited on ITO to serve as a metal grid for efficient carrier collection. The contact grids were not annealed. The resistivity and sheet resistance of Ti/Pt/Au deposited on the ITO layer was measured from the TLM analysis to be ~2×10^{-5} Ω.cm^2 and ~51 Ω/sq, respectively. It should be mentioned that this fabrication process requires further optimization with regards to the contact thickness, contact-annealing steps, and sidewall passivation.

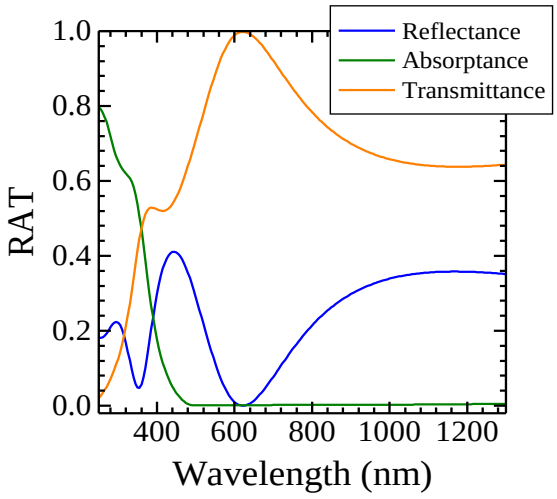

Figure 28. Calculated reflectance, transmittance, and absorptance of a 150 nm ITO layer performed via OPAL 2 software.

The mask layout was designed using L-edit software and was fabricated by a quartz photomask blank coated with chromium and photoresist (see Fig. 29). The grid spacing was optimized to increase the carrier collection and reduce the resistive loss in the fingers. Given the existing device size of 2.2×2.5 mm^2 (CPV size) and 5 microns finger width, optimal finger spacing was calculated to be around 255 microns.

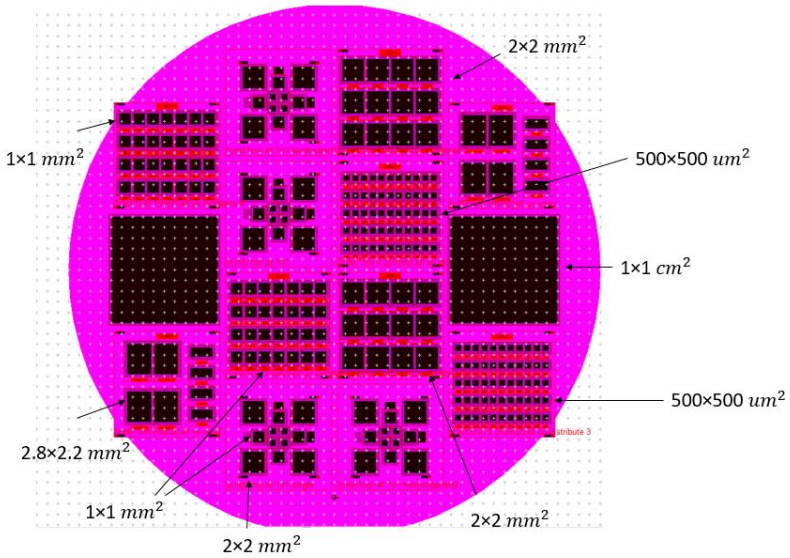

Figure 29. Mask layout of the solar cells with different active areas.

4.3. Device Performance and Analysis

The p-i-n InGaN MQW solar cells presented in this work with 9 and 40 $In_{0.12}Ga_{0.88}N$ (3 nm)/GaN MQWs (herein M9 and M40, respectively) were grown via metalorganic vapor phase epitaxy (MOVPE) at Photonitride corporation. The InGaN well has a theoretical bulk bandgap of $Eg_{25^{\circ}C}$=2.95 eV and $Eg_{600^{\circ}C}$=2.65 eV (based on Varshni's equation (Eq 1.3)). Sample M9 has 5.5 nm-thick QBs whereas sample M40 contains 2.0 nm-thick QBs. The InGaN QWs are UID, and the GaN QBs are lightly Si-doped at ~5×10^{17} cm^{-3} for polarization screening purposes. The active regions were capped with a thin *p*+GaN layer (Mg ≈1×10^{20} cm^{-3}). The surface morphology of the samples shows RMS values of <0.6 nm. The MQW period thickness, the degree of relaxation, and the In composition were all verified using x-ray diffraction technique.

Figure 30 and Table 13 depict the temperature-dependent light current density-voltage (LJ-V), dark J-V (DJ-V), and external quantum efficiency (EQE) characteristics of both samples. LJ-V was acquired using an AM1.5G Oriel class A solar simulator. The V_{OC} of both cells at room temperature show similar values (~2.2 V), however, the short-circuit

current density (J_{SC}) value of M40 (1.38 mA/cm^2) is higher than that of M9 (1.03 mA/cm^2), owing to its higher number of QWs and thinner QBs. The J_{SC} enhancement can be seen in the EQE results. The peak EQE for M40 and M9 are ~71% and ~41%, respectively. The V_{OC} and bandgap (E_G) of both samples linearly decrease with temperature by dV_{OC}/dT of -3 mV/°C and dE_G/dT of -0.5 meV/°C, respectively. However, the J_{SC} of both cells increases with temperature by $dJ_{SC\text{-}M40}/dT$ of ~1.2 µA/°C and $dJ_{SC\text{-}M9}/dT$ of ~1.8 µA/°C. The reduction of V_{OC} and increase in J_{SC} with temperature can be explained by the bandgap narrowing, the increase in the density of absorbable photons, and the increase in TE from the QWs. The EQE(T) results demonstrate two main features: (1) the redshift of the long cut-off wavelengths with temperature (note that sample M9 has higher values) and (2) reduction of spectral utilization (SU) of M40 with temperature, as opposed to M9.

TABLE 13. TEMPERATURE-DEPENDENT LJ-V PARAMETERS (INGAN BANDGAPS (EG) WERE EXTRACTED FROM VEGARD'S LAW).

		Sample M40 (40 MQWs)					Sample M9 (9 MQWs)				
Temp (°C)	E_G (eV)	J_{SC} (mA/cm^2)	V_{OC} (V)	FF (%)	SU (%)	Peak EQE (%)	J_{SC} (mA/cm^2)	V_{OC} (V)	FF (%)	SU (%)	Peak EQE (%)
25	2.95	1.38	2.22	77	39	76	1.03	2.20	55	29	41
150	2.89	1.50	1.82	70	38	73	1.23	1.87	63	32	42
300	2.81	1.65	1.34	61	37	71	1.48	1.39	60	34	44
500	2.69	1.94	0.60	49	36	68	1.91	0.76	55	35	51

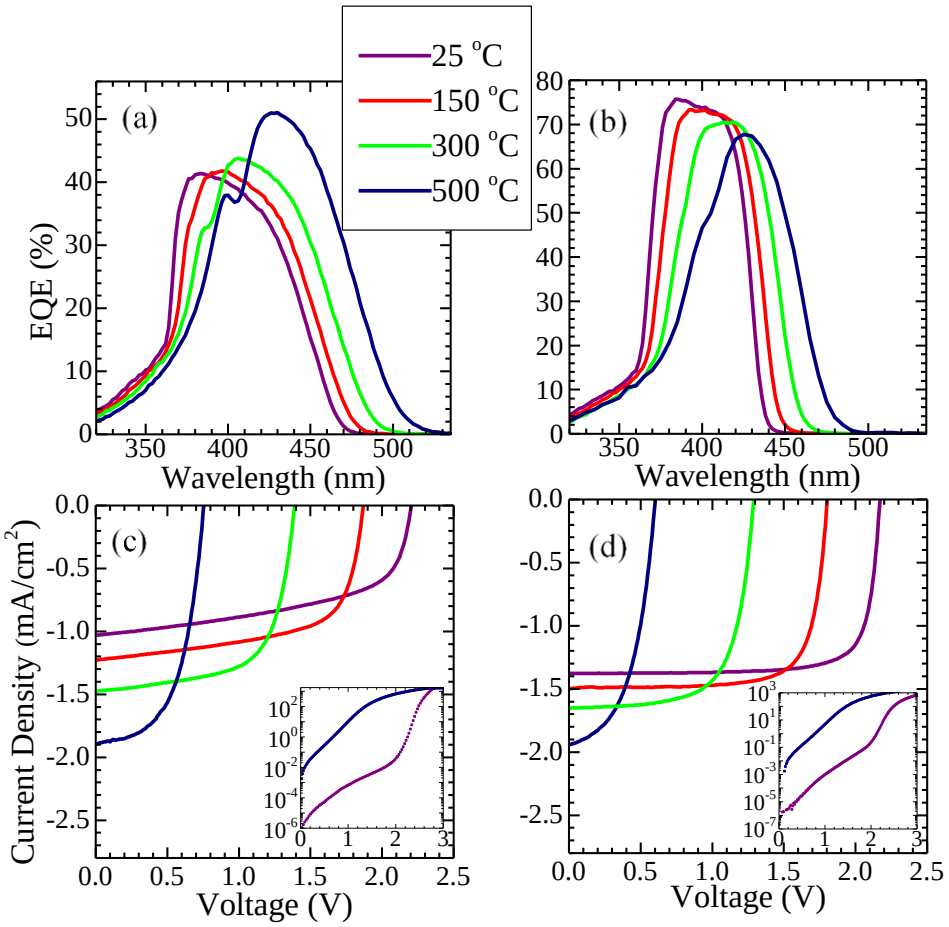

Figure 30. EQE characteristics of (a) M9 and (b) M40. LJ-V curves of (c) M9 and (d) M40. The insets are the DJ-V spectra at 25 and 500 °C.

To understand the higher cut-off wavelengths of M9, the effect of t_b and temperature on the energy band diagram of strained $In_{0.12}Ga_{0.88}N$/GaN MQW is investigated using Nextnano^3 software [176]. The temperature dependence of spontaneous polarization is assumed to be negligible [177], [178]. The effect of temperature on the pyroelectric coefficients (e_{13} and e_{33}) of InGaN-based materials is not fully known and assumed to be negligible. By increasing the t_b, however, the internal electric field within the QW increases, leading to an increase in the tilt of the QW energy band at all temperatures. As a result, the band-to-band transition probability between the conduction (e1) and valance (h1) band ground states reduces, resulting in a reduction of light absorption in M9. The

modeled e1-h1 overlap integral reduces from 0.37 to 0.28 by increasing the t_b from 2.0 to 5.5 nm at 25 ºC, respectively. The redshift with the increased t_b can be seen in the EQE results where the absorption edge redshifts from ~440 to ~470 nm. A similar observation was made by Wantanabe *et al.* and Wierre *et al*. [179], [180]. Although the redshift in M9 could increase the density of absorbable photons, the overall cell performance is negatively impacted by decreased electron-hole wavefunction overlap (reduction of the oscillator strength and increase in QCSE). The EQE results demonstrate the impact of temperature on the absorption edge, showing the long cut-off wavelengths of both cells redshift with temperature (due to bandgap narrowing, see Fig. 30). Figure 31 shows the e1-h1 transition wavelengths of both cells as a function of temperature, which are correlated to the experimental cut-off wavelengths. It depicts that the e1-h1 transition energies of M9 are redshifted compared to that for M40. The results suggest that the absorption throughout the temperature range occurs from the e1-h1 transition. The experimental data appear slightly redshifted in comparison with the calculated values, taking the In and QW thickness fluctuations into account. Such QW inhomogeneity is confirmed by transmission electron microscopy (TEM) images of QWs (Fig. 32), and the non-uniform emission in QWs observed in monochromatic cathodoluminescence intensity maps (not shown here).

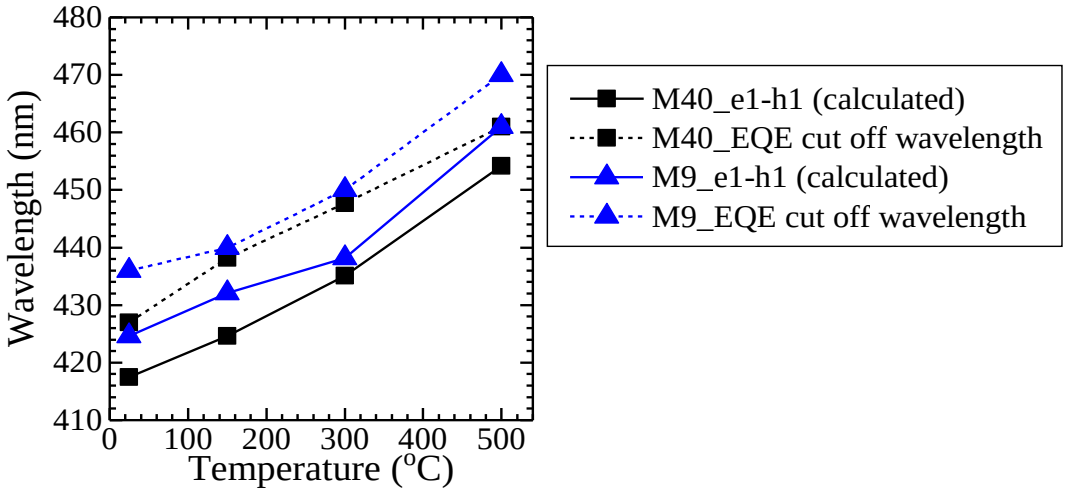

Figure 31. Modeled e1-h1 transition and experimental cut-off wavelengths vs. temperature (cut-off wavelength is defined as the inflection point of EQE at long wavelengths).

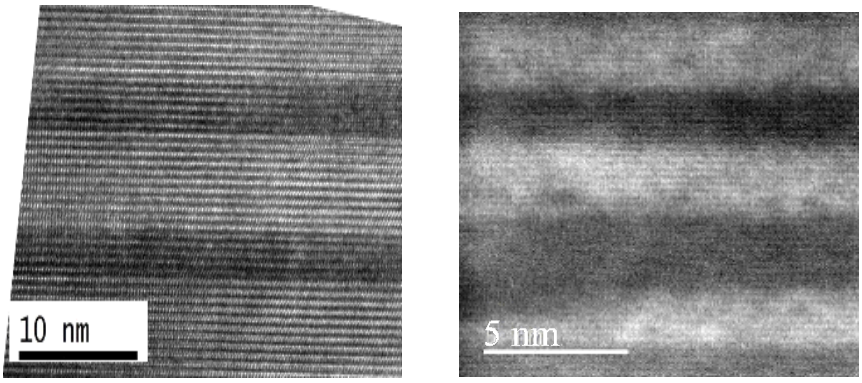

(a) (b)

Figure 32. Cross-sectional TEM images: (a) sample M9 showing sharp InGaN/GaN interfaces without interface inhomogeneity. (b) An upper QWs of sample M40 with an indication of non-uniformity at the interfaces. The TEM results were performed by Prof. Fernando Ponce at Arizona State University.

As the number of QWs increases, the photo-absorption increases, however, the carrier collection efficiency is impeded by material deterioration, minority carrier recombination outside the depletion region, and, consequently, an increase in the leakage current. To extract the leakage current, the DJ-V curves were fit with a double-diode model. The DJ-V curves change from a two-diode model to a single-diode mode at elevated temperatures (T > 300 °C) (see the insets of Fig. 30). The first saturation current density (J_{01}) can be expressed as

$$J_{01}(T) = J_{001} \exp\left(\frac{-\Delta E}{kT}\right), \quad (4.1)$$

where ΔE and J_{001} are the activation energy and exponential prefactor, respectively [140]. The results show that the $J_{01.0\ V}$ values of M40 and M9 increase from approximately 2.4×10^{-19} and 2.1×10^{-23} mA/cm^2 at 25 °C to 1.8×10^{-1} and 1.5×10^{-1} mA/cm^2 at 500 °C, respectively. As seen in the TEM images of Fig. 32, M9 exhibits sharp InGaN/GaN interfaces; however, M40 shows some non-uniform interfaces, particularly towards the upper QWs. It was found that the non-uniformity worsens as the number of QWs further increases, leading to structural deterioration in the form of non-radiative recombination centers, such as V-defects. In addition, thinner barriers can increase the tunneling probability of the photo-generated carriers, as the carrier wavefunctions within the QWs extend into the finite barriers. The combined effects of inferior material quality and thinner barriers of M40 leads to the larger dark current densities [179], [181]. Further, it is found that increasing temperature leads to a reduction of minority carrier lifetime, in part due to the thermal activation of defects, which leads to further carrier loss at high temperatures.

The first ideality factors (n_1~2) of both cells are temperature independent, which is attributed to the minority carrier recombination inside the depletion region and is common for MQW devices. The second ideality factors demonstrate higher values ($n_2 > 2$) that significantly improve (decrease) with temperature. The n_2 values of M9 and M40 linearly decrease from ~10.5 and ~8 at room temperature to ~3.8 and ~4 at 300 °C, respectively. The high ideality factors in GaN-based hetero-junction devices have been associated with defect-assisted tunneling through interface states [182], [183]. The reduction of n_2 with temperature implies that the effect of tunneling becomes less dominant, making the current transport mainly space-charge recombination limited. Therefore, the activation energy of

data from Table 13 plotted as $\ln(J_{01}T^{-2.5})$ vs. 1000/T (not shown here) should be approximately equal to half of the $In_{0.12}Ga_{0.88}N$ bandgap ($E_{G\text{-}25\,^{o}C}$ = 2.95 eV) [140], [141]. Indeed, the extracted ΔE values of both cells are ~1.5 V. This confirms that, regardless of the MQW design, the recombination in the depletion region limits the current transport at elevated temperatures. However, the recombination outside the depletion region is also detrimental as the carriers can recombine in non-depleted QWs because of the small diffusion length and, in turn, reduce the overall carrier collection. These effects make the temperature-dependent depletion region analysis the necessary point of focus in order to better understand the different SU trends of M9 and M40.

To acquire the temperature-dependent depletion width, the capacitance (C_P) data were extracted from the AC response of the cell using impedance spectroscopy (IS). Figure 33(a) depicts the IS spectra of M40 in a *Real* Z (R) vs. -*Img* Z (-X) Nyquist plot at varying bias voltages taken at room temperature. The displacement of the curves along the *Real* Z axis indicates the existence of series resistance (R_S), and the negative values on the *Img* axis (-X) at high frequencies is an indication of a series inductance (L_S), most likely due to the parasitic connecting wires [184]. The R_S originates from the contact, connecting wires, and quasi-neutral region resistances [185]–[187]. The diameter of the semicircle indicates a parallel resistance (R_P), which signifies the pn junction resistance. Thus, to accurately analyze the AC impedance behavior of the cell, the equivalent circuit should consist of series connected R_S and L_S Voigt elements coupled to a parallel to R_PC_P. Failure to do so will result in the erroneous voltage dependence of the capacitance, known as negative capacitance (NC) [187]. The total impedance (Z = R + jX) can then be expressed as

$$Z = R_s + j\omega L_s + \frac{R_p}{j\omega R_p C_p + 1}. \tag{4.2}$$

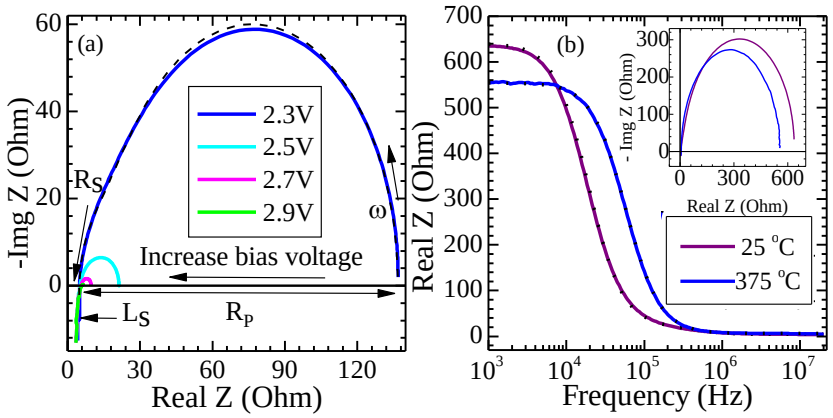

(a) (b)

Figure 33. (a) Impedance complex plane of M40. (b) Temperature-dependent real Z vs. frequency measured at V = V_{OC} of M40 (the inset shows the complex planes). The fitted lines are shown in dashed lines.

The C_P is intrinsic device capacitance, and R_P is comprised of the resistances associated with the surface (R_{Sur}), shunt (R_{Shunt}), and radiative (R_{Rec}) recombination. The device frequency response can then be fitted by the aforementioned equivalent circuit to extract L_S and R_S values. Figure 33(b) depicts *Real* Z of M40 vs. frequency at 25 and 375 °C (V_{bias} = V_{OC}). The extracted L_S and R_S values for M40 are ~1.06×10^{-7} H and ~5.0 Ω at room temperature. The same analysis for M9 results in values of L_S ~1.07×10^{-7} H and R_S ~10.9 Ω. By increasing temperature, R_{Shunt} decreases and the leakage current density increases, both of which lead to the reduction of R_P ($R_P \cong [(1/R_{Shunt}) + (1/R_{Rad\ Rec})]^{-1}$) and, eventually, degradation of the cell performance. Also, R_S and L_S are found to be essentially temperature independent, showing values of ~6.2 Ω and ~1.07×10^{-7} H at 375 °C. The device capacitance (C_P) can then be expressed as follows

$$C_P = \frac{\omega L_s - X}{(R_s - R)^2\left(1 + \left[\frac{\omega L_s - X}{R_s - R}\right]^2\right)}. \qquad (4.3)$$

Figure 34 depicts the extracted temperature-dependent C-V data of both cells at 100 kHz modulation frequency compared to the LCR meter results (which considers just a

parallel R_PC_P as the equivalent circuit). Around the V_{OC} points, the capacitance increases and the NC is not observed, which is in agreement with the theory developed by Laux *et al.* [188]. The NC (acquired from the LCR meter) is in contradiction to the conventional Shockley's *pn* junction model [189]. The NC has been associated with activation of sub-bandgap defects [190], Poole-Frenkel effect [191], and junction effect [192]. Here, the NC is a byproduct of the device conductance ($1/R_P$) dominating over its intrinsic capacitance (C_P), leaving only the parasitic inductance (L_S) as the remaining reactive component.

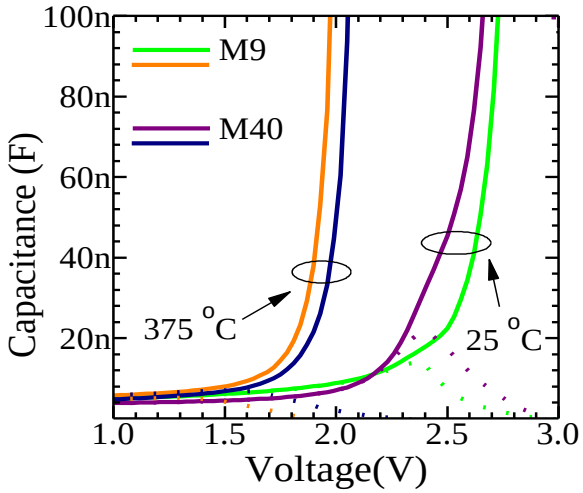

Figure 34. Temperature-dependent C-V. The capacitance data measured by an LCR meter is represented by the dotted lines.

The depletion capacitance (C_{Dep}) was deconvoluted from C_P at high frequencies to extract *W*:

$$W = \frac{\varepsilon_r \varepsilon_0 A}{C_{dep}}, \tag{4.4}$$

where ε_r and ε_0 are the relative and vacuum permittivities ($\varepsilon_{r-GaN} = 8.9$), respectively, and *A* is the area of the cell [193]. Figure 35(a) shows the extracted depletion widths as a function of voltage and temperature. At a given voltage, as temperature increases, the W and, consequently, the number of depleted QWs available for PV charge separation reduces (n_i is inversely proportional to the *W*). At zero bias, the depletion widths of M9 and M40

reduce from ~132 and ~110 nm at 25 °C to ~125 and ~107 nm at 375 °C, respectively. The MQWs of M40 is partially depleted throughout the temperature range. However, all the QWs of M9 are depleted at 25 °C but get partially depleted at higher temperatures and biases.

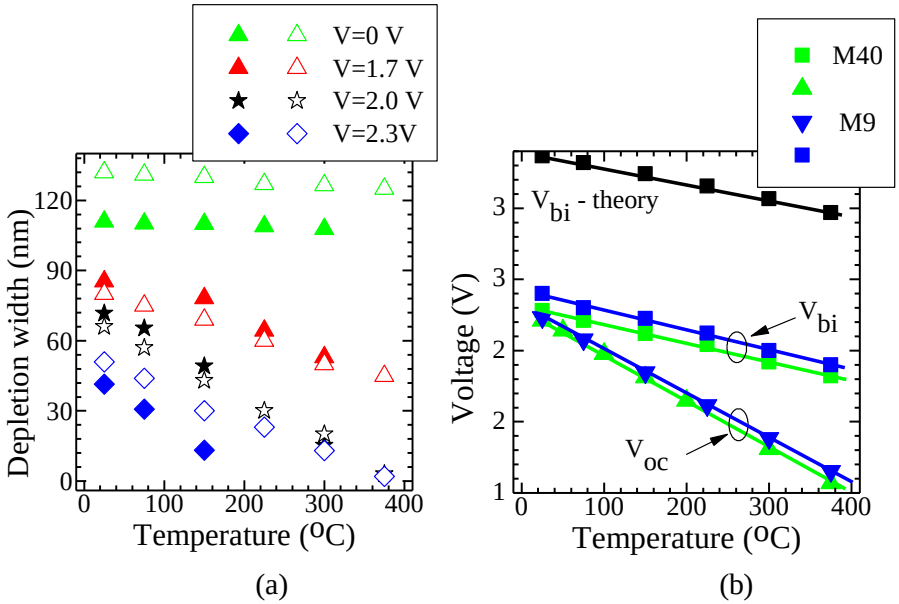

Figure 35. (a) Depletion width vs. temperature for different bias conditions. The empty and filled symbols represent the depletion widths of M9 and M40, respectively. (c) The V_{OC}, measured V_{bi}, and theoretical V_{bi} of M9 and M40.

The existence of partially depleted QWs in M40 leads to the reduction in the carrier collection efficiency as diffusion becomes the main collection mechanism outside the depleted area, where minority carriers can recombine due to their low diffusion length and high capture cross section in the QWs. Further, as temperature increases, the minority carrier lifetime reduces, leading to a further reduction in carrier extraction. Thus, it is likely that reducing the number of QWs in M40 can decrease the minority carrier recombination rate. In other words, optimizing the number of QWs based on the depletion width is crucial for increasing the J_{SC}. It is noteworthy that the W at elevated temperatures, and near the MPP, must be considered for the optimal design of the MQW. However, regardless of the

number of QWs, there will be non-depleted QWs at MPP at high temperatures, leading to higher carrier loss.

The TE is strongly dependent on the temperature; however, the tunneling is temperature independent and exponentially depends on the t_b. At room temperature, the main transport mechanism in M40 with a thinner barrier is tunneling, whereas, the tunneling rate is significantly lower in M9 due to its thicker barrier [194]. The reduction of the depletion width with temperature, which is a measure of stored charge in the depletion region, corroborates that the TE increases with temperature. The TE enhancement with temperature can also be seen in Fig. 34 as the C_P and, consequently, diffusion capacitance (C_{Dif}), increases at a fixed bias, confirming the supposition that thermal escape from the QWs is enhanced at elevated temperatures. The combined effects of TE and recombination outside the depleted region can be seen in the J_{SC} trends with temperature. Although the MQW region of M40 is ~2.7 times thicker than that of M9, at 500 °C the J_{SC} (~1.91 mA/cm^2) of M9 reaches the J_{SC} of M40 (~1.94 mA/cm^2), implying that carrier recombination outside the depletion region in M40 are significant at high temperatures. The lower dJ_{SC}/dT of M40 can be better understood by considering the SU, given in Table 13. The SU of M40 decreases with temperature, whereas, the SU of M9 improves with temperature. Two competing effects can explain the inverse SU behavior of M40 with temperature. On the one hand, the photo-absorption and TE increase with temperature. On the other hand, carrier collection efficiency is hampered due to the increase in the carrier recombination in the non-depleted regions and the thermal activation of defects.

Figure 35(b) shows a comparison between V_{OC}, the measured built-in potential (V_{bi}), and the theoretical V_{bi}. The measured V_{bi} is a projected realistic limit for V_{OC}. At room

temperature, the V_{OC} values are close to the measured V_{bi}, values indicating that the near-optimal voltage is realized. However, by increasing temperature, the V_{OC} of both cells degrade faster (dV_{OC}/dT = -3 mV/°C) than the measured V_{bi} ($dV_{bi\text{-}M40}/dT$ = -1.32 mV/°C and $dV_{bi\text{-}M9}/dT$ = -1.3 mV/°C). This deviation of V_{OC} from the V_{bi} indicates a significant loss of voltage compared to the realizable limit, possibly due to the thermal activation of mid-bandgap defects and an increase in the leakage current [125]. The measured V_{bi} generally trends with the theoretical V_{bi} but is found to be offset by ~1.0 V. The theoretical V_{bi} assumes that the dopants are fully ionized. This offset can be reduced by improving the hole concentration of the p-region.

4.4. Conclusion

The temperature-dependent performance of $In_{0.12}Ga_{0.88}N$/GaN MQW solar cells and the influence of the number of quantum wells (9 and 40) and the QB thickness on the carrier extraction were studied. It was seen that the absorption edge redshifts by increasing the quantum barrier thickness; however, the overall absorption reduces due to the reduction in e1-h1 wavefunction overlap. Although the 40 MQW cell has a higher photo-generated carrier density, it has higher recombination losses due to its partially depleted active region and inferior material quality. These results indicate that for achieving high-performance InGaN solar cells designed to operate at high temperatures, the MQW region should be optimized to increase carrier collection, balancing absorption with recombination.

CHAPTER 5
NITRIDE-BASED TUNNEL DIODES

5.1. Motivation

The III-nitride material system can be widely used for different optoelectronic devices such as LEDs, solar cells, and lasers. Although there have been numerous attempts at increasing the efficiency of nitride-based optoelectronic devices, they encounter multiple challenges, such as low hole concentration, high contact resistance, and high sheet resistance, which need to be addressed. Conventional LEDs, lasers, and solar cells utilize transparent conductive oxide, such as ITO, on top of the p-GaN layer as a current spreading layer. However, using a TCO layer can introduce some complications to device fabrication and high optical losses. The TCO layer can be replaced by a nitride-based tunnel junction to convert the p-type contact layer to an n-type contact layer. Nitride-based tunnel junction can be achieved via low-resistance inter-band tunneling enabled by heavily doped GaN layers.

Inter-band (band-to-band) tunnel diode has a broad range of applications for optoelectronic and electronic devices and has been extensively investigated since Esaki's discovery of the quantum tunneling phenomenon in a degenerately doped Ge pn diode [195]. The inter-band tunneling can be achieved by heavily doped p- and n-type regions of a pn junction. By increasing the doping concentration at the junction, the depletion and, consequently, the tunneling barrier height reduce, leading to tunneling of carriers between the conduction band and the valence band. However, by increasing the bandgap, the intrinsic carrier concentration and doping ionization efficiency reduce, resulting in the

reduction of tunneling probability. Thus, achieving an Esaki-style tunnel diode in wide bandgap materials (such as GaN with a bandgap of 3.42 eV) is remarkably challenging.

Different approaches have been demonstrated to achieve tunneling in nitride-based materials. Polarization-assisted heterojunction tunnel diodes, such as GaN/InGaN/GaN and GaN/AlN/GaN, have been reported, in which a large internal electric field is created across the junctions due to the polarization dipoles to increase the tunneling probability [196], [197]. It was demonstrated that the GaN/InGaN/GaN TJ could reach a low specific series resistance of ~10^{-4} Ω.cm^2 [198]. However, hetero TJ designs are sub-optimal for solar cells and LEDs due to a high absorption loss introduced by the InGaN layer and a low current density that results from the large bandgap of the insulating AlN layer. Defect-assisted tunneling through the introduction of midgap states in the depletion region was previously investigated but resulted in high overall series resistances and low device reliability [199], [200]. Thus, successful demonstration of pn GaN homojunction tunnel diode is desirable to overcome the aforementioned drawbacks. Tunnel junction enabled devices have been demonstrated such as InGaN miro-LEDs with heavily doped GaN tunnel junctions with doping concentrations of 1×10^{20} cm^{-3} for Mg and 2×10^{20} cm^{-3} for Si [201]. Akyol *et al.* used GaN/GdN/GaN tunnel contact for a GaN pn diode, showing an average series resistance of 5.7×10^{-4} Ω.cm^2 and GaN/InGaN/GaN tunnel junctions in a triple-junction LED, operating at 9.09 V under 10 A/cm^2 with a differential resistance of 6.31×10^{-2} Ω.cm^2 [202], [203]. Leonard *et al.* demonstrated an m-plane III-nitride vertical-cavity surface-emitting laser with a hybrid III-nitride tunnel junction intracavity contact, where an n-GaN contact layer was grown via ammonia MBE on an MOCVD grown p-GaN layer [204]. In the case of ultra-UV LEDs, a p-GaN contact layer, which degrades the total series

resistance and increases the optical absorption loss, can be replaced by a wide bandgap AlGaN-based tunnel junction with the structure of p-AlGaN/InGaN/n-AlGaN [205].

MOCVD has shown improved LED contact resistance using GaN homojunction tunnel contacts in place of p-GaN contact layers, but multiple attempts have been unsuccessful in demonstrating low-resistance stand-alone pn GaN homojunction tunnel diodes [206], [207]. The fundamental challenges associated with the MOCVD growth, such as low Mg activation efficiency in p-(Al)GaN, Mg memory effect, and hydrogen passivation of Mg, impose a substantial constraint on the growth of nitride-based TJs. However, the challenges above do not exist in plasma-assisted molecular beam epitaxy (PAMBE). Recently, GaN pn homo TJs have been successfully realized by PAMBE, showing negative differential resistance and intrinsic Zener characteristics [208], [209]. In particular, due to the absence of hydrogen in PAMBE, p-(Al)GaN layers are not passivated by hydrogen atoms, which eliminates the need for an activation anneal. In addition, a minimal Mg memory effect and a favorable low-temperature chemistry for Mg incorporation on substitutional sites, lead to high hole concentrations in excess of 1.2×10^{20} cm^{-3} in GaN, as reported using the metal-modulated epitaxy (MME) growth method [5], [38], [39], [210]. Similar growth technique was used to achieve high hole concentrations in AlGaN films [5]. The use of low-temperature MME growth technique reduces the incorporation of nitrogen vacancies and donor-like defects accountable, in part, for hole compensation. These effects make MME a promising growth method to achieve low-resistance TJs.

In this work, GaN homojunction tunnel diodes with different doping profiles were grown via MME growth technique. First, we discuss the properties of highly doped GaN films via MME. Next, the tunneling behaviors of grown GaN tunnel diodes (including

Zener at reverse bias and negative differential resistance) are discussed. Finally, wide bandgap AlGaN homojunction tunnel diodes with Zener characteristics are demonstrated.

5.2. Growth of Highly Doped GaN Films via Metal Modulated Epitaxy

A systematic study was performed to investigate n- and p-GaN films with the high free carrier concentrations required for low resistance tunnel junctions. MME growth technique was used to grow doped GaN films in MBE. MME is a growth technique in which metal shutters (*e.g.*, Ga, In, and Al) are modulated with a fixed duty cycle while a constant plasma nitrogen flux is supplied. By modulating the shutters, the film surface alternates between N- and metal-rich conditions, leading to high carrier concentrations [38]. In this section, the growth mechanisms of the doped GaN films via MME and the associated RHEED patterns are presented. The electrical and material characteristics of the grown films are analyzed to make a correlation between the growth condition and the film quality.

5.2.1. Experimental Procedure

The doped GaN samples were grown on single polished c-plane Lumilog semi-insulating (SI) GaN: Fe (0001) templates on sapphire via Riber 32 PAMBE with a base pressure of ~10^{-10} Torr. The backside of the substrates was coated with a 2 µm-thick tantalum (Ta) using DC sputtering to ensure homogenous heat distribution across the substrates during the growth. Prior to the growth, the templates were cleaned using a Piranha solution to remove the organic residues. The templates were first outgassed in two stages: in the MBE introductory chamber at 200 ºC for 20 minutes and in the MBE growth chamber at 600 ºC for 10 minutes. The subsequent doped GaN films were then grown in the high vacuum MBE growth chamber. Reactive nitrogen species were supplied via a UNI-Bulb RF plasma source manufactured by Veeco and operated at RF power of 350 W

and N_2 flow of 1.3 sccm. Al, In, and Si sources were supplied using standard effusion cells. Mg and Ga were supplied via a Veeco valved cracker and a Veeco SUMO effusion cell, respectively.

5.2.2. N-type GaN Growth via MME

Nitrogen vacancies, oxygen, Ge, and Si behave as donors in GaN films [211]. Si is a good candidate due to its shallow activation energy, low formation energy, and a high degree of solubility. In this work, the GaN: Si samples were grown at 600 ºC with 10 s open / 10 s closed Ga duty cycles and a growth rate of 0.98 µm/h. Similar to the nitrogen, Si shutter was unmodulated during the growth, as Si does not segregate on the surface. The Ga flux was adjusted during the growth to keep the III/V of ~1.8, and the temperature of the Si effusion cell varied from 1100 to 1250 ºC. The surface kinetics were analyzed using RHEED patterns, and the MME growth was monitored real-time using transient RHEED signal. Figure 36 shows the transient RHEED intensity with different portions of the modulation scheme. In MME growth method, the metal fluxes which are higher than the stoichiometric fluxes result in accumulated metal adlayers and, consequently, enhanced surface diffusion. The accumulated metal adlayers are consumed by impinging nitrogen flux while the metal shutters are closed. It is worth mentioning that Si does not introduce a perturbation in the kinetics of Ga atoms, as Si does not segregate on the surface (unlike Mg). Further details on the MME growth method can be found in the earlier works [39], [212], [213].

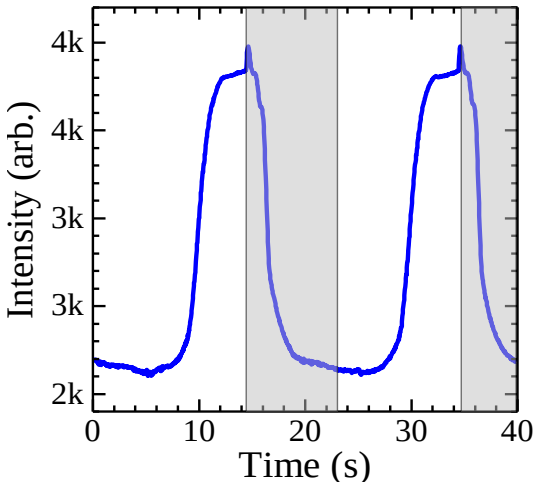

Figure 36. A transient RHEED intensity of the grown n-GaN film via MME. The graded regions show the Ga shutter open portion of the modulation scheme.

The electrical properties of 500 nm-thick GaN: Si films grown by MME were acquired by Hall-effect measurement using a 0.3 T fixed magnet at room temperature. Figure 37 depicts the resistivity, mobility, and electron concentration of the grown samples vs. Si temperature. It is shown that by increasing the Si temperature from 1100 to 1250 ºC, electron concentration increases from 8×10^{18} to 4×10^{20} cm^{-3} while mobility reduces from 175 to 75 cm^2/Vs, respectively. The increased electron concentration with Si doping shows a high incorporation rate of the impinging Si atoms enabled via MME growth technique. At low electron concentrations, the mobility is restricted by charged dislocation scattering, whereas, at high electron concentrations, the mobility is restricted by scattering of ionized impurities [214], [215]. Finally, as expected from the electron concentration trend, resistivity reduces from 5×10^{-2} to 2×10^{-4} Ω.cm with increasing the Si temperature.

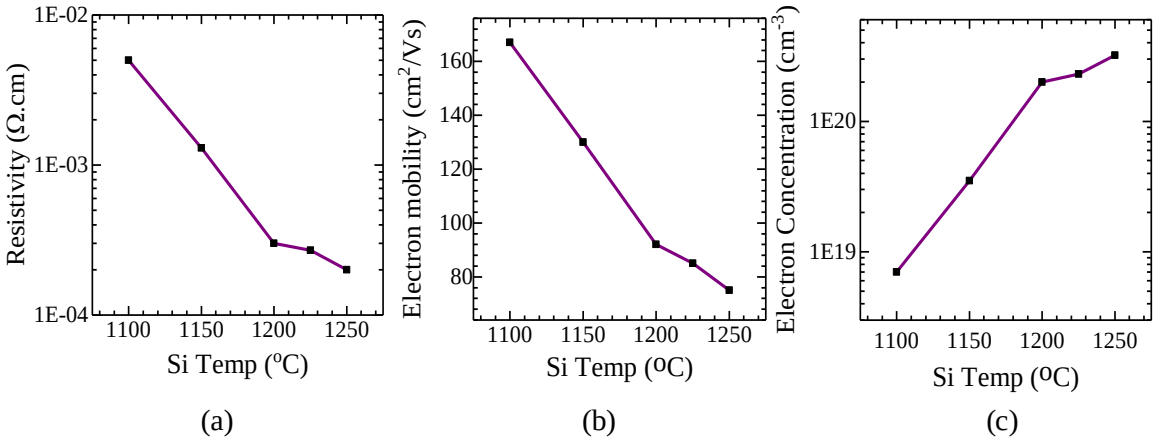

Figure 37. (a) Resistivity, (b) electron mobility, and (c) electron concentration of the grown GaN: Si samples as a function of Si temperature.

In order to investigate the material quality of the grown GaN: Si samples, AFM and XRD measurements were performed. The rocking curves (RCs) around (102) and (002) diffraction angles and 2θ scans were measured to analyze the crystalline quality of the doped sample. The FWHM of the RCs and the diffraction positions of the 2θ scans are shown in Fig. 38. As seen, the FWHM values and GaN diffraction positions are not a function of the Si doping level, indicating that the crystal structure of GaN (*i.e.*, lattice constants and strain) is not changed by incorporation of high Si concentrations; except the highest doped GaN: Si sample which show peak broadening for both ω RCs. It is reported that high Si doping of GaN in excess of 10^{19} cm^{-3} (*i.e.*, above the Mott transition in GaN) creates surface roughening and cracks due to tensile strain [216]. However, the AFM images of the grown films show smooth surface morphologies with no visible cracks (see Fig. 39). The AFM images show hexagonal spiral hillock structures with monolayer traces. These traces are an indication of step flow growth which can be formed around the dislocations. These hexagonal spiral hillocks are shown to be dominant in MBE-grown GaN films [217]. The smooth surfaces of the GaN layers were confirmed via 2×2 reconstruction RHEED patterns (not shown here).

As a summary, the Si concentration of 4×10^{20} cm^{-3} was achieved by controlling the kinetics of Si incorporation into GaN using Ga-rich and low substrate temperature conditions enabled via MME growth method. This method can be a stepping stone towards achieving low-resistance GaN tunnel junctions. Note that Ge can be used to produce even higher carrier concentrations in GaN with satisfactory crystal qualities as Ge has a shallow donor level (~31 meV), and its ionic radius is close to that of Ga. Thus, Ge can occupy the Ga sites and cause less strain, as opposed to Si atoms [218], [219]. Our previous work has shown GaN: Ge films with electron concentrations in excess of 4×10^{20} cm^{-3} [69].

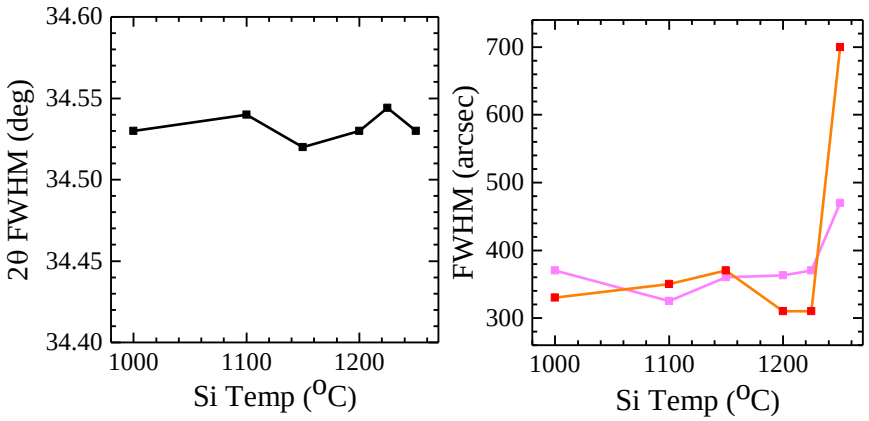

Figure 38. (a) 2θ diffraction positions of the grown Si-doped GaN vs. Si effusion cell temperature. (b) FHWM values of the grown Si-doped GaN around the (002) and (102) reflections vs. Si effusion cell temperature.

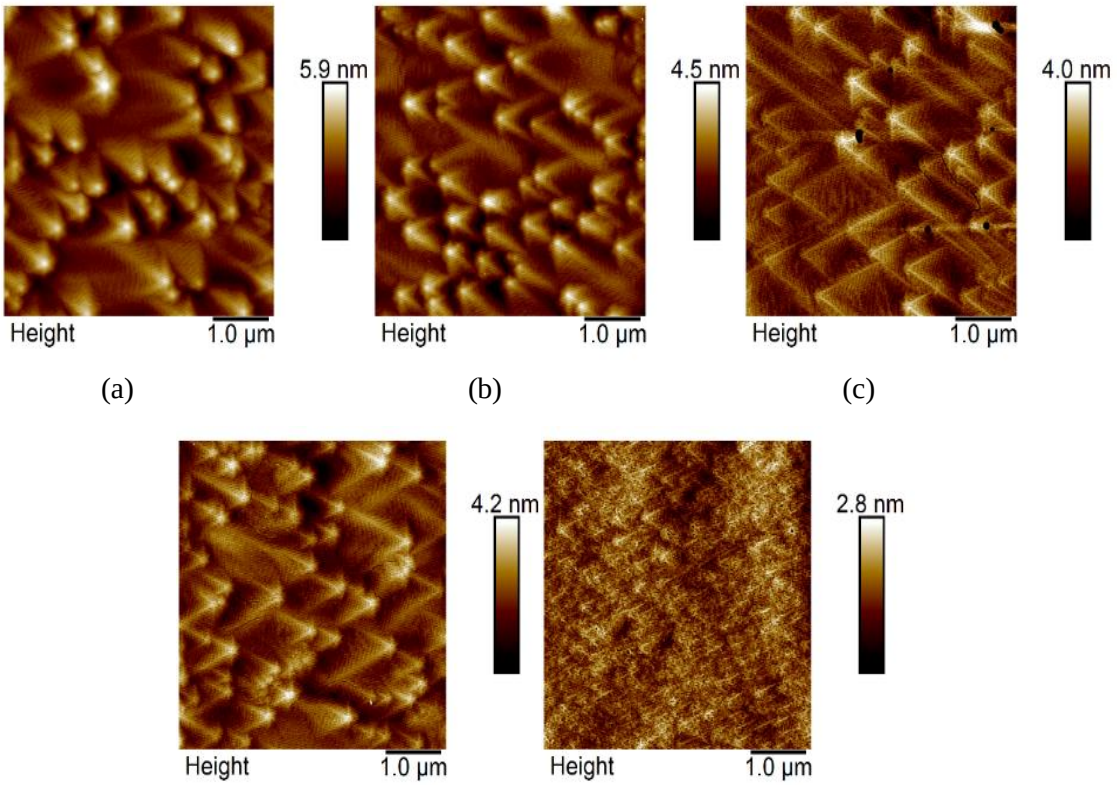

Figure 39. AFM images of the GaN: Si samples with different Si effusion cell temperatures: (a) 1100 ºC, (b) 1150 ºC, (c) 1200 ºC, (d) 1225 ºC, and (e) 1250 ºC.

5.2.3. P-type GaN Growth via MME

Achieving good crystalline quality of GaN film with a high hole concentration is crucial for the improvement of the next generation of tunnel contacted nitride-based devices. It is shown that hole concentrations beyond 10^{20} cm^{-3} with resistivities as low as 0.2 Ω.cm, no Mg precipitants, and inversion domains can be achieved via MME growth technique [5]. MME can control the kinetics of Mg incorporation into the lattice substitutional sites through metal- and N-rich conditions at low growth temperatures [39], [212], [213], [220]. The low growth temperature condition can reduce alloy fluctuation and improve In and Mg incorporation.

Under metal-rich growth condition, the amount of N atoms on the surface, which can act as diffusion barriers, reduces and metal adatom mobility increases, leading to a 2-dimensional (2-D) step flow growth. The 2-D step flow growth occurs when the mean distance between the binding sites is shorter than the diffusion length, causing efficient incorporation of Ga atoms and avoiding statistical roughing of the surface [56]. It is also reported that the increased Ga adatom mobility under metal-rich condition assists Ga to be trapped in the wurtzite *hcp* sites resulting in the reduction of stacking faults [56]. Mg solubility in GaN is the main limiting factor, which mostly arises from competition between the formation of Mg_3N_2 and Mg incorporation as an acceptor [221]. Under the N-rich condition, the density of V_Ns (nitrogen vacancies), as compensating centers to Mg, is lower than that of the metal-rich condition. It is also known that under the N-rich condition, the formation energy of Mg_{Ga} (Mg in substitutional Ga site) is lower than that of Mg_N or interstitial sites (Mg_i) [222]. Nevertheless, the adatom surface diffusion length reduces under the N-rich condition, leading to crystalline defects (such as surface faceting and stacking faults). Thus, by periodic oscillation between N- and metal-rich growth conditions, GaN: Mg can utilize the benefits of both growth conditions. It is experimentally shown that the MME growth method can reduce the density of point defects, leading to a lesser degree of compensation caused by nitrogen and gallium vacancies [221]. In addition, Gunning *et al*. reported that GaN: Mg films grown via MME show negligible carrier freeze-out attributed to impurity band conduction [39].

In this work, a series of 100 nm-thick GaN: Mg films with different Mg doping concentrations were grown on AlN buffer layers grown on GaN: Fe templates at 600 ºC with 10 s closed / 5 s open duty cycles, III/V of 1.3, and a growth rate of 0.98 µm/h. The

low III/V and the short open time are shown to improve the material quality and Mg incorporation [5]. The active nitrogen was supplied by Veeco UNI-Bulb RF plasma source with an RF power of 350 W and an N_2 flux of 1.3 sccm. The Mg and N shutters were open during the growth while the Ga shutter was modulated. The Mg base temperature was varied from 230 to 260 ºC, while the tip temperature was kept constant at 900 ºC. The transient RHEED signal was used to characterize the film *in-situ* (in particular, for adjustment of III/V).

Figure 40 shows the transient RHEED signal intensity of an MME grown GaN: Mg sample. As the Ga shutter opens, the RHEED intensity reduces due to the formation of excess Ga on the surface. By closing the Ga shutter, the intensity increases as the Ga adlayers get consumed by impinging active nitrogen species and recover to the starting value prior to the GaN growth.

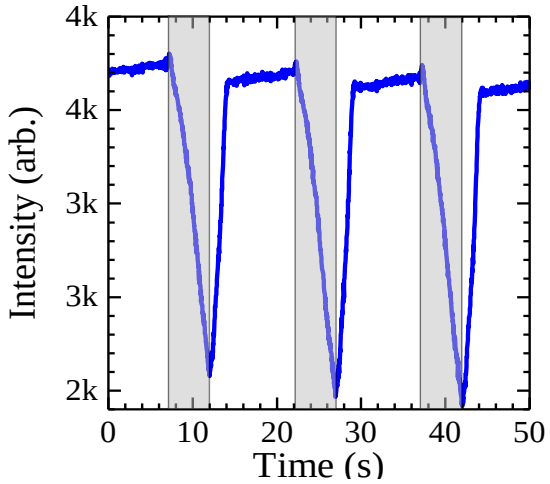

Figure 40. A transient RHEED intensity of a p-GaN film grown via MME growth technique. The graded regions show Ga shutter open portion of the modulation scheme.

SIMS analysis was performed to determine the Mg concentration in the p-GaN samples. The Mg concentration increases from ~1.5×10^{20} to ~7×10^{20} cm^{-3} by increasing the Mg base cell temperature from 230 to 260 ºC. The Mg doping level is beyond the solid solubility of Mg in GaN [4], [222]. However, it is shown that this thermodynamic limitation

can be overcome by kinetically "trapping" the Mg into the substitutional lattice sites by low-temperature MME growth method, resulting in meta-stable super-saturation acceptors [5]. Figure 41 depicts the electrical characteristics of the MME grown GaN: Mg films, measured via Hall-effect (based on Van der Pauw method). The highest hole concentration was achieved at an Mg base cell temperature of 250 ºC, showing a hole concentration of ~1.7×10^{20} cm^{-3} (leading to an activation efficiency of more than 50%) with a resistivity of 0.11 Ω.cm and mobility of 0.4 cm^2/Vs. At an extremely high Mg concentration of ~7×10^{20} cm^{-3}, the hole concentration reduces to ~4.2×10^{19} cm^{-3} and the resistivity increases to 0.12 Ω.cm. The degradation of electrical properties at the highest doped sample can be due to the reduction of surface diffusion length and suboptimal Mg incorporation into Ga substitutional sites. The highest doped sample showed a grainy surface morphology, which is dramatically different from that of GaN: Si films, with an RMS value of ~1.3 nm and no indication of Mg clustering (see Fig. 42). The observed pits at the surface are believed to be related to the defective AlN/GaN interface. The RHEED pattern of the highest doped GaN: Mg film showed streaky and spotty patterns which confirms the AFM observation.

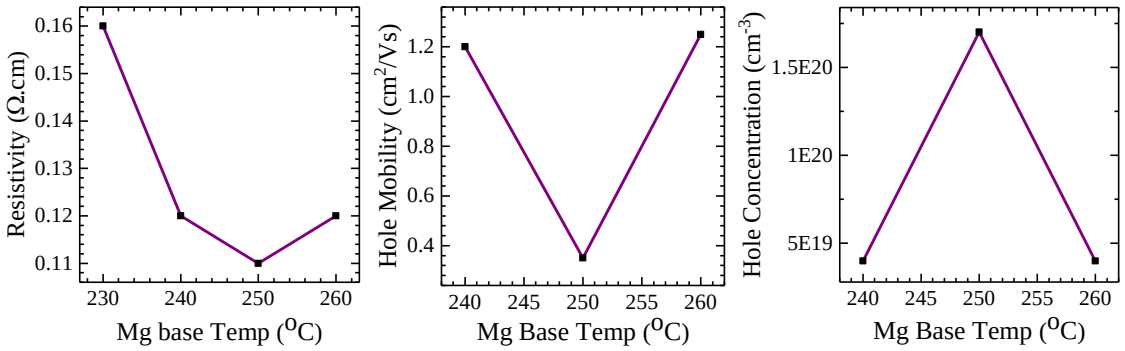

Figure 41. (a) Resistivity, (b) hole mobility, and (c) hole concentration vs. Mg bulk cell temperature of the grown GaN: Mg films.

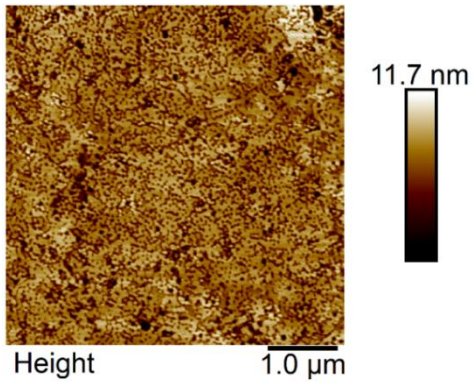

Figure 42. A 5×5 AFM image of the highest doped GaN: Mg film with an Mg concentration of ~7×10^{20} cm^{-3} showing a smooth surface with an RMS value of 1.3 nm and no observable pits.

5.3. Nitride-based Homojunction Tunnel Diode

5.3.1. GaN Homojunction Tunnel Diode

The achieved highly doped n- and p-type GaN via low-temperature MME growth technique can lead to low-resistance nitride-based tunnel junctions and, eventually, development of high-efficiency optoelectronic devices such as multijunction InGaN solar cells, RGB LEDs, and UV lasers. In this work, efforts have been made to grow, fabricate, and characterize GaN homojunction tunnel diodes with Zener and negative differential resistance characteristics. Forward and reverse tunneling current densities were shown to increase as the Mg doping concentrations increased. It is also found that the primary source of tunneling is defect-assisted tunneling, rather than Esaki-style band-to-band tunneling.

All the GaN pn homojunction tunnel diodes discussed here are grown on Saint-Gobain Lumilog MOCVD-grown n-type c-plane GaN (0001) templates on sapphire via Riber 32 PAMBE reactor. The samples consist of 100 nm-thick GaN: Si (Si=1.9×10^{19} cm^{-3}), p++/n++ tunnel junction, 130 nm-thick GaN: Mg (Mg=1.4×10^{20} cm^{-3}), and 20 nm-thick GaN: Mg contact layer (Mg=2×10^{20} cm^{-3}). The tunnel junction (TJ) include a 20 nm-thick GaN: Mg and a 20 nm-thick GaN: Si with a Si doping of ~3×10^{20} cm^{-3}. The Mg doping

level at the junction was varied from ~1.5×10^{20} to ~7×10^{20} cm^{-3}. All the doping levels were calibrated with a separate doping calibration sample (measured via SIMS). Figure 43 shows a schematic of the epitaxial stack of the grown diodes. Table 14 summarizes the Mg and Si doping levels used at the tunnel junctions.

Figure 44 shows RHEED patterns at various growth stages of sample Mg5 (with the highest doping concentration), showing streaky patterns during the n-GaN growth at the junction, which is an indication of smooth surfaces, and spotty and elongated patterns during the p-GaN growth at the junction, indicative of rougher surfaces. However, the rough surface of the p-GaN layer recovered after growing n-GaN layers, as seen by streaky 2×2 RHEED patterns. The smooth surface of sample Mg5 was verified via AFM, showing an RMS value of ~1.3 nm (see Fig. 45). Surface morphology of sample Mg5 showed no pits, unlike the p-GaN samples grown on AlN. The XRD analysis also showed a low defect density and no significant extended defects in the bulk. However, further measurements are essential to analyze the material quality of the grown diodes, including defects at the junction, regrown surface quality, and dislocation types.

The tunnel diodes were fabricated into devices with different mesa dimensions using conventional photolithography and inductively coupled plasma (ICP) etch processes. Ti (30 nm)/Al (100 nm)/Ti (30 nm)/Au (50 nm) and Ni (50 nm)/Au (50 nm) were deposited via e-beam evaporation as contacts to n- and p-GaN layers. The contacts were not annealed due to the high doping concentrations of the contact layers, which is a unique property.

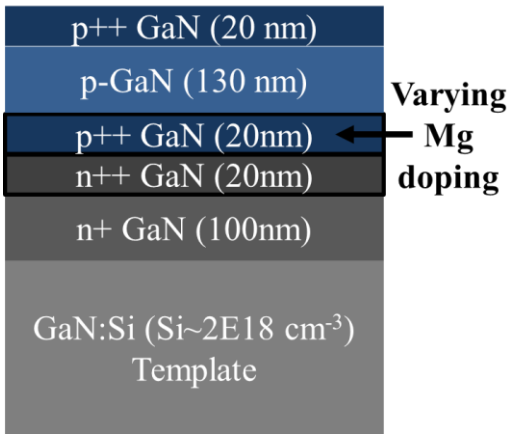

Figure 43. A tunnel diode schematic of pn homojunction tunnel diodes with varying Mg doping concentrations at the junction.

TABLE 14. THE MG AND SI DOPING CONCENTRATIONS EXTRACTED FROM SIMS ANALYSIS PROVIDED FROM EAG ANALYTICAL GROUP.

#	ID	TJ Si concentration (cm^{-3})	Mg base cell temp (^{o}C)	TJ Mg Concentration (cm^{-3})
R474	Mg1	4×10^{20}	230	1.5×10^{20}
R473	Mg2	4×10^{20}	240	2.5×10^{20}
R498	Mg3	4×10^{20}	250	3.5×10^{20}
R475	Mg4	4×10^{20}	260	5.5×10^{20}
R499	Mg5	4×10^{20}	270	6.3×10^{20}

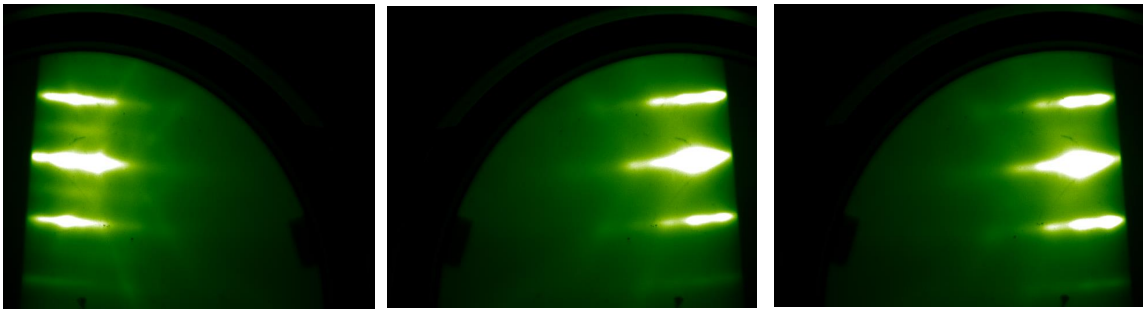

(a) (b) (c)

Figure 44. RHEED patterns at various growth stages of sample Mg5 with the highest doped TJ layer: (a) during n++GaN TJ layer, (b) during p++GaN TJ layer, and (c) after growth of p-GaN cap layer at 600 ºC.

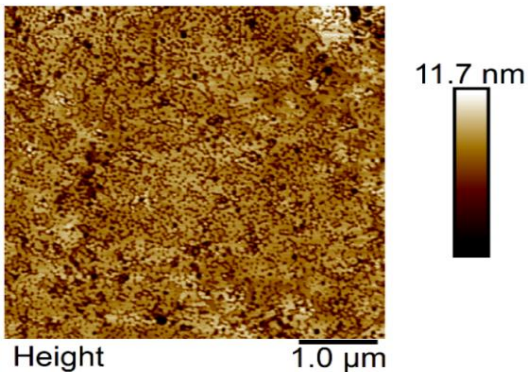

Figure 45. AFM image of the highest doped tunnel diode (sample Mg5) with Si concentration of ~4×10^{20} cm^{-3} and Mg concentration of ~6.3×10^{20} cm^{-3} showing an RMS value of ~1.3 nm.

Figure 46 depicts semi-log and linear J-V characteristics of the grown tunnel diodes. All the tunnel diodes exhibit Zenner type tunneling behavior with asymmetric reverse and forward current density profiles, where the current density at low reverse bias is higher than that of low forward bias. It is evident that by increasing the Mg doping concentration at the junction from ~1.5×10^{20} to ~7×10^{20} cm^{-3}, the conductivity, in forward and reverse biases, increases. This trend can be related to the reduction of depletion width and possibly an increase in the density of midgap states at the junction. Sample Mg5 shows a high current density of 213 and 50 A/cm^2 at -1.0 and 1.0 V. At 0.2 V (-0.2 V) the current density of sample Mg5 is 10x (30x) higher than that of sample Mg1. Sample Mg4 (with a device radius of 100 µm and TJ Mg concentration of ~5.5×10^{20}) shows a negative differential resistance (NDR) in forward bias with a peak current density (PCD) of 147 A/cm^2 at peak voltage (V_P) of 1.8 V and a peak-to-valley-ratio (PVR) of 1.094. All the tunnel diodes across sample Mg4 showed similar characteristics.

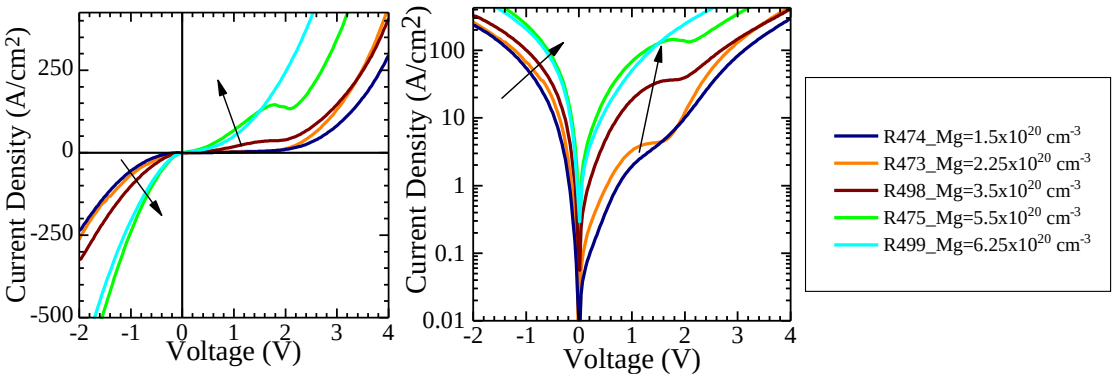

(a) (b)

Figure 46. (a) Linear and (b) semi-log J-V characteristics of the grown tunnel diodes with varying Mg doping at the junction.

Understanding the ohmic behavior of the contacts is necessary in order for them to be deconvoluted from the intrinsic characteristics of the tunnel diode. Thus, a separate p-GaN film was grown on AlN using an identical growth condition to the p-GaN cap layers. The resistance of Ni/Au contacts to the p-GaN was measured using TLM patterns. All the I-V characteristics of the as-deposited contacts show a specific contact resistivity of 1.1×10^{-2} $\Omega.cm^2$, indicating that the p-GaN contact has a limiting effect on the performance of the tunnel diodes. Further optimization of contact resistance is essential to improve the tunnel diode performance.

Esaki band-to-band tunneling has been observed in narrow bandgap material systems (*e.g.*, Ge and GaAs), showing NDR at voltages between 0.1 to 0.4 V [195], [223]. Based on the model proposed by Demassa *et al.*, the peak voltage of the NDR region is directly related to doping degeneracies in conduction and valance bands (E_n and E_p, respectively). The peak voltage of the NDR region is given by

$$V_p = \frac{En + Ep}{3}. \quad (5.1)$$

Based on Eq. 5.1, the measured peak voltage of 1.8 V achieved from sample Mg4 leads to E_n+E_p of ~5.4 V, which implies that the combination of doping degeneracies is well above

their physical limits. In addition, the direct tunneling probability of pn junction can be expressed by WKB approximation, which is inversely related to band gap [224]:

$$T_t \approx \exp\left(-2\int_0^{Wd}\sqrt{\frac{2m^*E_g x}{\hbar^2 q W_d}}\,dx\right), \tag{5.2}$$

where q is the electron charge, $\hbar$ is the reduced Planck's constant, W_d is the depletion width, E_g is the GaN bandgap (3.42 eV), and m* is the effective mass. The band-to-band tunneling probability of sample Mg4 was then calculated to be ~1×10^{-22} (assuming ionized Mg concentration of 5×10^{19} cm^{-3}), which is extremely low. Figure 47 shows the direct tunneling probability of a pn GaN diode vs. hole concentration (considering an electron concentration of 4×10^{20} cm^{-3}). It is evident that even at high hole concentrations, the direct band-to-band tunneling (Esaki-style) is improbable. Similarly, in polarization-assisted tunnel diodes where W_d is equal to the interlayer thickness, the tunneling probabilities are low. For example, for GaN/AlN (2.6 nm)/GaN and GaN/$In_{0.3}Ga_{0.7}N$ (6 nm)/GaN tunnel diodes, the tunneling probabilities are calculated to be 10^{-11} and 10^{-18}, respectively [196], [197]. The feasible mechanism for tunneling in nitride-based materials with wide bandgaps is proposed to be defect-assisted tunneling (DAT) through midgap states in the forbidden gap, such as oxygen contaminants, Mg precipitates, and deep level defects acting as carrier traps (*e.g.,* Ga vacancies in n-GaN and antisite defects and nitrogen vacancies in p-GaN) [225]–[228]. Furthermore, the presence of DAT in nitride-based diodes, where electrons and holes can tunnel through the midgap states, was suggested to be the origin of their high ideality factors (n>2), measured from their I-V characteristics [182], [183], [229].

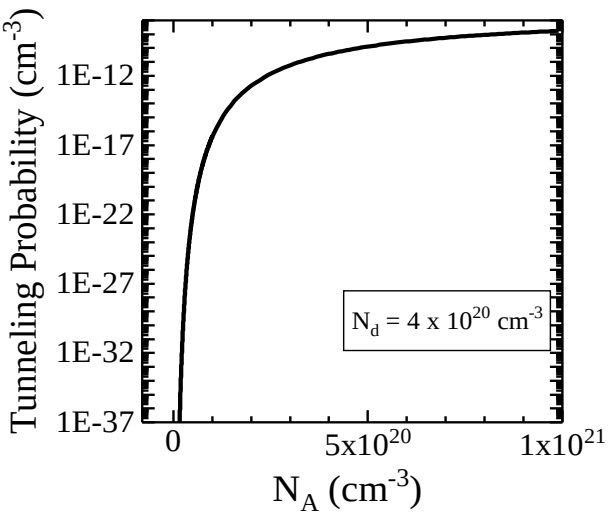

Figure 47. Tunneling probability of a GaN diode with a donor concentration of 4×10^{20} cm^{-3} vs. acceptor concentration derived from WKB model.

In order to investigate the repeatability of the NDR region, consecutive voltage sweeps were performed (see Fig. 48). Sample Mg4 shows a slight degradation of PVR and tunneling current at reverse bias. In addition, the current density at forward bias ($V>V_{valley}$) increases after each voltage sweep. However, after consecutive voltage sweeps (more than 60 scans), no noticeable NDR degradation was identified. The existence of NDR metastability can be related to DAT, where charges can accumulate in the midgap states and change the tunneling behavior [209]. The trapped charges at the midgap states can act as dopants and reduce the effective depletion width and, consequently, tunneling probability. It has been pointed out that if the density and distribution of the midgap states in the space-charge region are high, the carriers can tunnel via DAT, in which carriers tunnel in a staircase route (diagonal tunneling) [230]. Mandurrino *et al.* have shown that at sub-threshold forward bias, DAT (mainly through acceptor-like traps) is the primary carrier transport mechanism in InGaN/GaN MQW blue LEDs grown on SiC templates [231]. They implemented an SRH-like model based on trap energy (E_t) and trap density (N_t) to reproduce the tunneling current at low forward biases. As the grown tunnel diodes were

grown on GaN templates grown on sapphire with a high TDD of ~5×10^8 to 10^9 cm^{-2}, the DAT model can be applied to the GaN homojunction tunnel diodes. Further analytical research needs to be performed to analyze the defect levels (such as deep-level transient spectroscopy (DLTS) and deep-level optical spectroscopy (DLOS)) that are responsible for DAT in GaN homojunction tunnel diodes.

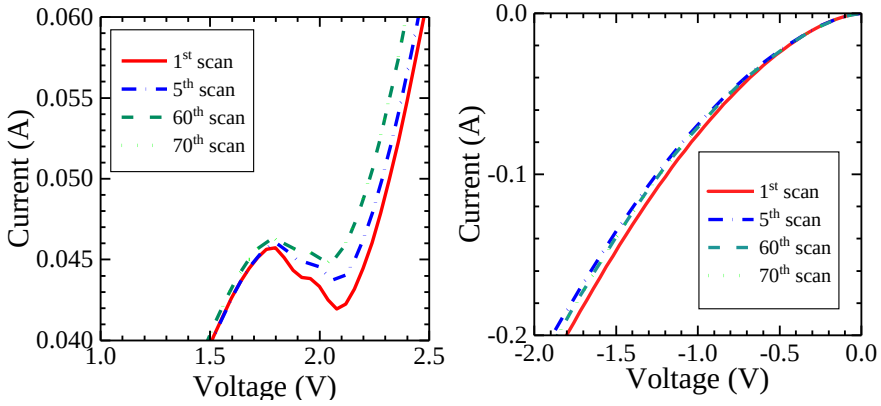

Figure 48. Repeatability of I-V characteristics of sample Mg4 after consecutive voltage sweeps (in forward (a) and reverse (b) biases) showing slight degradation of the NDR region and Zener feature.

Figure 49(a) depicts the temperature dependence of the J-V data of sample Mg4. At 77 K, V_P and PVR show values of 2.48 V and 1.24, respectively. By increasing temperature to room temperature, V_P and PVR reduce, but the current density (tunneling and diffusion currents) at forward bias increases. The presence of tunneling at 77 K confirms (I) a negligible hole freeze out in MME grown p-GaN, (II) temperature independence of tunneling mechanism, and (III) injection of carriers through midgap states at the junction. The negligible carrier freeze-out in p-GaN layers was reported by Gunning *et al.* [39]. Fig. 49(b) shows the J-V characteristics of sample Mg4 at 77 K after multiple voltage weeps to indicate full repeatability and no hysteresis effect. We postulate that at low temperatures, the possible midgap states at the junction deactivate and carriers do not get trapped in them,

leading the full repeatability of the diode. To the best of our knowledge, this is the first reported tunnel diode that has a repeatable NDR at low temperature.

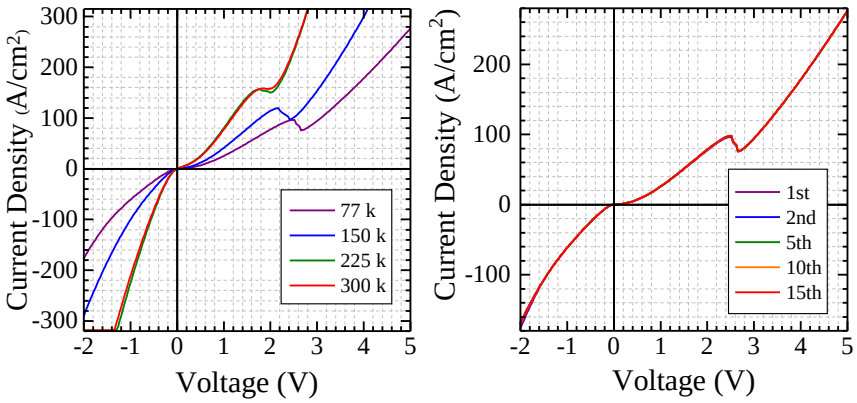

(a) (b)

Figure 49. (a) J-V characteristics of sample Mg4 at different temperatures. (b) J-V characteristics of sample Mg4 at 77 K after multiple voltage sweeps.

5.3.2. GaN Homojunction Tunnel Diode Grown on Free-standing GaN Substrate

The free-standing GaN substrates showed great potentials for achieving high-efficiency nitride-based LEDs and laser diodes due to their low TDD values (in the range of 10^7 cm^{-2}) [232]–[236]. It is reported that dislocations are the possible leakage paths for forward tunneling of nitride-based devices (such as InGaN LEDs on Si substrate) [237]. For example, the repeatability and NDR characteristics of resonant tunneling diodes (RTDs) are significantly impacted by dislocations [238]. In this subsection, the effect of dislocations on the performance of a GaN homojunction tunnel diode which is grown on a free-standing GaN template is examined and critiqued.

The polar GaN (0001) substrate was acquired from slicing a c-plane GaN bulk crystal grown by hydride vapor phase epitaxy (HVPE) at Saint Gobain Lumilog Corporation. The substrate had a TD density of less than 1×10^7 cm^{-2}, an n-type background carrier concentration of ~1×10^{17} cm^3, and an RMS value of less than 1 nm (measured by AFM). The tunnel diode was grown via MME and consists of a 100 nm-thick n-type GaN: Si layer

(Si=1.9×10^{19} cm^{-3}), a heavily doped TJ region (20 nm-thick GaN: Si (4×10^{20} cm^{-3}) and 20 nm-thick GaN: Mg (~5.5×10^{20} cm^{-3})), a 100 nm-thick p-type GaN: Mg layer, and a 20 nm-thick highly doped p-type GaN: Mg contact layer. The epitaxial structure of the grown GaN tunnel diode (sample F) is shown in Fig. 50(a). The grown sample was fabricated into a device by a similar procedure to the tunnel diodes grown on GaN/sapphire substrates.

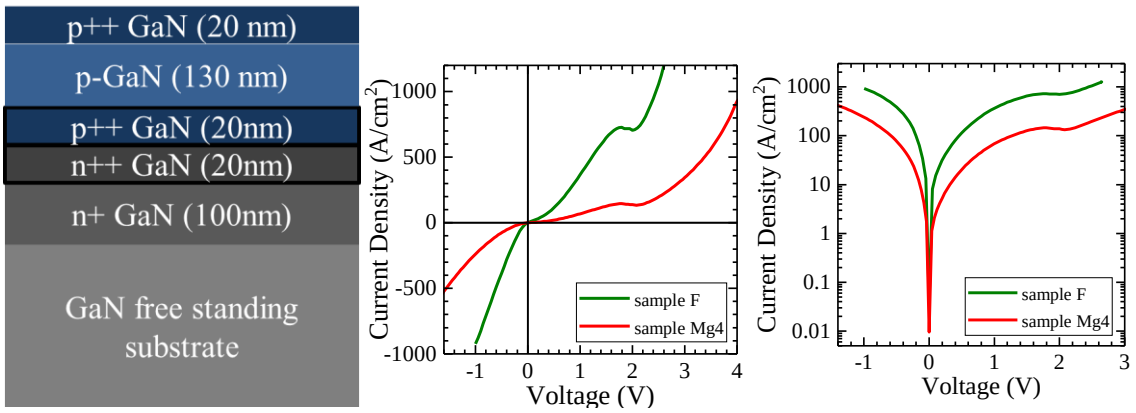

(a) (b) (c)

Figure 50. (a) A schematic structure of a GaN tunnel diode grown a free-standing GaN substrate (sample F). (b) Linear and semi-log J-V characteristics of sample F.

The tunnel diode grown on the free-standing GaN template has a PVR of 1.033 and a peak current density (J_P) of 729 A/cm^2 at V_P of 1.8 V, shown in Fig. 50. The current density of sample F is significantly improved compared to that of sample Mg4 which has a similar structure but was grown on a GaN/sapphire template. At 2.6 V, the current density of sample F reaches a value of 1.273 KA/cm^2, which is significantly higher (2.7x) than that of sample Mg4 (0.461 KA/cm^2). Above the diode's turn-on voltage, where diffusion current is dominant over tunneling current, the current density enhancement can be related to the reduction of SRH recombination centers in the bulk. Contrary to the observation of Cao *et al.*, which reported that the forward tunneling current in InGaN/GaN LEDs, at low positive voltage biases, can be significantly reduced when growing on a low-defect-density GaN template, the forward current density of sample F with a low TDD is higher than that

of sample Mg4 [239], [240]. To the best of our knowledge, this is the highest current density reported for a GaN homojunction tunnel diode. The demonstration of exceptionally low-resistance TJ with low leakage could enable new optoelectronic devices which operate at extremely high current densities and high modulation frequencies with low charging time.

5.2.3. GaN Homojunction Tunnel Diode with Mg delta-Doped Interlayer

Delta-doping is a delta-function-like doping profile to obtain high carrier concentrations beyond solubility limit. This technique reduces the carrier compensation and improves the incorporation of dopants. A delta-doped (δ-doped) layer is defined as a structure that holds spatially confined dopants, whose thickness is narrow as compared to the ground-state wave function of the corresponding free carrier system [241]. The localization of ionized impurities results in a high electric field, leading to band bending and a V-shaped potential. Tunnel diodes (such as Si/SiGe/Si and GaAs) have shown performance improvement by utilizing delta-doping interlayer [242]–[244]. DeSalvo *et al.* have shown a delta-doped GaAs tunnel diode grown via MBE with a current density of 133 A/cm^2 at 0.1 V, which is higher than its counterpart with no delta-doped interlayer [245]. For wide bandgap III-N materials, Si delta-doped n-GaN layers have been reported, showing improved carrier concentrations and low thermal diffusion of carriers into n-GaN layers [246], [247]. It is also argued that Mg δ-doping improves the hole concentration of p-type GaN films without causing material degradation [248]. It is also shown that Mg δ-doping can partially annihilate the propagation of dislocations in GaN crystal [249]–[251]. However, a δ-doped GaN tunnel diode has not been successfully demonstrated yet. In this work, for the first time, the use of Mg delta-doped interlayer in GaN tunnel diodes is

investigated in order to enhance tunneling and hole injection efficiency, showing a significant improvement in tunnel junction specific resistivity compared to the previous results. It is shown that delta-doping can overcome the tunneling limitations associated with the high bandgap and low hole concentrations in GaN by establishing low resistance current paths with reduced tunneling barriers. Unlike the use of InGaN interlayer in GaN tunnel diodes, a delta-doped GaN layer does not introduce high optical absorption loss and growth complication.

The tunnel diodes with Mg δ-doped interlayer at the junction were grown on GaN: Si templates grown on sapphire. The epitaxial structure of these diodes is similar to that of sample Mg3 (described in the previous section) with an additional Mg δ-doped interlayer at the junction, shown in Fig. 51. The tunnel junction regions have Mg and Si doping levels of ~3.5×10^{20} and ~4×10^{20} cm^{-3}, respectively. After the growth of the n++GaN, the growth was interrupted by closing the Ga, Si, and nitrogen plasma shutters and opening the Mg shutter to form localized ionized impurities in a very thin atomic layer. During the impurity insertion, the GaN crystal does not grow, and Mg concentration depends on the flux of Mg and doping time. The location of Mg delta-doping was designed to produce a sharp doping profile. It is believed that the Si dopants are all incorporated into the n++GaN layer, leading to no Si surface residue and carrier compensation. Precise control of the dopant profile, delta-doping time, and growth temperature are all critical for the engineering of a low-resistance tunneling path. The Mg dose of the delta-doped layer was estimated based on the bulk Mg concentration and the growth rate of the Mg-doped p-GaN layer. It is assumed that at a growth temperature of 600 ºC the Mg sticking coefficient is one. The bulk Mg concentration (N_{3D}) of the p-GaN (measured via SIMS analysis) and the growth rate were

~3×10^{20} cm^{-3} and 2.78 Å/s, respectively. By considering the mentioned assumptions, two different Mg delta-doped concentrations were chosen with two dimensional Mg concentrations of 1.6×10^{13} cm^{-2} and 3.2×10^{13} cm^{-2}, corresponding to 20 s and 40 s of Mg delta-doping duration, respectively. Table 15 tabulates the doping concentrations at the junctions. The grown samples were fabricated into devices using conventional photolithography and dry etch processes (similar to the tunnel diodes mentioned in the previous sections).

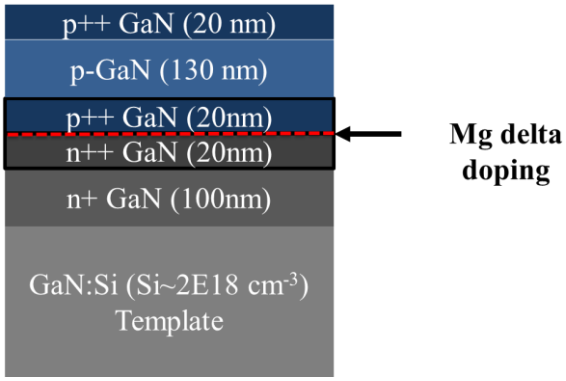

Figure 51. A schematic structure of a GaN tunnel diode with an Mg delta-doped layer at the junction.

TABLE 15. THE DOPING PROFILE OF THE GROWN GAN HOMOJUNCTION TUNNEL DIODES WITH DELTA-DOPED INTERLAYER AT THE JUNCTION.

Sample number	Sample ID	Si concentration (cm^{-3})	Mg concentration (cm^{-3})	Mg delta doping duration (sec)	Mg delta doping concentration (cm^{-2})
R478	D1	4×10^{20}	3.5×10^{20}	20	1.6×10^{13}
R479	D2	4×10^{20}	3.5×10^{20}	40	3.2×10^{13}

The J-V characteristics of the tunnel diodes with δ-doped interlayer are shown in Fig. 52. The presented tunnel diodes with varying Mg concentrations at the junction are also presented for the sake of comparison. All the δ-doped tunnel diodes show Zenner tunneling characteristics. The current density and specific resistivity were dramatically improved in all the Mg delta-doped tunnel diodes. It can also be seen that the increase in the

concentration of Mg δ-doped layer increases the conductivity at forward and reverse biases. Sample D2 with the highest δ-doped concentration ($\delta_{Mg} = 3.2\times10^{13}$ cm^{-2}) shows a current density of 318 A/cm^2 at 1.28 V. At 0.7 V (-0.7 V) the current density of sample D2 is ~149 A/cm^2 (234 A/cm^2). The same epitaxial film with no Mg δ-doped interlayer had a lower current density of ~27 and ~1 A/cm^2 at 1.28 and -0.1 V, respectively. To the best of our knowledge, these are the highest reported current density values for a GaN tunnel diode in the literature.

Notably, both delta-doped tunnel diodes do not exhibit the DR feature at forward bias. This can imply that the excess current which is generated from tunneling through midgap states (*e.g.*, Mg complexes and Mg precipitants) in the depletion region (which is resulted from excessive doping) is dominant. These midgap states form impurity bands, possibly contributing to the high excess current. Typically, the excess current is measured at the valley of the NDR region. Therefore, high Mg delta-doping concentration creates defect states and, consequently, high excess current density. Two similar tunnel diodes (sample D2 and sample Mg3) with the same doping concentrations at the junction but different density of defect sites, have different excess currents.

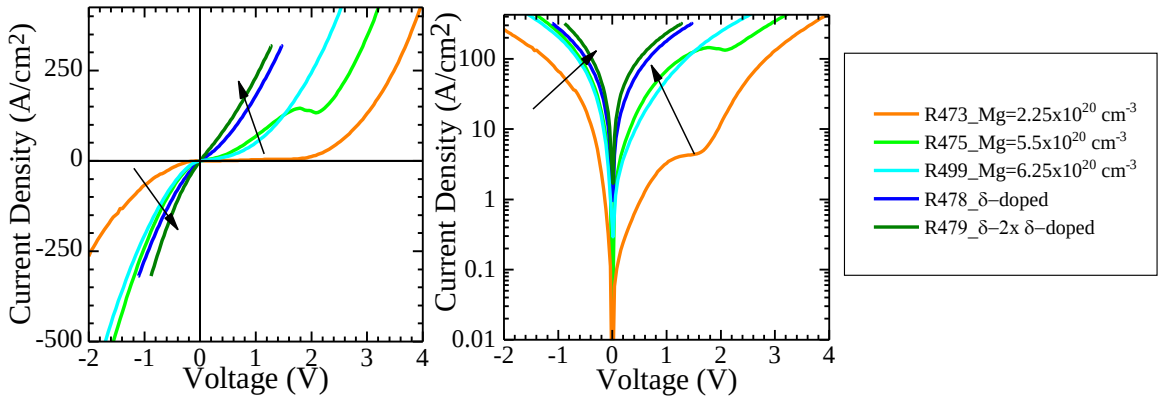

(a) (b)

Figure 52. Linear (a) and semi-log J-V (b) characteristics of the delta-doped tunnel diodes (R478 (D1) and R479 (D2)) compared to the tunnel diodes with no delta-doping at the junction and varying Mg concentration.

Tunneling through midgap states presents energetically in the forbidden gap and can significantly increase the probability of tunneling for several possible reasons. It is shown by Sakowski *et al.* that the acceptor traps which are deeper than donor-like traps can be responsible for tunneling in GaN tunnel diodes [225]. The diffused Mg into the GaN layer can contribute to the tunneling as it can act as an acceptor and increase the band bending at the interface. The band bending at the p-GaN region can consequently reduce the depletion width. TEM measurements and future analytical analysis are under investigation to disclose the nature of tunneling paths.

The reduction of TJ resistance through the implementation of Mg delta-doping at the junction can enable high-efficiency InGaN LEDs with no p-type GaN contact layer and high hole injections. The low-resistance GaN TJs, reported in this work, can also benefit lasers (which operate in KA/cm^2 regimes) by improving modulation bandwidth and reducing series resistance losses.

5.3.4. AlGaN Homojunction Tunnel Diode

The nitride-based UV emitters (LEDs and lasers) have a broad range of applications, such as water and air purification, medical sterilization, and biochemistry [253]. The nitride-based UV emitters divide into the three categories of UV-A (320 to 420 nm), UV-B (280 to 320 nm), and UV-C (200 to 280 nm) which primarily utilizes AlGaN/GaN superlattices as QW active regions. For example, the wavelength range of 200 to 300 nm with a peak wavelength of 270 nm can be absorbed by the DNA of microorganisms, which can ultimately be used for efficient sterilization. There are many challenges associated with the growth and fabrication of high-efficiency UV emitters, such as poor light extraction efficiency, inferior crystalline quality, high contact resistance, low p-type doping of AlGaN films (due to their high activation energy), and poor hole injection efficiency (due to electron overshoot and electron leakage in the p-region). Figure 53 displays the external quantum efficiency vs. emission wavelength of LEDs showing a significant reduction of efficiency in the UV region where the EQE decreases to values as low as 0.01% at 200−300 nm wavelength regime. The low efficiency at ultra-UV wavelength regime is an indication of a fundamental limitation facing the wide-bandgap semiconductor devices (in particular AlGaN).

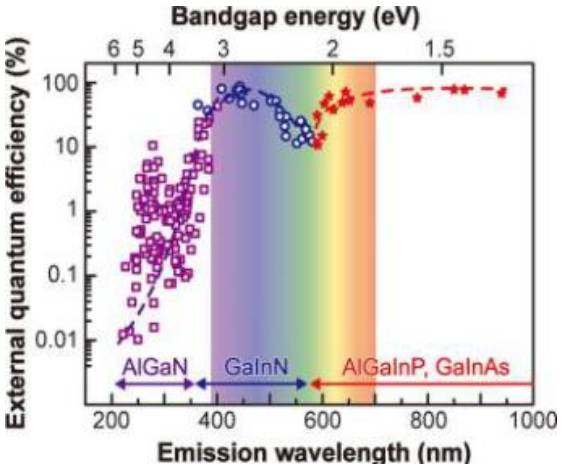

Figure 53. EQE values of InAlGaP- and InGaAs-based IR and InGaN-based visible and AlGaN-based UV LEDs vs. emission wavelength [254].

In recent years, increased attention was placed on improving the performance of AlGaN UV LEDs through the use of buffer layer schemes, low-temperature AlGaN growth, superlattice AlGaN/GaN p-contact layers, and AlGaN growth via metal modulated epitaxy [39], [255]–[257]. The weak light extraction of UV AlGaN LEDs mainly stems from poor reflective p-type electrodes for UV wavelengths, high UV absorption coefficients of p-GaN layers, and high-resistance p-GaN contact layer. The first two issues were addressed by using a p-AlGaN contact layer with the highly reflective p-type electrode to increase the efficiency of deep UV LEDs [258]. The AlGaN/AlGaN superlattice-based transparent UV contact layer was also reported, which led to an external quantum efficiency of more than 10% [258]. The AlGaN/AlGaN superlattice, however, can introduce complications to the crystal growth and increase the overall series resistance of the device.

Based on the two-band Kane model (derived from the k.p perturbation theory), the bandgap (E_g) of semiconductor materials are directly related to their carrier effective mass (m_e*) [258]:

$$\frac{m_e}{m_e^*} = 1 + \frac{2}{m_e E_g} |\langle v| p_x |c\rangle|^2, \quad (5.3)$$

where p_x is the momentum operator in the x-direction, m_e is the free electron mass, $|c\rangle$ is the state at the conduction band minimum, and $|v\rangle$ is the light-hole state at the valence band maximum [254]. It can be deduced that as the bandgap increases the electron effective mass increases. Based on the Kroing-Penney model, carriers with a higher degree of localization have higher effective masses, which means holes in the valance band have higher effective mass than that of electrons. In addition, based on the hydrogen model, as the effective mass increases the ionization energy increases. As a result, as the bandgap increases, the ionization energy of n- and p-type materials asymmetrically increases. N-AlGaN has lower ionization energy than that of p-AlGaN leading to asymmetric carrier injection into the active region of LEDs and lasers. The asymmetry of carrier injection (*i.e.*, lack of efficient hole injection) causes the electron leakage out of the active region. It is reported that among all causes of efficiency droop in LEDs, such as Auger recombination and defect-assisted SRH recombination, the low hole injection is the key mechanism [259]–[261]. Therefore, improving the hole injection into the active region can dramatically improve the performance of LEDs and their efficiency droop issue. All the mentioned challenges can be addressed by tunneling holes from the n-AlGaN to the p-AlGaN layer which can potentially provide a solution for the problems of high contact resistance of p-(Al)GaN and AlGaN/(Al)GaN superlattice (which potentially eliminate the flip-chip bonding). Using tunnel junction to inject holes from n- to p-AlGaN requires low-resistance n-AlGaN/p-AlGaN tunnel junction. In particular, a transparent n-AlGaN top contact layer can replace the widely used p-GaN contact layer and directly connects to the p-AlGaN electron blocking layer in LED, AlGaN cladding layer in EEL (edge emitting

lasers), and AlGaN/GaN p-DBR (distributed brag reflectors) by forming a pn AlGaN homo tunnel junction.

We present AlGaN pn homojunction tunnel diode with Zener tunneling characteristics for the first time. Achieving a high hole concentration in p-AlGaN is challenging due to multiple growth-related limiting factors. (I) High growth temperature is required to increase the adatom mobility of AlGaN films (T > 600 ºC). (II) However, the sticking coefficient of Mg dopants reduces with increasing growth temperature, which depends on the availability of sites on the surface for the incorporation of Mg [262]. (III) Excessive Mg doping leads to the formation of Mg precipitates leading to polarity inversions [35]. In this work, the MME growth method is used in order to kinetically control the incorporation of Mg into the lattice structure of AlGaN at low growth temperatures. The MME growth of AlGaN showed high hole concentrations with low sheet resistance values [39]. It is worth mentioning that the MBE growth of AlGaN film is not affected by hydrogen passivation, unlike MOCVD. Finally, we show that the homoepitaxial structure of AlGaN tunnel junction with low resistances can facilitate efficient tunneling for ultra-wide bandgap devices. Polarization engineered AlGaN/InGaN/AlGaN heterostructure TJ with high Al contents was reported showing high tunneling current density [205]. However, the presence of low bandgap InGaN can dramatically degrade the optical performance of the device due to high UV absorption of the InGaN layer and its poor crystal quality owing to the lattice mismatch between InGaN and AlGaN.

Enabled by the high hole concentration of p-AlGaN films, in this section, the growth, fabrication, and characterization of the AlGaN homojunction tunnel diode are presented. The tunnel diode was grown on a GaN: Si template (with an electron concentration of

2×10^{18} cm^{-3}) grown on c-plane sapphire. The substrate was cleaned via piranha solution prior to loading into the MBE and outgassed in the MBE growth chamber at 650 ºC. A thin buffer layer of GaN: Si was grown at 600 ºC to improve the surface quality, resulting in 2×2 streaky RHEED patterns (not shown here), an indication of smooth and Al-polar layers. The substrate thermocouple temperature was set to 620 ºC for the growth of consecutive AlGaN layers, including 400 nm-thick n-AlGaN (Si=1×10^{19} cm^{-3}), 20 nm-thick n++AlGaN (Si=4×10^{19} cm^{-3}), and 50 nm-thick p++AlGaN layer (Mg=5×10^{19} cm^{-3}). Separate calibration films with 100 nm-thick p- and n-AlGaN layers were grown on AlN templates to acquire the net carrier concentrations, which resulted in values of ~5×10^{19} cm^{-3} and 1×10^{20} cm^{-3} at room temperature, respectively. It is known that the P_{SP} and P_{PZ} at the AlGaN/GaN hetero-interface result in a 2DHG (2-dimensional hole gas) and a significant upward band bending at the junction [263], [264]. It is shown that 2DHG is a minor contributor to the bulk hole concentration, calculated based on Ambacher *et al.* [5], [39].

The AlGaN tunnel diode film quality was evaluated via XRD, showing no phase separation with narrow FWHM values of 313 and 314 arcsec for (002) and (105) ω scans, respectively. In order to extract the relaxation degree and Al content of the AlGaN films, a reciprocal space map (RSM) analysis was performed around the (105) refraction spot. The Al content was calculated to be approximately 10%, and the film was fully strained to the GaN underlayer. The AlGaN homojunction tunnel diode was fabricated into circular devices with different diameters via conventional photo-lithography and dry etch process. Ti/Al/Ti/Au and Pt/Pd/Au were used for the contacts to n- and p-AlGaN layers, respectively. No sidewall passivation was used, and no annealing was performed on the contacts.

The Wentzel–Kramers–Brillouin (WKB) approximation was used to calculate the tunneling probability by considering a constant donor concentration of 1×10^{20} cm^{-3} and varying acceptor concentration (see Fig. 54). In order to understand the space-charge region of AlGaN tunnel junctions, the depletion width at zero bias was also calculated. Bandgap narrowing and band-tail states due to heavy band impurity dopings were not considered in the calculations. An $Al_{0.1}GaN$ tunnel junction with calculated depletion width of 9 nm and a relatively high N_D value of 1×10^{20} cm^{-3} and N_A value of 1×10^{20} cm^{-3} shows a tunneling probability of 1×10^{-22}. The low tunneling probability conveys that the band-to-band tunneling in AlGaN tunnel diodes is highly improbable.

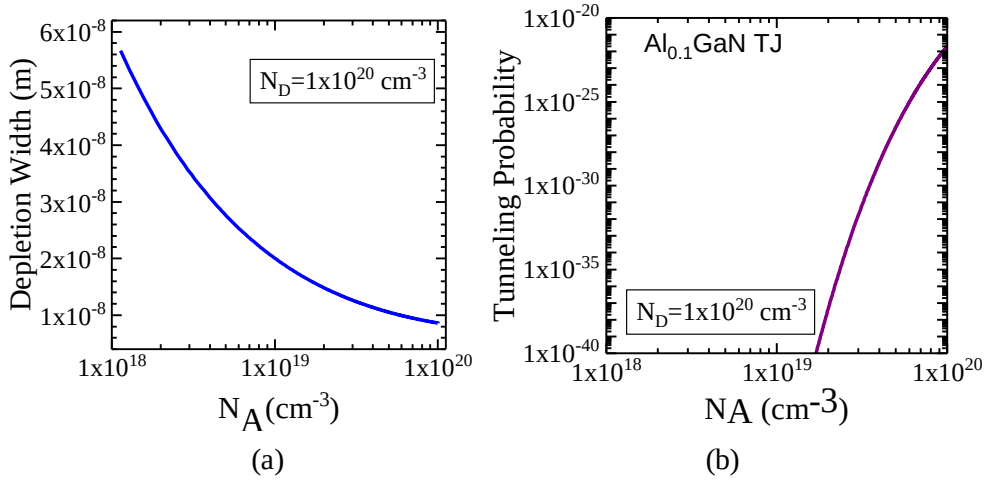

Figure 54. (a) Depletion width and (b) tunneling probability vs. acceptor concentration of the $Al_{0.1}GaN$ tunnel diode with a Si concentration of 1×10^{20} cm^{-3} at the junction.

All the fabricated tunnel diodes showed tunneling behavior with Zener characteristics at the reverse bias. The current density-voltage (J-V) characteristics of the tunnel diodes with different diameters were measured (see Fig. 55). The tunnel diode with a diameter of 300 µm shows a current density of 500 and 70 A/cm^2 at -3.0 and -1.0 V, respectively. Under forward bias of 1.0 and 4.0 V, the current density reaches the values of ~40 and ~450 A/cm^2. The mentioned values confirm the low-resistance of the tunnel diode, which could greatly improve the carrier injection efficiency and reduces electron overflow and

optical absorption. In the case of LEDs and lasers, where the top TJ layer is reverse biased, electrons can tunnel from the valence band of p-AlGaN to the conduction band of n-AlGaN, which results in the injection of holes into p-AlGaN. With tunneling-based hole injection, enabled by a low-resistance homojunction AlGaN tunnel diode, the efficiency of ultra UV optoelectronic devices with high Al contents can be dramatically improved. In future work, the tunnel contacted UV LEDs will be investigated.

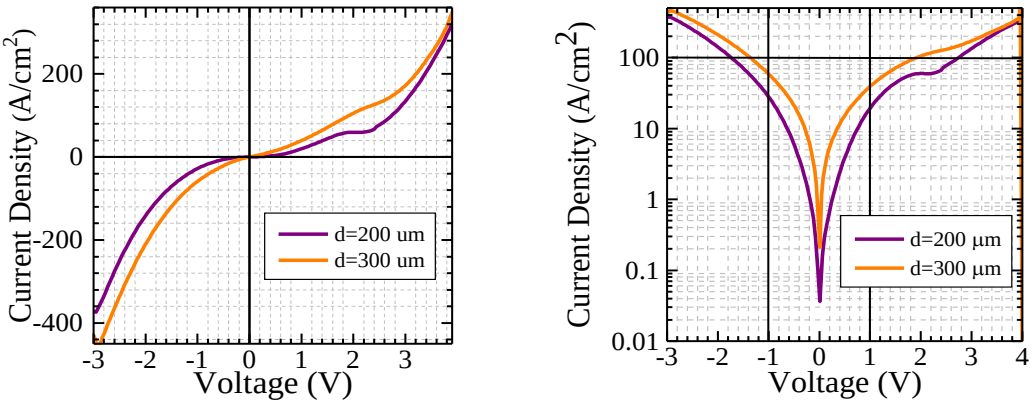

Figure 55. (a) Linear and (b) semi-log J-V characteristics of the AlGaN tunnel diode with two different mesa diameters. The current density of the sample with a diameter of 300 µm is higher than that of the one with a diameter of 200 µm.

CHAPTER 6

INGAN SOLAR CELL WITH HOMOJUNCTION GAN TUNNEL CONTACT

6.1. Introduction

This chapter describes the design, growth, and characterization of the InGaN MQW solar cells with low resistance tunnel contacts. GaN-based tunnel diodes have successfully been implemented in LEDs and lasers as an n-type contact to p-type GaN [228], [265]. The n-type tunnel contacts can improve the current spreading of the resistive p-GaN and improve the hole injection into the active region of LEDs and lasers. In addition, tunnel diode was incorporated into InGaN-based devices as tunnel junctions. Aykol *et al.* have demonstrated a three-junction monolithic LED connected via GaN/InGaN/GaN tunnel junctions, and Kurokawa *et al.* showed a series-connected solar cell with an InGaN interlayer TJ [203],[266]. Hamamatsu *et al.* have demonstrated a nitride-based two-stack laser diode with a tunnel junction [267]. Although there are multiple reports on devices with TJs, further improvement in the conductivity of the TJ (both in forward and reverse biases) is necessary. Motivated by that, this chapter discusses the development of low-resistance GaN homojunction tunnel diodes with negative differential resistance at forward bias and Zener characteristic at the reverse bias. In addition, the TJ was incorporated into an InGaN MQW solar cell for the first time as a contact to the p-GaN.

6.2. InGaN Solar Cell with GaN Homojunction Tunnel Contact

As mentioned in the earlier chapter, the significant remaining challenge in III-nitride-based devices is the lack of low-resistance contacts to p-type GaN due to low hole carrier concentration (N_A) and high hole effective mass. Successful demonstration of GaN TJs would have broad applications in optoelectronics since they convert p-type contact regions

to n-type, which are easier to contact. The reverse-biased and low-forward-biased TJ exhibits an ohmic behavior rather than rectification, providing a highly conductive path from n- to p-layer and resulting in lower series resistance in light-emitting diodes (LEDs). This means that the TJ can be used for efficient hole injection into the p-type region of LEDs and reduce the efficiency droop commonly observed in InGaN-based LEDs, which mainly originates from asymmetric carrier-transport properties of the n-type side (with low activation energy) and p-type side (with high activation energy) [268], [269]. GaN-based TJs were also successfully implemented in vertical-cavity surface-emitting lasers to achieve buried tunnel junctions for carrier confinements [270]. In this work, TJs operating in forward bias are demonstrated for the first time to achieve good carrier extraction in InGaN-based solar cells to overcome the low p-GaN lateral conductivity issue. In addition, TJs can interconnect multiple solar cells with different indium mole fractions and bandgaps, providing a path for multijunction solar cells with higher efficiencies.

In order to increase the lateral conductivity of the p-GaN contact layer of an InGaN solar cell and address the thermal degradation of the active region, an ITO cladding layer has been used [271]. However, adding an ITO on p-GaN can introduce more complications to device fabrication. A highly-doped GaN TJ can be an alternative way to reduce the voltage drop due to the current spreading and an increase in light absorption in the active region. Thus, the TJ can be used in solar cells to provide a low-resistance n-type ohmic contact instead of resistive p-type contact.

In this work, TJ contacted cells were formed using a hybrid growth approach in which the active solar cell regions were grown by MOCVD and the subsequent homojunction GaN TJ contacts were grown by MBE. Different device types, such as LEDs and laser

diodes were reported using this hybrid growth method [272], [273] by regrowth of n-type layers via MBE. However, in this work, different TJ structures with a range of p_+/n_+ GaN layer combinations and varied doping levels were grown on top of the MOCVD-grown p^+GaN contact layers of InGaN/GaN multi-quantum well (MQW) solar cells to conclude the optimum TJ contact design.

The cell structure consists of a 1.0 µm n-GaN (Si ≈ 1×10^{17} cm^{-3}) buffer layer and a 4.5 µm n-GaN (Si ≈ 6×10^{18} cm^{-3}) n-contact layer, followed by the MQW region comprised of a 20-period InGaN (3.0 nm)/GaN (5.6 nm) MQW structure with In mole fraction of ~13.7%, determined by x-ray diffraction (XRD) and photoluminescence peak emission line at 460 nm (~2.7 eV). The MQW active region was then followed by a 150 nm-thick GaN: Mg (~2×10^{19} cm^{-3}) and 10 nm-thick heavily-doped GaN: Mg (~1×10^{20} cm^{-3}). The Hall acceptor concentration (N_A) of the p_+GaN was measured to be ~2×10^{18} cm^{-3} [125]. After the MOCVD growth, the Mg atoms were activated at 810 °C under an N_2-rich environment for 10 minutes. It is worth mentioning that although the growth of the entire InGaN cell with a TJ contact is possible by MOCVD, the thermal activation of buried Mg becomes difficult. H atoms can easily migrate in p-GaN as the binding energy of an electrically neutral Mg acceptor and H donor is ~0.7 eV [274], whereas the high diffusion barrier of H in n-type GaN (~3.4 eV) renders H almost immobile in n-GaN [222]. Thus, the lateral out-diffusion of H from the side mesa walls is possible with dramatic reduction of etched mesa size (*e.g.*, µLEDs), longer thermal annealing time, and higher annealing temperatures [208], [268]. Nevertheless, the active area needs to be large enough to efficiently collect the photo-generated carriers, which makes the lateral diffusion of H challenging. Thus, the hybrid regrowth of InGaN cells with a TJ can be a suitable option to avoid these challenges.

Generally, the surface of MOCVD-grown cells, prior to the MBE regrowth, contain carbon, oxygen, and impurities which can act as unintentional dopants. Various surface treatment methods have been reported to minimize the effect of impurities on carrier transport [275], [276]. In this study, the activated cells were treated with a 49% HF solution for 1 minute at room temperature prior to loading into the MBE chamber. The HF solution was found to produce the lowest series resistance, compared to H_2SO_4: H_2O_2, HCl, and HNO_3: HCl solutions. After loading into the MBE growth chamber, the cells were thermally out-gassed *in-situ* at 700 °C for 20 minutes. The subsequent TJ contacts were then grown via shutter pulsing of Ga and Si. Mg and nitrogen plasma were kept un-shuttered. No polarity inversion was observed during the growth.

Sample N consists of MBE-grown n_{++} (20 nm)/n- (130 nm)/n_{+} (20 nm) GaN layers with Si concentrations of ~4×10^{20}, 1×10^{19}, and 4×10^{19} cm^{-3}, respectively, in series with the MOCVD-grown p^{+}GaN layer (see Fig. 56). All the Si and Mg concentrations in this work were measured using secondary ion mass spectroscopy (SIMS). In order to effectively increase the tunneling probability, N_A at the junction is increased by preparing an additional sample (P/N) in which a 20-nm-thick p++GaN layer (Mg ≈ 3×10^{20} cm^{-3}) was deposited on top of the MOCVD-grown p^{+}GaN layer, followed by n-GaN layers with a similar structure to sample N. The highly-doped n++ and p++GaN show carrier concentrations of 3×10^{20} and 1.5×10^{20} cm^{-3}, and resistivities of 2×10^{-4} and 0.1 $\Omega.cm^2$, respectively.

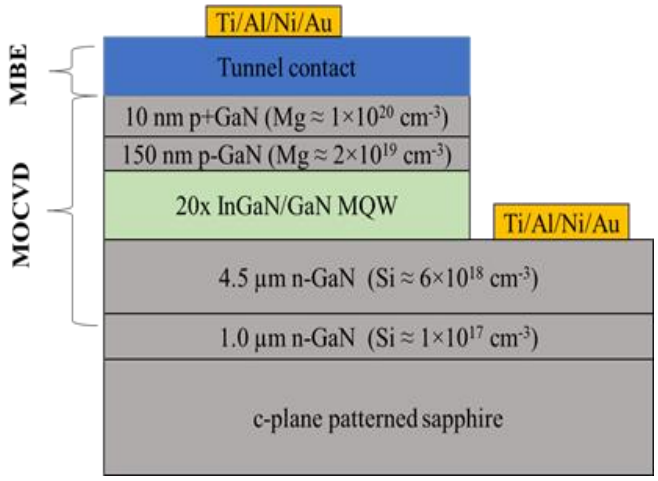

Figure 56. A device structure of an InGaN/GaN cell with a TJ contact. The tunnel contact layer represents four different pn structures.

In order to gain insight into the location and estimated depletion width of the grown TJs, the band alignments of samples N and P/N were calculated by a one-dimensional modeling program (Nextnano^3) at room temperature (see Fig. 57) [176]. The simulated band diagrams at zero applied voltage show that the depletion width of the TJ has been reduced from ~41 nm in sample N to ~6 nm in sample P/N. The tunneling probability in a pn junction can be expressed by the WKB approximation [224]

$$T_t \approx \exp\left(-2\int_0^{Wd}\sqrt{\frac{2m^* E_g x}{\hbar^2 q W_d}}\,dx\right), \tag{6.1}$$

where q is the electron charge, $\hbar$ is the reduced Planck's constant, W_d is the depletion width, E_g is the GaN bandgap (3.42 eV), and m* is the effective mass. Sample P/N shows a band-to-band tunneling probability of ~10^{-15}. This implies that, even at the high doping concentrations achieved via MME, the direct band-to-band tunneling (Esaki tunneling) is still improbable. Similarly, polarization-assisted tunneling with W_d equal to the interlayer thickness yields low values of 10^{-11} for GaN/AlN (2.6 nm)/GaN and 10^{-18} for GaN/$In_{0.3}Ga_{0.7}N$ (6 nm)/GaN [196], [197]. The probable mechanism for the tunneling,

particularly in the wide bandgap materials, is suggested to be defect-assisted tunneling (DAT) through buried impurities in the depletion region, such as Mg precipitates, oxygen contaminants, and deep level defects acting as carrier traps (*e.g.*, nitrogen vacancies and antisite defects in p-GaN and Ga vacancies in n-GaN) [225]–[228]. The presence of DAT in GaN-based diodes was suggested as an explanation for their high ideality factors (n > 2) measured from their I-V characteristics [182], [183], [229]. The effect of DAT has also been reported in AlGaN/GaN resonant tunneling diodes [238].

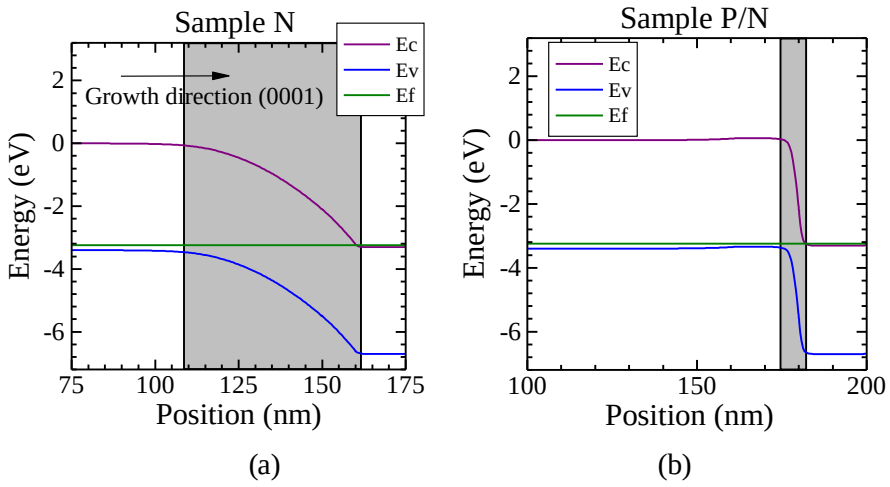

(a) (b)

Figure 57. Band diagrams of the TJ portion of sample N (a) and P/N (b). The approximated depletion regions are indicated by the shading area.

In order to further reduce W_d and the T_t through the defective states at the junction two additional cells were prepared that were similar to sample P/N, but with thin highly-doped GaN interlayers sandwiched between the MBE-grown n++GaN and p++GaN [277], [278]. Sample P+/N contains an additional 5-nm-thick p+++GaN (Mg ≈ 7×10^{20} cm^{-3}) and sample P+/N+ has 5-nm-thick p++GaN (Mg ≈ 7×10^{20} cm^{-3})/9-nm-thick n+++GaN (Si ≈ 7×10^{20} cm^{-3}) interlayers. The Mg doping level is expected to be well beyond the solid solubility of Mg in GaN [4], [222]. However, it is possible to overcome this thermodynamic

limitation by kinetically "trapping" the Mg into the lattice by low-temperature MME growth method, resulting in meta-stable super-saturation acceptors [5].

As shown in Fig. 58, XRD 2θ-ω scans in the vicinity of (0002) reflections of all samples show superlattice features with a period of ~8.5 nm and the absence of indium phase separation. The control cell refers to a separate MOCVD-grown cell with the p_+GaN top layer. The AFM images of the hybrid cells show smooth surfaces with spiral hillock features, an indication of step flow growth, with RMS roughness of less than 0.5 nm, comparable to that of the control cell (see Fig. 59).

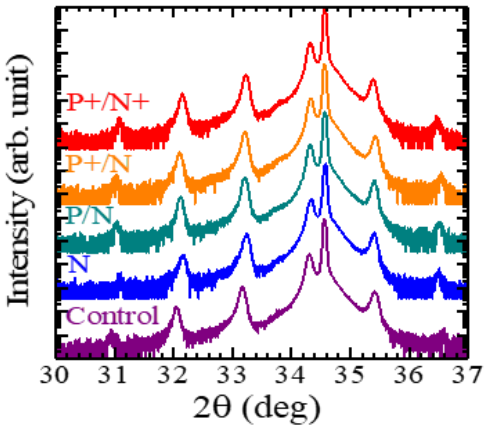

Figure 58. (0002) 2θ–ω diffraction scans showing the absence of phase separation in all the solar cells.

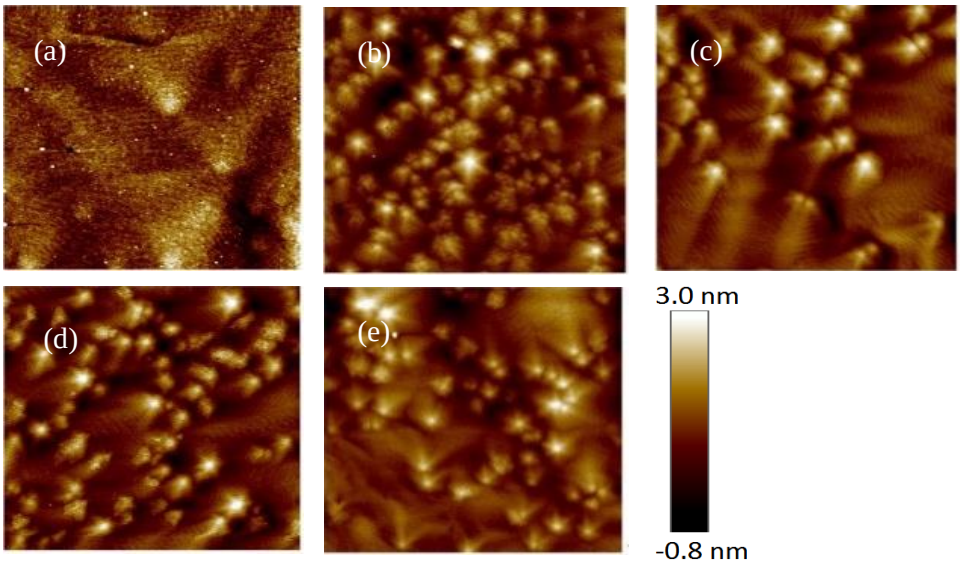

Figure 59. 5×5 μm^2 AFM images of (a) control cell, and tunnel contacted samples: (b) N, (c) P/N, (d) P+/N, (e) and P+/N+.

All the hybrid samples were fabricated into solar cells with an active area of ~0.56 mm^2. Standard photolithography and plasma dry etching (BCl_3/Cl_2) processes were performed to electrically isolate the individual cells. Metal contacts to n-GaN layers were deposited via e-beam evaporation using Ti/Al/Ni/Au. The control cell was fabricated using ITO (150 nm) with a sheet resistance of ~50 Ω/□ as the p-GaN lateral conduction layer and Ti/Pt/Au as metal gridlines on the ITO. The ITO layer was deposited using e-beam evaporation with an excess oxygen flow and post-thermal annealing at 500 °C under an N_2 atmosphere for 10 minutes, which was previously found to optimize the resistivity vs. absorption trade-off. Details on growth and fabrication of the control cell can be found in our previous works [125], [169]. Due to the high carrier concentrations achieved via the MME, the deposited TJ contacts show ohmic behavior without any thermal annealing.

The dark current density-voltage (DJ-V) characteristics of the hybrid and control cells are depicted in the inset of Fig. 60(a). The hybrid cells have 5 to 6 orders of magnitude of rectification between -1 to 3 V, showing reduced turn-on voltage with increased Si and Mg

doping levels in the TJ. At a current density of 40 mA/cm^2, the combined solar cell/TJ forward bias voltage (in which the TJ is reverse biased) was measured to be 3.5, 2.8, 2.74, and 2.68 V for samples N, P/N, P+/N, and P+/N+, respectively, compared to 2.4 V for the control cell. These values indicate that as the doping levels at the junction increase, the voltage drop reduces and the turn-on voltage of the diode lowers (see Fig. 60(a)). Sample P+/N+ shows the lowest slope/intercept extrapolated turn-on voltage of ~2.58 V, compared to ~2.32 V for the control cell. We ascribed the low added voltage drop to the extremely high Mg and Si doping levels and the abrupt junction enabled by MME.

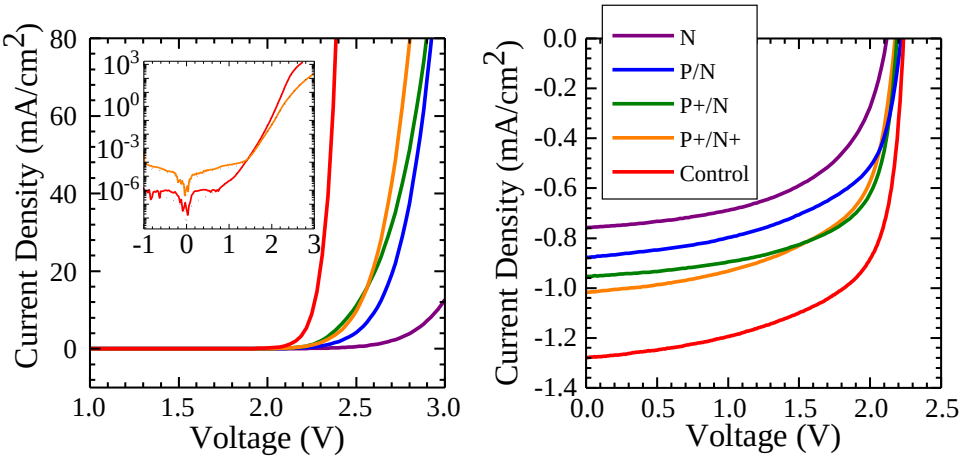

Figure 60. (a) DJ-V and (b) LJ-V characteristics of all the InGaN tunnel contacted solar cells. The inset shows the semi-log DJ-V curves of sample P+/N+ and the control cell.

Comparing the slopes of DJ-V curves of samples N and P/N at forward bias, it was demonstrated that the overall device series resistance is reduced by depositing the MBE-grown p-doped GaN layer on top of the MOCVD-grown p$_+$GaN layer. The specific on-resistance is further reduced by inserting the highly doped GaN interlayers. The DJ-V curves of sample P+/N+ and the control cell were fit to a double-diode model to gain more insight into the effect of the TJ on the solar cell carrier transport (see the inset of Fig. 60(a)). The extracted shunt resistance values for sample P+/N+ and the control cell are ~1.8×10^6

and 1.6×10^6 kΩcm^2, respectively, indicating no significant shunting issues in the hybrid cell. However, the series resistance of sample P+/N+ (3.2 Ωcm^2) is higher than that of the control cell (0.08 Ω.cm^2), implying a higher carrier transport loss in the sample P+/N+. The first ideality factor (n_1) of both cells exhibits a value of ~2 which is commonly attributed to the recombination in the depletion region and is expected in an MQW solar cell. In addition, the second ideality factors (n_2) of sample P+/N+ and the control cell are higher, showing values of 3.4 and 5.1, respectively, which corroborate the presence of the DAT mechanism.

The one-sun light J-V (LJ-V) characteristics of all the cells were acquired by an AM1.5G Oriel class A solar simulator (see Fig. 60(b) and Table 16). The open-circuit voltage (V_{OC}) value of the sample N shows a lower value of ~2.0 V compared to the V_{OC} of 2.24 V of the control cell, which can be related to its high dark current density, originating mainly from the defective regrown junction centered metallurgically in the TJ. However, all other hybrid cells where the p-region was first regrown show similar V_{OC} values (~2.2 V) to the control cell, indicating that the MBE growth of the pn TJ itself does not degrade the crystal quality or increase the leakage current. Sample P/N shows a higher short-circuit current density (J_{SC}) value (0.88 mA/cm^2) than that of sample N (0.76 mA/cm^2). This can be attributed to the shorter tunneling distance of sample P/N enabled by its higher N_A and its reduced density of contaminants at the interface. However, the highly optimized control cell exhibits the highest J_{SC} value (1.28 mA/cm^2). Compared to samples N and P/N, the J_{SC} was increased to 0.94 and 1.02 mA/cm^2 in samples P+/N and P+/N+, respectively, indicating a higher relative carrier collection achieved by using the heavily-doped GaN interlayers. This may be due to the slightly greater band bending

induced by the heavily-doped layers, effectively reducing the tunneling distance and possibly increasing the DAT contribution to the carrier transport. It can be concluded that the presence of highly-doped layers at the junction can improve the electrical performance of the TJ and the cell.

TABLE 16. ELECTRICAL CHARACTERISTICS OF INGAN HYBRID AND CONTROL CELL. $W_{OC} \equiv (E_G/q) - V_{OC}$ = BANDGAP-VOLTAGE OFFSET.

Sample ID	J_{SC} (mA/cm^2)	V_{OC} (V)	FF (%)	η (%)	W_{OC} (V)
N	0.76	2.0	59	0.90	0.95
P/N	0.88	2.22	57	1.11	0.73
P+/N	0.94	2.22	64	1.34	0.73
P+/N+	1.02	2.2	59	1.32	0.75
Control	1.28	2.24	64	1.82	0.71

Since the TJ is critical for the success of future tandem solar cells, yet these first TJ connected devices underperformed the optimized control sample, it is critical to understand where the loss originates. The measured external quantum efficiency (EQE) shown in Fig. 61 provides some insights. The main spectral response of all the hybrid cells occurs in the range of 360-460 nm. In the low wavelength regime (300-360 nm), the control cell exhibits higher EQE values compared to the hybrid cells, as the EQE of the hybrid cells is sharply reduced below ~365 nm. This drop in the EQE is due to the presence of thick and highly-doped MBE-grown top layers with strong absorption at low wavelengths. For instance, for sample N with an added 170 nm of regrown n-type GaN, an absorption depth calculation based on the wavelength-dependent extinction coefficient of GaN reveals that >80% of photons with a wavelength greater than 350 nm will be absorbed [279] before reaching the active layers. Thus, the thickness of the TJ is higher than the penetration depth of the low wavelength photons and needs to be reduced to avoid the parasitic loss.

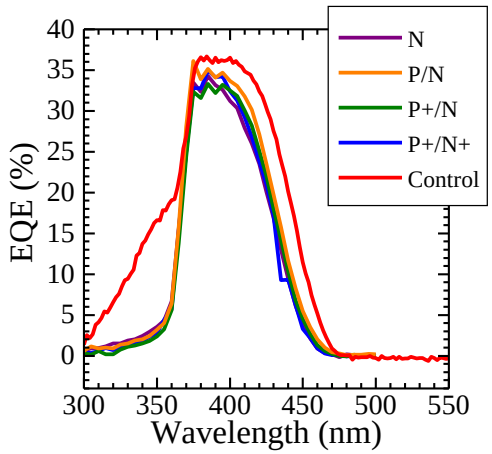

Figure 61. EQE characteristics of all the hybrid solar cells and the control cell.

Conversely, the lower EQE values at the peak and long wavelengths in the hybrid cells compared to the control cell are not inherent to the TJ but are associated with the indium fluctuation in the InGaN/GaN QWs of the control cell. The bandgaps acquired from the inflection points of the EQE data at long wavelengths for the hybrid cells and the control cell show values of ~2.88 and 2.82 eV, respectively, which implies higher In content in the control cell (verified by the XRD).

In addition, although the surface treatment was effective, the presence of contaminants at the interface can still hinder the effective carrier transport through regrown p-layers prior to the TJ. A thin n-doped contaminant sheet charge at the regrowth interface between the MOCVD p+GaN and MBE p++GaN can cause band bending and acts as a barrier to hole extraction. Thus, the regrowth interface is a major limitation in the ultimate utilization of hybrid TJs for the solar cell [275].

6.3. Conclusion

In conclusion, solar cells with low-resistance pn GaN homojunction tunnel contacts were grown via a hybrid MOCVD/MBE method. Increasing the Mg and Si concentrations of the TJ reduces the turn-on voltage of the diode, giving a low voltage drop across the TJ. The best InGaN MQW solar cell with a TJ contact show V_{OC} and J_{SC} values of 2.2 V and

1.02 mA/cm^2, respectively, comparable to the control cell with a traditional top contact based on an ITO.

CHAPTER 7

CONCLUSION AND FUTURE WORKS

7.1. Conclusion

The work presented in this dissertation covered the design, growth, characterization, and fabrication of two different III-V solar cells: III-Sb and III-N solar cells using MBE and MOCVD.

AlGaSb solar cells with different Al compositions grown on GaAs were presented for the first time. The MBE growth of GaSb on GaAs was optimized, leading to a TDD of ~10^8 cm^{-2} using GaSb/Sb superlattices at the interface. Further reduction of TDD was achieved by optimizing the growth conditions of GaSb on GaAs and insertion of $AlAs_ySb_{1-y}$ dislocation blocking layer at the interface on the GaSb/GaAs layer, which led to low TDDs (in the order of ~10^7 cm^{-2}) and increased V_{OC} values of the cells. Although the crystal deterioration and the high density of SRH recombination centers limit the performance of solar cells, the highly lattice-mismatched devices show photovoltaic responses comparable to the lattice matched solar cells.

This study presented the high temperature characteristics of the single-junction $Al_xGa_{1-x}Sb$ cells with different Al compositions (x=0, 0.15, 0.50) over a range of 25–250 °C. Temperature-dependent losses of the cells have been characterized, and the fundamental temperature coefficients have been calculated. The impact of the absorption bands of the incident spectrum on the cell performance has also been highlighted. All the device characteristics showed degradation with temperature. It was shown that while the $Al_xGa_{1-x}Sb$ bandgap reduces with increasing temperature, J_{SC} decreases with a non-linear trend. Also, based on the dark J-V analysis, it was found that the thermally excited intrinsic

carriers dominate the performance degradation of the cells at different temperatures. The detrimental effect of the J_0 on cell performance is expected to be reduced by increasing the incoming light concentration, as it increases the J_{SC} value. In addition, multiple temperature cycles showed the long-term durability of all the cells. To perform a reliable numerical simulation of the GaSb cell performance at different operating temperatures, a set of temperature- dependent material parameters was proposed. The simulation results using the recommended parameters reproduced the experimental findings from the light J-V(T) and EQE(T) measurements.

For the second part of this dissertation, we focused on developing high-efficiency InGaN solar cells that can operate up to 600 ºC with no permanent performance degradation. The temperature-dependent performance of $In_{0.12}Ga_{0.88}N$/GaN MQW solar cells and the influence of the number of quantum wells (9x and 40x) and the QB thickness on the carrier extraction were studied. The absorption edges showed a redshift by increasing the quantum barrier thickness; however, the overall absorption reduces due to the reduction in the e_1-h_1 wavefunction overlap. Although 40 MQW cells have a higher density of photo-generated carriers, it has a higher recombination loss due to its partially depleted active region and inferior material quality. The presented results indicate that for achieving high-performance InGaN solar cells designed to operate at high temperature regimes, the MQW region should be optimized to increase carrier collection, balancing absorption with recombination

GaN homojunction tunnel diodes with different Mg doping profiles at the junction were demonstrated showing NDR and Zaner characteristics. Using a highly doped GaN: Mg layer at the junction, the tunnel diode grown on a free-standing GaN template showed a

PVR of 1.033 and a peak current density (J_P) value of 729 A/cm^2 at V_P at 1.8 V, which is the highest reported in the literature. In addition to a GaN tunnel diode, an AlGaN homojunction tunnel diode was investigated showing the first AlGaN tunnel diode with Zener characteristic. The AlGaN tunnel diode showed a current density of ~500 and ~70 A/cm^2 at -3.0 and -1.0 V, respectively. Under forward biases of 1 and 4 V, the current density reached values of ~40 and ~450 A/cm^2.

After developing the GaN homojunction tunnel diode, solar cells with low-resistance p–n GaN homojunction tunnel contacts were grown via a hybrid MOCVD-MBE method. Increasing the Mg and Si concentrations of the TJ reduced the turn-on voltage of the diode giving a low voltage drop across the TJ. The best InGaN MQW solar cell with a TJ contact showed V_{OC} and J_{SC} values of 2.2 V and 1.02 mA/cm^2, respectively, comparable to those of the control cell with a traditional top contact based on ITO.

7.2. Future Work

The objective of the proposed research is to demonstrate the MBE growth, characterization, and fabrication of tunnel contacted III-N-based devices. However, different areas of growth and fabrication still need to be advanced and understood, such as (a) in-depth knowledge in MBE growth of III-N materials, (b) expertise in material characterization, (c) proficiency in nitride-based device fabrication, and (e) equipment access.

7.2.1. Growth and Fabrication of AlGaN Tunnel Contacted Ultra-UV Emitters

In order to improve the efficiency and reduce the light absorption in the cap layer of solar cells and LEDs (p-GaN contact layer) at low wavelength regimes (<360 nm), different $Al_xGa_{1-x}N$ homojunction tunnel contacted devices can be grown and fabricated. The

devices can be grown either by an MBE or a hybrid growth of MOCVD/MBE. The AlGaN tunnel contact can dramatically increase the hole injection into the active region of LED and reduce the parasitic absorption loss at the p-contact layer.

7.2.2. Investigation of Tunnel Contacted AlGaN Solar Cells

InGaN/GaN heterojunction devices are limited by their blue response mainly due to the use of the p-GaN contact layer with high absorption coefficient. To mitigate this disadvantageous effect, AlGaN tunnel contacted InGaN solar cell can be introduced to replace the absorptive GaN cap later. The proposed structure has an InGaN/GaN MQW absorbing layer and an AlGaN top tunnel contact. Unlike the thick GaN tunnel contacted InGaN solar cells presented in this work, which has high absorption loss at short wavelengths, AlGaN tunnel contacted solar cell is expected to have a lower loss. In addition, InGaN MQW solar cell with a thinner GaN homojunction tunnel contact (<20 nm) can be investigated to be compared to the AlGaN tunnel counterpart.

7.2.2. Investigation of Double-junction InGaN Solar Cell

The InGaN tandem solar cell is achievable via a series connection of InGaN solar cells with different In contents. The proposed structure has a higher bandgap cell with an InGaN/GaN MQW absorbing layer grown via MOCVD and a lower bandgap cell with a double-heterojunction design grown via MBE. Both solar cells are connected monolithically by a GaN homo tunnel junction.

7.2.3. Investigation of InGaN Homojunction Tunnel Diode

In order to achieve homojunction and MJ InGaN solar cells with low series resistances, an InGaN homojunction tunnel junction can be an excellent candidate to introduce a minimal interface polarization and low carrier transport barriers. Motivated by those,

InGaN homojunction tunnel diodes with different In compositions will be investigated. Correlation between the In composition and the tunneling properties of the diodes will be made. This design requires further improvement in the growth of thick InGaN films. The effect of growth techniques (N-rich and MME) on the tunnel diode will also be examined. Low-temperature and nitrogen-rich growth have shown to be able to achieve high quality and optically active InGaN layers, but InGaN films grown via these techniques roughen as InGaN thickness increases, which can lead to an increase in the resistance of the tunnel diode. On the other hand, the MME growth method has shown great promises both in terms of the film quality and the high carrier concentrations. Contingent on obtaining a high-quality InGaN film with a high hole concentration attempts for InGaN homojunction tunnel diodes will be made.

REFERENCES

[1] "Renewables 2017." [Online]. Available: https://www.iea.org/publications/renewables2017/.

[2] National Renewable Energy Laboratory, "Research Cell Record Efficiency Chart." [Online]. Available: https://www.nrel.gov/pv/.

[3] J. Wu, "When group-III nitrides go infrared: New properties and perspectives," *J. Appl. Phys.*, vol. 106, no. 1, p. 011101, 2009.

[4] F. Bernardini, V. Fiorentini, and A. Bosin, "Theoretical evidence for efficient - type doping of GaN using beryllium," *Appl. Phys. Lett.*, vol. 70, no. 10, p. 2990, 1997.

[5] B. P. Gunning *et al.*, "Comprehensive study of the electronic and optical behavior of highly degenerate p- type Mg-doped GaN and AlGaN," *J. Appl. Phys.*, vol. 117, no. 10, p. 45710, 2015.

[6] A. E. Becquerel, "Comptes Rendus des Séances Hebdomadaires," vol. 9, p. 561, 1839.

[7] D. M. Chapin, C. S. Fuller, and G. L. Pearson, "A New Silicon p-n Junction Photocell for Converting Solar Radiation into Electrical Power," *J. Appl. Phys.*, vol. 25, p. 183, 1954.

[8] F. Dimroth *et al.*, "Four-Junction Wafer-Bonded Concentrator Solar Cells," *IEEE J. Photovoltaics*, vol. 6, no. 1, pp. 343–349, Jan. 2016.

[9] M. A. Green, Y. Hishikawa, E. D. Dunlop, D. H. Levi, J. Hohl-Ebinger, and A. W. Y. Ho-Baillie, "Solar cell efficiency tables (version 51)," *Prog. Photovoltaics Res. Appl.*, vol. 26, no. 1, pp. 3–12, 2018.

[10] H. Kroemer, "The family (InAs, GaSb, AlSb) and its heterostructures: a selective review," *Phys. E Low-dimensional Syst. Nanostructures*, vol. 20, no. 3–4, pp. 196–203, Jan. 2004.

[11] C. Hitchcock *et al.*, "Ternary and quaternary antimonide devices for thermophotovoltaic applications," *J. Cryst. Growth*, vol. 195, no. 1, pp. 363–372, 1998.

[12] I. Vurgaftman, J. R. Meyer, and L. R. Ram-Mohan, "Band parameters for III–V compound semiconductors and their alloys," *J. Appl. Phys.*, vol. 89, no. 11, p.

5815, 2001.

[13] Anna Mukhtarova, “InGaN/GaN Multiple Quantum Wells for Photovoltaics,” 2015.

[14] Y. P. Varshni, “Temperature dependence of the energy gap in semiconductors,” *Physica*, vol. 34, no. 1, pp. 149–154, 1967.

[15] T. L. Tansley and C. P. Foley, “Optical band gap of indium nitride,” *J. App. Phys.*, vol. 59, no. 3241, 1986.

[16] V. Y. Davydov *et al.*, “Absorption and Emission of Hexagonal InN. Evidence of Narrow Fundamental Band Gap,” *Phys. status solidi*, vol. 229, no. 3, pp. r1–r3, Feb. 2002.

[17] T. Matsuoka, H. Okamoto, M. Nakao, H. Harima, and E. Kurimoto, “Band parameters for nitrogen-containing semiconductors,” *Appl. Phys. Lett.*, vol. 81, p. 5815, 2002.

[18] J. Wu *et al.*, “Unusual properties of the fundamental band gap of InN,” *App. Phys. Lett.*, vol. 80, no. 21, p. 3967, 2002.

[19] J. Wu *et al.*, “Small band gap bowing in In1−xGaxN alloys,” *Appl. Phys. Lett.*, vol. 80, no. 25, pp. 4741–4743, Jun. 2002.

[20] C.-A. Chang, T.-Y. Tang, P.-H. Chang, N.-C. Chen, and C.-T. Liang, “Magnesium Doping of In-rich InGaN,” *Jpn. J. Appl. Phys.*, vol. 46, no. 5A, pp. 2840–2843, May 2007.

[21] “Global GaN semiconductor devices market is expected to be worth $3438.4M by 2024 | Solid State Technology,” *Solid State Thechnology*. [Online]. Available: https://electroiq.com/2016/08/global-gan-semiconductor-devices-market-is-expected-to-be-worth-3438-4m-by-2024/. [Accessed: 22-Jul-2018].

[22] A. G. Bhuiyan, K. Sugita, A. Hashimoto, and A. Yamamoto, “InGaN Solar Cells: Present State of the Art and Important Challenges,” *IEEE J. Photovoltaics*, vol. 2, no. 3, pp. 276–293, Jul. 2012.

[23] S. R. Routray and T. R. Lenka, “InGaN-based solar cells: a wide solar spectrum harvesting technology for twenty-first century,” *CSI Trans. ICT*, 2017.

[24] X. Cai *et al.*, “Investigation of InGaN p-i-n Homojunction and Heterojunction Solar Cells,” *IEEE Photonics Technol. Lett.*, vol. 25, no. 1, pp. 59–62, Jan. 2013.

[25] O. Jani, I. Ferguson, C. Honsberg, and S. Kurtz, “Design and characterization of solar cells,” *Appl. Phys. Lett.* , vol. 91, no. 10, 2007.

[26] C. A. M. Fabien, A. Maros, C. B. Honsberg, and W. A. Doolittle, “III-Nitride Double-Heterojunction Solar Cells With High In-Content InGaN Absorbing Layers: Comparison of Large-Area and Small-Area Devices,” *IEEE J. Photovoltaics*, vol. 6, no. 2, pp. 460–464, Mar. 2016.

[27] E. A. Clinton *et al.*, “A review of the synthesis of reduced defect density InxGa1−xN for all indium compositions,” *Solid. State. Electron.*, vol. 136, p. 3, 2017.

[28] X. Cai, S. Zeng, and B. Zhang, “Fabrication and characterization of InGaN p-i-n homojunction solar cell,” *Appl. Phys. Lett.*, vol. 95, no. 17, p. 173504, Oct. 2009.

[29] R. M. Farrell *et al.*, “High quantum efficiency InGaN/GaN multiple quantum well solar cells with spectral response extending out to 520 nm,” *Appl. Phys. Lett.*, vol. 98, no. 20, p. 201107, May 2011.

[30] L. Sang, M. Liao, Y. Koide, and M. Sumiya, “InGaN-based thin film solar cells: Epitaxy, structural design, and photovoltaic properties,” *J. Appl. Phys.*, vol. 117, no. 10, p. 105706, Mar. 2015.

[31] J. R. Lang *et al.*, “High external quantum efficiency and fill-factor InGaN/GaN heterojunction solar cells grown by NH3-based molecular beam epitaxy,” *Appl. Phys. Lett*, vol. 98, p. 131115, 2011.

[32] J. H. Park, D. Y. Kim, E. F. Schubert, J. Cho, and J. K. Kim, “Fundamental Limitations of Wide-Bandgap Semiconductors for Light-Emitting Diodes,” *ACS Energy Lett.*, vol. 3, p. 655, 2018.

[33] S. Fischer, C. Wetzel, E. E. Haller, and B. K. Meyer, “On p-type doping in GaN-acceptor binding energies,” *App. phys. lett.*, vol. 67, p. 1298, 1995.

[34] B. N. Pantha, H. Wang, N. Khan, J. Y. Lin, and H. X. Jiang, “Origin of background electron concentration in InxGa1−xN alloys,” *Phys. Rev. B*, vol. 84, p. 75327, 2011.

[35] P. Kozodoy, S. Keller, S. P. Denbaars, and U. K. Mishra, “MOVPE growth and characterization of Mg-doped GaN,” *J. Cryst. Growth*, vol. 195, p. 265, 1998.

[36] Z. Liliental-Weber *et al.*, “Pyramidal defects in metalorganic vapor phase epitaxial Mg doped,” *Appl. Phys. Lett*, vol. 75, p. 61301, 1999.

[37] S. Pezzagna, P. Vennegues, N. Grandjean, and J. Massies, “Polarity inversion of GaN(0 0 0 1) by a high Mg doping,” *J. Cryst. Growth*, vol. 269, pp. 249–256, 2004.

[38] G. Namkoong, E. Trybus, K. K. Lee, M. Moseley, W. A. Doolittle, and D. C. Look, “Metal modulation epitaxy growth for extremely high hole concentrations above 1019cm−3 in GaN,” *Appl. Phys. Lett.*, vol. 93, no. 17, p. 172112, Oct. 2008.

[39] B. Gunning, J. Lowder, M. Moseley, and W. A. Doolittle, “Negligible carrier freeze-out facilitated by impurity band conduction in highly p-type GaN,” *Appl. Phys. Lett.*, vol. 101, no. 10, p. 082106, 2012.

[40] X. Q. Shen, T. Ide, S. H. Cho, M. Shimizu, S. Hara, and H. Okumura, “Surface polarity dependence of Mg doping in GaN grown by molecular-beam epitaxy,” *Appl. Phys. Lett.*, vol. 77, p. 1855, 2000.

[41] F. Tuomisto *et al.*, “Effect of growth polarity on vacancy defect and impurity incorporation in dislocation-free GaN,” *Appl. Phys. Lett,* vol. 86, p. 152108, 2005.

[42] F. Bernardini, V. Fiorentini, and D. Vanderbilt, “Spontaneous polarization and piezoelectric constants of III-V nitrides,” *Phys. Rev. B*, vol. 56, no. 16, 1997.

[43] C. E. Dreyer, A. Janotti, C. G. Van De Walle, and D. Vanderbilt, “Correct Implementation of Polarization Constants in Wurtzite Materials and Impact on III-Nitrides,” *Phys. Rev. X*, vol. 6, p. 021038, 2016.

[44] A. Hangleiter, F. Hitzel, S. Lahmann, and U. Rossow, “Composition dependence of polarization fields in GaInN/GaN quantum wells,” *Appl. Phys. Lett*, vol. 83, p. 1169, 2003.

[45] C. Sah, R. Noyce, and W. Shockley, “Carrier Generation and Recombination in P-N Junctions and P-N Junction Characteristics,” *Proc. IRE*, vol. 45, no. 9, pp. 1228–1243, Sep. 1957.

[46] J. Abell and T. D. Moustakas, “The role of dislocations as nonradiative recombination centers in InGaN quantum wells,” *Appl. Phys. Lett.*, vol. 92, p. 91901, 2008.

[47] Danny Wee, “Characterization of the minority carrier diffusion length using the photocurrent technique in extrinsically doped GaN,” The University of Western Australia, 2014.

[48] Z. Z. Bandić, P. M. Bridger, E. C. Piquette, T. C. Mcgill, and Z. Z. Bandi,

"Electron diffusion length and lifetime in p-type GaN," *Appl. Phys. Lett.*, vol. 73, no. 3222, pp. 52105–2531, 1998.

[49] P. Würfel, T. Trupke, T. Puzzer, E. Schäffer, W. Warta, and S. W. Glunz, "Diffusion lengths of silicon solar cells from luminescence images," *J. App. Phys.*, vol. 101, 2007.

[50] I. Ho and G. B. Stringfellow, "Solid phase immiscibility in GaInN," *Appl. Phys. Lett.*, vol. 69, no. 18, p. 2701, 1996.

[51] C. A. M. Fabien *et al.*, "Low-temperature growth of InGaN films over the entire composition range by MBE," *J. Cryst. Growth*, vol. 425, pp. 115–118, 2015.

[52] M. Rao, D. Kim, and S. Mahajan, "Dependence of composition fluctuation on indium content in InGaN/GaN multiple quantum wells," *App. Phys. Lett.*, vol. 85, p. 2988, 2004.

[53] R. Singh, D. Doppalapudi, T. D. Moustakas, and L. T. Romano, "Dependence of composition fluctuation on indium content in InGaN/GaN multiple quantum wells," *Appl. Phys. Lett.*, vol. 70, p. 2988, 1997.

[54] S. Chen *et al.*, "Nitrogen species from radio frequency plasma sources used for molecular beam epitaxy growth of GaN," *Plasma Sources Sci. Technol. Plasma Sources Sci. Technol*, vol. 9, no. 900, pp. 12–12, 2000.

[55] B. Heying, R. Averbeck, L. F. Chen, E. Haus, H. Riechert, and J. S. Speck, "Control of GaN surface morphologies using plasma-assisted molecular beam epitaxy," *Appl. Phys. Lett.*, vol. 88, p. 1855, 2000.

[56] T. Zywietz, J. Neugebauer, and M. Scheffler, "Adatom diffusion at GaN (0001) and (000$\bar{1}$) surfaces," *Appl. Phys. Lett.*, vol. 73, p. 1855, 1998.

[57] R. Averbeck and H. Riechert, "Quantitative Model for the MBE-Growth of Ternary Nitrides," *Phys. status solidi*, vol. 176, no. 1, pp. 301–305, Nov. 1999.

[58] J. Wu *et al.*, "Superior radiation resistance of In1−xGaxN alloys: Full-solar-spectrum photovoltaic material system," *J. Appl. Phys.*, vol. 94, no. 10, p. 6477, 2003.

[59] C. Yang *et al.*, "Photovoltaic effects in InGaN structures with p-n junctions," *Phys. status solidi*, vol. 204, no. 12, pp. 4288–4291, Dec. 2007.

[60] A. M. Fischer, Y. O. Wei, F. A. Ponce, M. Moseley, B. Gunning, and W. A.

Doolittle, “Highly luminescent, high-indium-content InGaN film with uniform composition and full misfit-strain relaxation,” *Appl. Phys. Lett.*, vol. 103, p. 131101, 2013.

[61] P. Misra, C. Boney, N. Medelci, D. Starikov, A. Freundlich, and A. Bensaoula, “Fabrication and characterization of 2.3eV InGaN photovoltaic devices,” in *3rd IEEE Photovolatic Specialists Conference*, 2008, pp. 1–5.

[62] A. G. Bhuiyan, K. Sugita, A. Hashimoto, and A. Yamamoto, “InGaN solar cells: Present state of the art and important challenges,” *IEEE J. Photovoltaics*, vol. 2, no. 3, pp. 276–293, Jul. 2012.

[63] O. Jani *et al.*, “Effect of phase separation on performance of III-V nitride solar cells,” in *22nd European Photovoltaic Solar Energy Conference*, 2007, pp. 64–67.

[64] C. Boney *et al.*, “Growth and characterization of InGaN for photovoltaic devices,” *Phys. status solidi*, vol. 8, no. 7–8, pp. 2460–2462, Jul. 2011.

[65] E. Matioli *et al.*, “High internal and external quantum efficiency InGaN/GaN solar cells,” *Appl. Phys. Lett.*, vol. 98, no. 2, p. 021102, Jan. 2011.

[66] N. G. Young *et al.*, “High-performance broadband optical coatings on InGaN/GaN solar cells for multijunction device integration,” *Appl. Phys. Lett.*, vol. 104, p. 163902, 2014.

[67] H. C. Lee *et al.*, “Study of Electrical Characteristics of GaN-Based Photovoltaics With Graded InxGa1−xN Absorption Layer,” *IEEE Photonics Technol. Lett.*, vol. 23, no. 6, pp. 347–349, Mar. 2011.

[68] B. Jampana *et al.*, “Realization of InGaN solar cells on (111) silicon substrate,” in *35th IEEE Photovoltaic Specialists Conference*, 2010, pp. 000457–000460.

[69] B. P. Gunning, E. A. Clinton, J. J. Merola, W. A. Doolittle, and R. C. Bresnahan, “Control of ion content and nitrogen species using a mixed chemistry plasma for GaN grown at extremely high growth rates >9 µm/h by plasma-assisted molecular beam epitaxy,” *J. Appl. Phys.*, vol. 1181, no. 10, pp. 155302–5, 2015.

[70] S. D. Burnham, W. Alan Doolittle, G. Namkoong, and W. Henderson, “Mg Doped GaN Using a Valved, Thermally Energetic Source: Enhanced Incorporation, Control and Quantitative Optimization,” *MRS Proc.*, vol. 798, p. Y8.11, Jan. 2003.

[71] Ž. Gačević *et al.*, “A comprehensive diagram to grow (0001)InGaN alloys by molecular beam epitaxy,” *J. Cryst. Growth*, vol. 364, pp. 123–127, 2013.

[72] J. (Zi-J. Ju, B. Loitsch, T. Stettner, F. Schuster, M. Stutzmann, and G. Koblmüller, "Trade-off between morphology, extended defects, and compositional fluctuation induced carrier localization in high In-content InGaN films," *J. Appl. Phys.*, vol. 116, no. 5, p. 053501, Aug. 2014.

[73] M. Azadmand *et al.*, "Droplet Controlled Growth Dynamics in Molecular Beam Epitaxy of Nitride Semiconductors," *Sci. Rep.*, vol. 8, no. 1, p. 11278, Dec. 2018.

[74] M. A. Hoffbauer *et al.*, "In-rich InGaN thin films: Progress on growth, compositional uniformity, and doping for device applications," *J. Vac. Sci. Technol. B, Nanotechnol. Microelectron. Mater. Process. Meas. Phenom.*, vol. 31, no. 3, p. 03C114, May 2013.

[75] T. Kitamura *et al.*, "Growth and characterization of cubic InGaN epilayers on 3C-SiC by RF MBE," *J. Cryst. Growth*, vol. 227, pp. 471–475, 2001.

[76] M. Moseley, D. Billingsley, W. Henderson, E. Trybus, and W. A. Doolittle, "Transient atomic behavior and surface kinetics of GaN," *J. Appl. Phys.*, vol. 106, no. 1, p. 014905, Jul. 2009.

[77] M. Moseley, B. Gunning, J. Greenlee, J. Lowder, G. Namkoong, and W. A. Doolittle, "Observation and control of the surface kinetics of InGaN for the elimination of phase separation," *J. Appl. Phys*, vol. 112, p. 014909, 2012.

[78] R. R. King *et al.*, "Solar cell generations over 40% efficiency," *Prog. Photovoltaics Res. Appl.*, vol. 20, no. 6, pp. 801–815, Sep. 2012.

[79] J. H. Ermer *et al.*, "Status of C3MJ+ and C4MJ Production Concentrator Solar Cells at Spectrolab," *IEEE J. Photovoltaics*, vol. 2, no. 2, pp. 209–213, Apr. 2012.

[80] R. R. King *et al.*, "Band-gap-engineered architectures for high-efficiency multijunction concentrator solar cell," in *Proc. 24th Eur. Photovolt. Sol. Energy Conf. Exhib.*, 2009, pp. 55–61.

[81] A. De Vos, "Detailed balance limit of the efficiency of tandem solar cells," *J. Phys. D. Appl. Phys.*, vol. 13, no. 5, pp. 839–846, May 1980.

[82] S. P. Bremner, M. Y. Levy, and C. B. Honsberg, "Analysis of tandem solar cell efficiencies under AM1.5G spectrum using a rapid flux calculation method," *Prog. Photovoltaics Res. Appl.*, vol. 16, no. 3, pp. 225–233, May 2008.

[83] D. J. Friedman, "Progress and challenges for next-generation high-efficiency multijunction solar cells," *Curr. Opin. Solid State Mater. Sci.*, vol. 14, pp. 131–

138, 2010.

[84] M. P. Lumb *et al.*, "GaSb-Based Solar Cells for Full Solar Spectrum Energy Harvesting," *Adv. Energy Mater.*, p. 1700345, Jul. 2017.

[85] A. Maros, "1-eV GaNAsSb for multijunction solar cells," *IEEE 43rd Photovolt. Spec. Conf.*, pp. 2306–2309, 2016.

[86] D. J. Friedman, A. J. Ptak, S. R. Kurtz, and J. F. Geisz, "Analysis of depletion-region collection in GaInNAs solar cells," in *Conference Record of the Thirty-first IEEE Photovoltaic Specialists Conference, 2005.*, 2005, pp. 691–694.

[87] V. Sabnis, S. Yuen, and M. Wiemer, "High-efficiency multijunction solar cells employing dilute nitrides," in *AIP Conference Proceedings*, 2012, vol. 1477, no. 101.

[88] H. Mohseni, E. Michel, J. Sandoen, M. Razeghi, W. Mitchel, and G. Brown, "Growth and characterization of InAs/GaSb photoconductors for long wavelength infrared range," *Appl. Phys. Lett.*, vol. 71, no. 10, p. 1403, 1997.

[89] L. Zheng, N. J. Mason, G. Verschoor, and S. K. Haywood, "p-GaSb/n-GaAs heterojunction diodes for TPV and solar cell applications," *IEE Proc. - Optoelectron.*, vol. 147, no. 3, pp. 205–208, Jun. 2000.

[90] C. A. Wang *et al.*, "Wafer bonding and epitaxial transfer of GaSb-based epitaxy to GaAs for monolithic interconnection of thermophotovoltaic devices," *J. Electron. Mater.*, vol. 33, no. 3, pp. 213–217, Mar. 2004.

[91] A. H. Eltoukhy and J. E. Greene, "Growth and electrical properties of sputter-deposited single-crystal GaSb films on GaAs substrates," *J. Appl. Phys.*, vol. 50, no. 10, pp. 6396–6405, 2008.

[92] Y.-C. Xin *et al.*, "InAs quantum-dot GaAs-based lasers grown on AlGaAsSb metamorphic buffers," *J. Appl. Phys.*, vol. 94, no. 3, p. 2133, 2003.

[93] D. H. Chow, R. H. Miles, J. R. Söderström, and T. C. McGill, "Growth and characterization of InAs/Ga1−xInxSb strained-layer superlattices," *Appl. Phys. Lett.*, vol. 56, no. 15, p. 1418, 1990.

[94] A. Jallipalli *et al.*, "Structural Analysis of Highly Relaxed GaSb Grown on GaAs Substrates with Periodic Interfacial Array of 90° Misfit Dislocations," *Nanoscale Res. Lett.*, vol. 4, no. 12, pp. 1458–62, Jan. 2009.

[95] M. Mehta, G. Balakrishnan, M. N. Kutty, P. Patel, L. R. Dawson, and D. L. Huffaker, "1.55 μm GaSb/AlGaSb MQW diode lasers grown on GaAs substrates using interfacial misfit (IMF) arrays," in *2007 Conference on Lasers and Electro-Optics (CLEO)*, 2007, pp. 1–2.

[96] D. M. Collins, J. N. Miller, Y. G. Chai, and R. Chow, "Sn and Te doping of molecular beam epitaxial GaAs using a SnTe source," *J. Appl. Phys.*, vol. 53, no. 4, p. 3010, 1982.

[97] J. F. Chen and A. Y. Cho, "Characterization of Te-doped GaSb grown by molecular beam epitaxy using SnTe," *J. Appl. Phys.*, vol. 70, no. 1, p. 277, 1991.

[98] K. Ikossi, M. Goldenberg, and J. Mittereder, "Metallization options and annealing temperatures for low contact resistance ohmic contacts to n-type GaSb," *Solid. State. Electron.*, vol. 46, no. 10, pp. 1627–1631, 2002.

[99] S. H. Huang, G. Balakrishnan, A. Khoshakhlagh, A. Jallipalli, L. R. Dawson, and D. L. Huffaker, "Strain relief by periodic misfit arrays for low defect density GaSb on GaAs," *Appl. Phys. Lett.*, vol. 88, no. 13, p. 131911, Mar. 2006.

[100] M. Manasreh, *Antimonide-Related Strained-Layer Heterostructures*. CRC Press, 1997.

[101] M. B. Katz, M. E. Twigg, N. A. Mahadik, C. L. Canedy, and C. A. Affouda, "Threading and Near-Surface Dislocations in InGaSb/AlSb Films with Blocking and Anti-Blocking Layers," *J. Electron. Mater.*, vol. 45, no. 4, pp. 2102–2107, Apr. 2016.

[102] S. T. Choi and Y. Y. Earmme, "Elastic study on singularities interacting with interfaces using alternating technique," *Int. J. Solids Struct.*, vol. 39, no. 4, pp. 943–957, Feb. 2002.

[103] R. R. King *et al.*, "Band gap-voltage offset and energy production in next-generation multijunction solar cells," *Prog. Photovoltaics Res. Appl.*, vol. 19, no. 7, pp. 797–812, Nov. 2011.

[104] R. Ferrini, M. Patrini, and S. Franchi, "Optical functions from 0.02 to 6 eV of AlxGa1−xSb/GaSb epitaxial layers," *J. Appl. Phys.*, vol. 84, no. 8, p. 4517, 1998.

[105] O. Blum, M. J. Hafich, J. F. Klem, K. Baucom, and A. Allerman, "Wet thermal oxidation of AlAsSb against As/Sb ratio," *Electron. Lett.*, vol. 33, no. 12, p. 1097, 1997.

[106] M. Yamaguchi, A. Yamamoto, N. Uchida, and C. Uemura, "A new approach for thin film InP solar cells," *Sol. Cells*, vol. 19, no. 1, pp. 85–96, 1986.

[107] A. Onnoa *et al.*, "Al0.2Ga0.8As solar cells monolithically grown on Si and GaAs by MBE for III-V/Si tandem dual-junction applications," in *6th International Conference on Silicon Photovoltaics, SiliconPV*, 2016, pp. 661–668.

[108] M. Yamaguchi, A. Yamamoto, and Y. Itoh, "Effect of dislocations on the efficiency of thin-film GaAs solar cells on Si substrates," *J. Appl. Phys.*, vol. 59, no. 3182, pp. 1751–2549, 1986.

[109] S. Manzoor, M. Filipic, M. Topic, and Z. Holman, "Revisiting light trapping in silicon solar cells with random pyramids," in *2016 IEEE 43rd Photovoltaic Specialists Conference (PVSC)*, 2016, pp. 2952–2954.

[110] S. F. Rowlands, J. Livingstone, and C. P. Lund, "Optical modelling of thin film solar cells with textured interfaces using the effective medium approximation," *Sol. Energy*, vol. 76, no. 301, pp. 301–307, 2004.

[111] A. F. P. S. Manzoor, Z.J. Yu, A. Ali, W. Ali, K.A. Bush and Z. C. H. S.F. Bent, M.D. McGehee, "Improved Light Management in Planar Silicon and Perovskite Solar Cells using PDMS Scattering Layer," *Sol. Energy Mater. Sol. Cellls*, vol. 173, p. 59, 2017.

[112] H. M. Branz, W. Regan, K. J. Gerst, J. B. Borak Ac, and E. A. Santori, "Hybrid solar converters for maximum exergy and inexpensive dispatchable electricity," *Energy Environ. Sci.*, vol. 8, no. 8, pp. 3083–3091, 2015.

[113] E. Vadiee *et al.*, "AlGaSb-Based Solar Cells Grown on GaAs : Structural Investigation and Device Performance," *IEEE J. Photovoltaics*, vol. 7, no. 6, pp. 1–7, 2017.

[114] A. De Vos, "Detailed balance limit of the efficiency of tandem solar cells," *J. Phys. D. Appl. Phys.*, vol. 13, no. 5, pp. 839–846, May 1980.

[115] V. L. Teofilo, P. Choong, W. Chen, J. Chang, and Y. Tseng, "Thermophotovoltaic Energy Conversion for Space Applications," in *AIP Conference Proceedings*, 2006, vol. 813, no. 552.

[116] L. M. Fraas, "Infrared Photovoltaics (IR PV) for Combined Solar Lighting and Electricity for Buildings," in *Low-Cost Solar Electric Power*, Cham: Springer International Publishing, 2014, pp. 127–134.

[117] G. Palfinger *et al.*, "Silicon, germanium and silicon/germanium photocells for thermophotovoltaics applications," *Semicond. Sci. Technol.*, vol. 18, pp. 221–227, 2003.

[118] H. Yugami *et al.*, "New approaches to the design of the combustion system for thermophotovoltaic applications Thermophotovoltaic systems," *Semicond. Sci. Technol.*, vol. 18, no. 03, pp. 262–269, 2003.

[119] L. M. Fraas, J. E. Avery, and Han Xiang Huang, "Thermophotovoltaics: heat and electric power from low bandgap 'solar' cells around gas fired radiant tube burners," in *Conference Record of the Twenty-Ninth IEEE Photovoltaic Specialists Conference, 2002.*, pp. 1553–1556.

[120] M. G. Mauk and V. M. Andreev, "GaSb-related materials for TPV cells," *Semicond. Sci. Technol.*, vol. 18, no. 5, pp. S191–S201, May 2003.

[121] A. G. Milnes and A. Y. Polyakov, "Gallium antimonide device related properties," *Solid. State. Electron.*, vol. 36, no. 6, pp. 803–818, Jun. 1993.

[122] J. Fan, "Theoretical temperature dependence of solar cell parameters," *Sol. cells*, vol. 17, pp. 309–315, 1986.

[123] J. J. Wysocki and P. Rappaport, "Effect of Temperature on Photovoltaic Solar Energy Conversion," *J. Appl. Phys*, vol. 31, no. 3, 1960.

[124] L. G. Ferguson and L. M. Fraas, "Theoretical study of GaSb PV cells efficiency as a function of temperature," *Sol. Energy Mater. Sol. Cells*, vol. 39, no. 1, pp. 11–18, 1995.

[125] J. J. Williams *et al.*, "Refractory InGaN Solar Cells for High-Temperature Applications," *IEEE J. Photovoltaics*, vol. 7, no. 6, pp. 1–7, 2017.

[126] A. Maros *et al.*, "High temperature characterization of GaAs single junction solar cells," in *2015 IEEE 42nd Photovoltaic Specialist Conference (PVSC)*, 2015, pp. 1–5.

[127] E. E. Perl, J. Simon, J. F. Geisz, M. L. Lee, D. J. Friedman, and M. A. Steiner, "Measurements and Modeling of III-V Solar Cells at High Temperatures up to 400 C," *IEEE J. Photovoltaics*, vol. 6, no. 5, pp. 1345–1352, Sep. 2016.

[128] C. Yu *et al.*, "Temperature dependence of the band gap of perovskite semiconductor compound CsSnI3," *J. Appl. Phys.*, vol. 110, no. 6, p. 063526, Sep. 2011.

[129] P. Dey *et al.*, "Origin of the temperature dependence of the band gap of PbS and PbSe quantum dots," *Solid State Commun.*, vol. 165, pp. 49–54, 2013.

[130] I. Vurgaftman, J. R. Meyer, and L. R. Ram-Mohan, "Band parameters for III–V compound semiconductors and their alloys," *J. Appl. Phys.*, vol. 89, no. 81, pp. 13710–3675, 2001.

[131] M. Wu, C. Chen, M.-C. Wu, and C.-C. Chen, "Photoluminescence of high-quality GaSb grown from Ga-and Sb-rich solutions by liquid-phase epitaxy," *J. Appl. Phys. J. Appl. Phys.*, vol. 72, no. 68, 1992.

[132] J. Nelson, *The Physics of Solar Cells*. IMPERIAL COLLEGE, UK, 2003.

[133] M. A. Green, "Solar cells: operating principles, technology, and system applications." Prentice-Hall, Inc., Englewood Cliffs, NJ, 1982.

[134] J. C. C. Fan, "Theoretical temperature dependence of solar cell parameters," *Sol. Cells*, vol. 17, no. 2–3, pp. 309–315, Apr. 1986.

[135] J. J. Loferski, "Theoretical Considerations Governing the Choice of the Optimum Semiconductor for Photovoltaic Solar Energy Conversion," *J. Appl. Phys.*, vol. 27, no. 7, pp. 777–784, Jul. 1956.

[136] L. M. Fraas, J. E. Avery, P. E. Gruenbaum, V. S. Sundaram, K. Emery, and R. Matson, "Fundamental characterization studies of GaSb solar cells," in *The Conference Record of the Twenty-Second IEEE Photovoltaic Specialists Conference1991*, pp. 80–84.

[137] A. Chandola, R. Pino, and P. S. Dutta, "Below bandgap optical absorption in tellurium-doped GaSb," *Semicond. Sci. Technol*, vol. 20, pp. 886–893, 2005.

[138] T. R. Harris, "Optical Properties of Si, Ge, GaAs, GaSb,InAs, and InP at Elevated Temperatures," Airforce Institute of Tech., 2010.

[139] S. G03.09, "ASTM G173-03(2012), Standard Tables for Reference Solar Spectral Irradiances: Direct Normal and Hemispherical on 37° Tilted Surface," vol. 14.04.ASTM, pp. 1–21, 2012.

[140] A. L. Fahrenbruch and R. H. Bube, *Fundamentals of solar cells : photovoltaic solar energy conversion*. Academic Press, 1983.

[141] S. A. Ringel, A. W. Smith, M. H. MacDougal, and A. Rohatgi, "The effects of CdCl 2 on the electronic properties of molecular-beam epitaxially grown

CdTe/CdS heterojunction solar cells," *J. Appl. Phys.* , vol. 70, no. 10, pp. 2851–2881, 1991.

[142] H. Bayhan and C. Erçelebi, "Electrical characterization of vacuum-deposited n-CdS/p-CdTe heterojunction devices," *Semicond. Sci. Technol.*, vol. 12, no. 5, pp. 600–608, May 1997.

[143] V. Bellani *et al.*, "Thermoreflectance study of the direct energy gap of GaSb," *Solid State Commun.*, vol. 104, no. 2, pp. 81–84, Oct. 1997.

[144] C. Ghezzi *et al.*, "Optical absorption near the fundamental absorption edge in GaSb," *Phys. Rev. B*, vol. 52, no. 3, pp. 1463–1466, Jul. 1995.

[145] V. Bellani *et al.*, "Thermoreflectance study of the direct energy gap of GaSb," *Solid State Commun.*, vol. 104, no. 2, pp. 81–84, Oct. 1997.

[146] C. Ghezzi *et al.*, "Optical absorption near the fundamental absorption edge in GaSb," *Phys. Rev. B*, vol. 52, no. 3, pp. 1463–1466, Jul. 1995.

[147] S. Michael, A. D. Bates, and M. S. Green, "Silvaco ATLAS as a solar cell modeling tool," in *Conference Record of the Thirty-first IEEE Photovoltaic Specialists Conference, 2005.*, pp. 719–721.

[148] D. M. Caughey and R. E. Thomas, "Carrier mobilities in silicon empirically related to doping and field," *Proc. IEEE*, vol. 55, no. 12, pp. 2192–2193, 1967.

[149] S. Noor Mohammad, A. V. Bemis, R. L. Carter, and R. B. Renbeck, "Temperature, electric field, and doping dependent mobilities of electrons and holes in semiconductors," *Solid. State. Electron.*, vol. 36, no. 12, pp. 1677–1683, Dec. 1993.

[150] D. B. M. Klaassen, "A unified mobility model for device simulation-I. Model equation and concentration dependence," *Solid. State. Electron.*, vol. 35, no. 7, pp. 95–959, 1992.

[151] C. Ghezzi *et al.*, "Electron mobility and physical magnetoresistance in n-type GaSb layers grown by molecular beam epitaxy," *Semicond. Sci. Technol. Semicond. Sci. Technol*, vol. 11, no. 11, pp. 1656–1667, 1996.

[152] V. W. L. Chin and V. W. L., "Electron mobility in GaSb," *Solid. State. Electron.*, vol. 38, no. 1, pp. 59–67, Jan. 1995.

[153] G. Irmer *et al.*, "Determination of the effective Hall factor in p-type

semiconductors," *Semicond. Sci. Technol. Semicond. Sci. Technol*, vol. 13, no. 1398, pp. 505–505, 1998.

[154] M. Sotoodeh, A. H. Khalid, and A. A. Rezazadeh, "Empirical low-field mobility model for III–V compounds applicable in device simulation codes," *J. Appl. Phys.*, vol. 8711, no. 10, pp. 2890–71104, 2000.

[155] D. Martín and C. Algora, "Temperature-dependent GaSb material parameters for reliable thermophotovoltaic cell modelling," *Semicond. Sci. Technol.*, vol. 19, no. 1904, pp. 1040–1052, 2004.

[156] G. Stollwerck, O. V. Sulima, and A. W. Bett, "Characterization and simulation of GaSb device-related properties," *IEEE Trans. Electron Devices*, vol. 47, no. 2, pp. 448–457, 2000.

[157] Vul'.A Ya, *Handbook Series on Semiconductor Parameters*, vol. 1. WORLD SCIENTIFIC, 1996.

[158] P. S. Dutta, H. L. Bhat, and V. Kumar, "The physics and technology of gallium antimonide: An emerging optoelectronic material," *J. Appl. Phys.*, vol. 81, no. 9, p. 5821, 1997.

[159] A. Krier, *Mid-infrared semiconductor optoelectronics*. Springer, 2012.

[160] M. W. Dashiell *et al.*, "Quaternary InGaAsSb Thermophotovoltaic Diodes," *IEEE Trans. Electron Devices*, vol. 53, no. 12, 2006.

[161] Y. Tian *et al.*, "Theoretical analysis of the Auger mechanism in a GaInAsSb infrared photovoltaic detector," *Opt. Eng.*, vol. 37, no. 6, p. 1754, Jun. 1998.

[162] J. A. González-cuevas, "Modeling of the temperature-dependent spectral response of In1-xGaxSb infrared."

[163] S. Adachi, *Properties of Semiconductor Alloys: Group-IV, III-V and II-VI Semiconductors*. John Wiley & Sons, 2009.

[164] D. Martin, C. Algora, D. Martín, and C. Algora, "Temperature-dependent GaSb material parameters for reliable thermophotovoltaic cell modelling," *Semicond. Sci. Technol.*, vol. 19, no. 8, pp. 1040–1052, 2004.

[165] G. W. Charache *et al.*, "Thermophotovoltaic devices utilizing a back surface reflector for spectral control," *AIP Conf. Proc.*, vol. 358, no. 339, 1996.

[166] E. Trybus *et al.*, "InN: A material with photovoltaic promise and challenges," *J. Cryst. Growth*, vol. 288, no. 2, pp. 218–224, 2006.

[167] E. Vadiee *et al.*, "InGaN solar cells with regrown GaN homojunction tunnel contacts," *Appl. Phys. Express*, vol. 11, p. 082304, 2018.

[168] S. Yoshida and J. Suzuki, "High-temperature reliability of GaN metal semiconductor field-effect transistor and bipolar junction transistor," *J. Appl. Phys.*, vol. 85, no. 10, pp. 2940–2273, 1999.

[169] J. J. Williams *et al.*, "Development of a high-band gap high temperature III-nitride solar cell for integration with concentrated solar power technology," in *Conference Record of the IEEE Photovoltaic Specialists Conference*, 2016, vol. 2016–Novem.

[170] B. W. Liou, "Design and fabrication of InxGa1−xN/GaN solar cells with a multiple-quantum-well structure on SiCN/Si(111) substrates," *Thin Solid Films*, vol. 520, no. 3, pp. 1084–1090, 2011.

[171] L. Redaelli *et al.*, "Effect of the quantum well thickness on the performance of InGaN photovoltaic cells," *Appl. Phys. Lett.*, vol. 105, no. 10, pp. 131105–161907, 2014.

[172] J. K. Sheu *et al.*, "High-transparency Ni/Au ohmic contact to p-type GaN," *Appl. Phys. Lett.*, vol. 74, no. 16, p. 2340, Apr. 1999.

[173] L. Zhou, W. Lanford, A. T. Ping, I. Adesida, J. W. Yang, and A. Khan, "Low resistance Ti/Pt/Au ohmic contacts to p-type GaN," *Appl. Phys. Lett.*, vol. 76, no. 23, p. 3451, 2000.

[174] C.-T. Lee and H.-W. Kao, "Long-term thermal stability of Ti/Al/Pt/Au Ohmic contacts to n-type GaN," *App. Phys. Lett.*, vol. 76, no. 17, p. 2364, Apr. 2000.

[175] A. Durbha, S. J. Pearton, C. R. Abernathy, J. W. Lee, P. H. Holloway, and F. Ren, "Microstructural stability of ohmic contacts to InxGa1−xN," *J. Vac. Sci. Technol. B Microelectron. Nanom. Struct.*, vol. 14, no. 4, p. 2582, Jul. 1996.

[176] S. Birner *et al.*, "nextnano: General Purpose 3-D Simulations," *IEEE Trans. Electron Devices*, vol. 54, no. 9, pp. 2137–2142, Sep. 2007.

[177] R. Dimitrov, A. Mitchell, and L. Wittmer, "Pyroelectric properties of Al(In)GaN/GaN hetero- and quantum well structures," *J. Phys. Condens. Matter*, vol. 14, p. 3399, 2002.

[178] W. S. Yan *et al.*, "Temperature dependence of the pyroelectric coefficient and the spontaneous polarization of AlN," *Appl. Phys. Lett.*, vol. 901, no. 10, p. 212102, 2007.

[179] J. J. Wierer, D. D. Koleske, and S. R. Lee, "Influence of barrier thickness on the performance of InGaN/GaN multiple quantum well solar cells," *Appl. Phys. Lett.*, vol. 100, no. 10, pp. 111119–132117, 2012.

[180] N. Watanabe, H. Yokoyama, N. Shigekawa, K. Sugita, and A. Yamamoto, "Barrier Thickness Dependence of Photovoltaic Characteristics of InGaN/GaN Multiple Quantum Well Solar Cells," *Jpn. J. Appl. Phys.*, vol. 51, p. 10ND10, 2012.

[181] X. M. Cai *et al.*, "Study of InGaN/GaN Multiple Quantum Well Solar Cells With Different Barrier Thicknesses," *Phys. status solidi*, vol. 215, no. 10, p. 1700581, Nov. 2017.

[182] P. Perlin *et al.*, "Low-temperature study of current and electroluminescence in InGaN/AlGaN/GaN double-heterostructure blue light-emitting diodes," *Appl. Phys. Lett*, vol. 69, p. 1680, 1996.

[183] M. Binder *et al.*, "Investigations on correlation between I–V characteristic and internal quantum efficiency of blue (AlGaIn)N light-emitting diodes," *Appl. Phys. Lett.*, vol. 103, no. 22, p. 221110, Nov. 2013.

[184] M. Ershov, H. C. Liu, L. Li, M. Buchanan, Z. R. Wasilewski, and A. K. Jonscher, "Negative Capacitance Effect in Semiconductor Devices," *IEEE Trans. Electron Devices*, vol. 45, no. 10, pp. 2196–2206, 1998.

[185] J. E. Garland, D. J. Crain, and D. Roy, "Impedance spectroscopy coupled with voltammetry for quantitative evaluation of temperature and voltage dependent parameters of a silicon solar cell," *Sol. Energy*, vol. 85, no. 11, pp. 2912–2923, Nov. 2011.

[186] J. Panigrahi *et al.*, "Impedance spectroscopy of crystalline silicon solar cell: Observation of negative capacitance," *Sol. Energy*, vol. 136, pp. 412–420, 2016.

[187] I. an Mora-Ser, G. Garcia-Belmonte, P. P. Boix, M. A. V azquez, and J. Bisquert, "Impedance spectroscopy characterisation of highly efficient silicon solar cells under different light illumination intensities," *Energy Environ. Sci.*, vol. 2, pp. 678–686, 2009.

[188] S. E. Laux and K. Hess, "Revisiting the analytic theory of p-n junction impedance:

Improvements guided by computer simulation leading to a new equivalent circuit," *IEEE Trans. Electron Devices*, vol. 46, no. 2, pp. 396–412, 1999.

[189] O. Dupré, R. Vaillon, and M. A. Green, "Physics of the temperature coefficients of solar cells," *Sol. Energy Mater. Sol. Cells*, vol. 140, pp. 92–100, 2015.

[190] K. Bansal and S. Datta, "Voltage modulated electro-luminescence spectroscopy to understand negative capacitance and the role of sub-bandgap states in light emitting devices," *J. Appl. Phys.*, vol. 110, p. 114509, 2011.

[191] W. Yang, D. Li, J. He, C. Wang, and X. Hu, "Temperature-dependent ac current-voltage-capacitance characteristics of GaN-based light-emitting diodes under high forward bias," *Phys. Status Solidi Curr. Top. Solid State Phys.*, vol. 11, no. 3–4, pp. 714–717, 2014.

[192] C. Y. Zhu *et al.*, "Negative capacitance in light-emitting devices," *Solid. State. Electron.*, vol. 53, pp. 324–328, 2009.

[193] and Z. A. Bougrov V, LevinshteinM, Rumyantsev S L, *Properties of Advanced Semiconductor Materials*. New York, 2011.

[194] A. M. Fox, D. A. B. Miller, G. Livescu, J. E. Cunningham, and W. Y. Jan, "Quantum Well Carrier Sweep Out: Relation to Electroabsorption and Exciton Saturation," *IEEE J. Quantum Electron.*, vol. 27, no. 10, pp. 2281–2295, 1991.

[195] L. Esaki, "New Phenomenon in Narrow Germanium p − n Junctions," *Phys. Rev.*, vol. 109, no. 603, 1958.

[196] S. Krishnamoorthy, D. N. Nath, F. Akyol, P. S. Park, M. Esposto, and S. Rajan, "Polarization-engineered GaN/InGaN/GaN tunnel diodes," *Appl. Phys. Lett.*, vol. 97, no. 102, pp. 203502–113503, 2010.

[197] J. Simon *et al.*, "Polarization-Induced Zener Tunnel Junctions in Wide-Band-Gap Heterostructures," *Phys. Rev. Lett.*, vol. 103, p. 026801, 2009.

[198] S. Krishnamoorthy, Fatih Akyol, P. S. Park, and S. Rajan, "Low resistance GaN/InGaN/GaN tunnel junctions," *Appl. Phys. Lett.*, vol. 102, no. 10, p. 113503, 2013.

[199] J. M. O. Zide *et al.*, "Increased efficiency in multijunction solar cells through the incorporation of semimetallic ErAs nanoparticles into the tunnel junction," *Appl. Phys. Lett.*, vol. 88, no. 16, p. 162103, Apr. 2006.

[200] S. Krishnamoorthy, T. F. Kent, J. Yang, P. S. Park, R. C. Myers, and S. Rajan, "GdN Nanoisland-Based GaN Tunnel Junctions," *Nano Lett.*, vol. 13, p. 2570−2575, 2013.

[201] M. Malinverni, D. Martin, and N. Grandjean, "InGaN based micro light emitting diodes featuring a buried GaN tunnel junction," *Appl. Phys. Lett.*, vol. 107, no. 105, 2015.

[202] F. Akyol, S. Krishnamoorthy, and S. Rajan, "Tunneling-based carrier regeneration in cascaded GaN light emitting diodes to overcome efficiency droop," *Appl. Phys. Lett.*, vol. 103, no. 8, p. 081107, Aug. 2013.

[203] Z. Yu-Kun, L. Yu-Feng, and Y.-P. Huang, "GaN-based three-junction cascaded light-emitting diode with low-resistance InGaN tunnel junctions," *Appl. Phys. Express*, vol. 8, 2015.

[204] J. T. Leonard *et al.*, "Demonstration of a III-nitride vertical-cavity surface-emitting laser with a III-nitride tunnel junction intracavity contact," *Appl. Phys. Lett.*, vol. 107, no. 9, p. 091105, Aug. 2015.

[205] Y. Zhang *et al.*, "Design and demonstration of ultra-wide bandgap AlGaN tunnel junctions," *Appl. Phys. Lett.*, vol. 109, p. 121102, 2016.

[206] M. Diagne *et al.*, "Vertical cavity violet light emitting diode incorporating an aluminum gallium nitride distributed Bragg mirror and a tunnel junction," *Appl. Phys. Lett.*, vol. 79, no. 22, pp. 3720–3722, Nov. 2001.

[207] I. Ozden, E. Makarona, A. V Nurmikko, T. Takeuchi, and M. Krames, "A dual-wavelength indium gallium nitride quantum well light emitting diode," *Appl. Phys. Lett.*, vol. 79, no. 16, p. 2532, 2001.

[208] F. Akyol, S. Krishnamoorthy, Y. Zhang, J. Johnson, J. Hwang, and S. Rajan, "Low-resistance GaN tunnel homojunctions with 150 kA/cm2 current and repeatable negative differential resistance," *Appl. Phys. Lett.*, vol. 108, no. 10, p. 131103, 2016.

[209] E. A. Clinton, E. Vadiee, S.-C. Shen, K. Mehta, P. D. Yoder, and W. A. Doolittle, "Negative differential resistance in GaN homojunction tunnel diodes and low voltage loss tunnel contacts," *Appl. Phys. Lett.*, vol. 112, no. 25, p. 252103, Jun. 2018.

[210] M. Moseley, B. Gunning, J. Lowder, W. A. Doolittle, and G. Namkoong, "Structural and electrical characterization of InN, InGaN, and p-InGaN grown by

metal-modulated epitaxy," *J. Vac. Sci. Technol. B*, vol. 31, no. 3, p. 03C104, 2013.

[211] A. Nakajima *et al.*, "High Density Two-Dimensional Hole Gas Induced by Negative Polarization at GaN/AlGaN Heterointerface," *Appl. Phys. Express*, vol. 3, p. 121004, 2010.

[212] G. Namkoong *et al.*, "Metal Modulation Epitaxy Growth for Extremely High Hole Concentrations Above 10^19 cm^-3 in GaN," *Appl. Phys. Lett.*, vol. 93, no. 17, 2008.

[213] S. D. Burnham, G. Namkoong, D. C. Look, B. Clafin, and W. A. Doolittle, "Reproducible increased Mg incorporation and large hole concentration in GaN using metal modulated epitaxy," *J. Appl. Phys.*, vol. 104, no. 2, p. 024902, 2008.

[214] H. M. Ng, D. Doppalapudi, T. D. Moustakas, N. G. Weimann, and L. F. Eastman, "The role of dislocation scattering in n-type GaN films," *Appl. Phys. Lett.*, vol. 73, no. 6, p. 821, Aug. 1998.

[215] N. G. Weimann, L. F. Eastman, D. Doppalapudi, H. M. Ng, and T. D. Moustakas, "Scattering of electrons at threading dislocations in GaN," *J. Appl. Phys.*, vol. 83, no. 7, p. 3656, Jun. 1998.

[216] S. Fritze *et al.*, "High Si and Ge n-type doping of GaN doping - Limits and impact on stress," *Appl. Phys. Lett.*, vol. 100, no. 12, p. 122104, Mar. 2012.

[217] B. Heying, E. J. Tarsa, C. R. Elsass, P. Fini, S. P. DenBaars, and J. S. Speck, "Dislocation mediated surface morphology of GaN," *J. Appl. Phys.*, vol. 85, no. 9, pp. 6470–6476, 1999.

[218] A. Ajay, "Ge doping of GaN beyond the Mott transition," *J. Phys. D Appl. Phys.*, vol. 49, p. 445301, 2016.

[219] P. Bogusławski and J. Bernholc, "Doping properties of C, Si, and Ge impurities in GaN and AlN," *Phys. Rev. B*, vol. 56, no. 15, pp. 9496–9505, Oct. 1997.

[220] E. Trybus *et al.*, "Extremely high hole concentrations in c-plane GaN," *Phys. status solidi*, vol. 6, no. S2, pp. S788–S791, Jun. 2009.

[221] J. Neugebauer and C. G. Van de Walle, "Theory of Point Defects and Complexes in GaN," *MRS Proc.*, vol. 395, p. 645, Jan. 1995.

[222] C. G. Van De Walle, C. Stampfl, and J. Rg Neugebauer, "Theory of doping and defects in III—V nitrides," *J. Cryst. Growth*, vol. 189–190, pp. 505–510, 1998.

[223] N. Holonyak and I. Lesk, "Gallium-Arsenide Tunnel Diodes," *Proc. IRE*, vol. 48, no. 8, pp. 1405–1409, Aug. 1960.

[224] S. M. Sze and K. K. Ng, *Physics of semiconductor devices*. John Wiley & Sons, 2007.

[225] K. Sakowski, L. Marcinkowski, S. Krukowski, S. Grzanka, and E. Litwin-Staszewska, "Simulation of trap-assisted tunneling effect on characteristics of gallium nitride diodes," *J. Appl. Phys.*, vol. 111, no. 86, pp. 123115–44107, 2012.

[226] J. B. Fedison, T. P. Chow, H. Lu, and I. B. Bhat, "Electrical characteristics of magnesium-doped gallium nitride junction diodes," *Appl. Phys. Lett.*, vol. 72, no. 73, pp. 2841–975, 1998.

[227] M. Auf Der Maur, B. Galler, I. Pietzonka, M. Strassburg, H. Lugauer, and A. Di Carlo, "Trap-assisted tunneling in InGaN/GaN single-quantum-well light-emitting diodes," *Appl. Phys. Lett*, vol. 105, p. 133504, 2014.

[228] E. C. Young *et al.*, "Hybrid tunnel junction contacts to III–nitride light-emitting diodes," *Appl. Phys. Express*, vol. 9, no. 2, p. 022102, Feb. 2016.

[229] A. Chitnis *et al.*, "High-quality junctions with quaternary AlInGaN/InGaN quantum wells," *Appl. Phys. Lett*, vol. 77, no. 3800, p. 3800, 2000.

[230] P. Perlin *et al.*, "Low-temperature study of current and electroluminescence in InGaN/AlGaN/GaN double-heterostructure blue light-emitting diodes," *Appl. Phys. Lett*, vol. 69, p. 1680, 1996.

[231] M. Mandurrino *et al.*, "Physics-based modeling and experimental implications of trap-assisted tunneling in InGaN/GaN light-emitting diodes," *Phys. Status Solidi Appl. Mater. Sci.*, vol. 212, no. 5, pp. 947–953, 2015.

[232] H. Asamizu, M. Saito, K. Fujito, J. S. Speck, S. P. DenBaars, and S. Nakamura, "Demonstration of 426 nm InGaN/GaN Laser Diodes Fabricated on Free-Standing Semipolar (1122) Gallium Nitride Substrates," *Appl. Phys. Express*, vol. 1, no. 9, p. 091102, Aug. 2008.

[233] S. S. Park, I.-W. Park, and S. H. Choh, "Free-Standing GaN Substrates by Hydride Vapor Phase Epitaxy," *Jpn. J. Appl. Phys.*, vol. 39, pp. L1141–L1142, Nov. 2000.

[234] Y. Enya *et al.*, "531 nm Green Lasing of InGaN Based Laser Diodes on Semi-Polar {20\bar21} Free-Standing GaN Substrates," *Appl. Phys. Express*, vol. 2, no. 8, p. 082101, Jul. 2009.

[235] M. Lee, M. Yang, K. M. Song, and S. Park, "InGaN/GaN Blue Light Emitting Diodes Using Freestanding GaN Extracted from a Si Substrate," *ACS Photonics*, vol. 5, no. 4, pp. 1453–1459, Apr. 2018.

[236] C. R. Miskys, M. K. Kelly, O. Ambacher, and M. Stutzmann, "Freestanding GaN-substrates and devices," *phys. stat. sol.*, vol. 0, no. 6, pp. 1627–1650, 2003.

[237] J. Kim, Y. Tak, J. Kim, S. Chae, J.-Y. Kim, and Y. Park, "Analysis of forward tunneling current in InGaN/GaN multiple quantum well light- emitting diodes grown on Si (111) substrate," *J. App. Phys.*, vol. 114, p. 013101, 2013.

[238] C. Bayram, Z. Vashaei, and M. Razeghi, "Reliability in room-temperature negative differential resistance characteristics of low-aluminum content AlGaN/GaN double-barrier resonant tunneling diodes," *Appl. Phys. Lett.*, vol. 97, p. 181109, 2010.

[239] X. A. Cao, J. M. Teetsov, M. P. D'evelyn, D. W. Merfeld, and C. H. Yan, "Electrical characteristics of light-emitting diodes grown on and sapphire substrates," *Appl. Phys. Lett*, vol. 85, p. 7, 2004.

[240] D. Yan, H. Lu, D. Chen, R. Zhang, and Y. Zheng, "Forward tunneling current in GaN-based blue light-emitting diodes," *Appl. Phys. Lett*, vol. 96, p. 083504, 2010.

[241] E. E. Schubert, "Delta-Doping of Semiconductors: Electronic. Optical. and Structural Properties of Materials and Devices," *Semicond. SEMIMETALS*, vol. 40, 1994.

[242] S. L. Rommel *et al.*, "Si-based interband tunneling devices for high-speed logic and low power memory applications," in *International Electron Devices Meeting*, 1998, pp. 1035–1037.

[243] J. H. Wolter, M. R. Leys, and F. W. Ragay, "Application of δ-doping in GaAs tunnel junctions," *Electron. Lett.*, vol. 30, no. 1, pp. 86–87, Jan. 1994.

[244] Yan-Kuin Su, Ruey-Lue Wang, and Hann-Huei Tsai, "Delta-doping interband tunneling diode by metal-organic chemical vapor deposition," *IEEE Trans. Electron Devices*, vol. 40, no. 12, pp. 2192–2198, 1993.

[245] G. C. Desalvo, "Ultrathin delta doped GaAs and AlAs tunnel junctions as interdevice ohmic contacts," *J. Appl. Phys.*, vol. 74, p. 4207, 1993.

[246] J.-H. Kim *et al.*, "Si Delta Doped GaN Grown by Low-Pressure Metalorganic Chemical Vapor Deposition," in *MRS Proceedings*, 1998, vol. 537, p. G3.49.

[247] G. Y. Zhao, M. Adachi, H. Ishikawa, T. Egawa, M. Umeno, and T. Jimbo, "Growth of Si delta-doped GaN by metalorganic chemical-vapor deposition," *Appl. Phys. Lett.*, vol. 77, p. 2195, 2000.

[248] J. F. Wheeldon *et al.*, "Performance comparison of AlGaAs, GaAs and InGaP tunnel junctions for concentrated multijunction solar cells," *Prog. Photovoltaics Res. Appl.*, vol. 19, no. 4, pp. 442–452, Jun. 2011.

[249] T. Li *et al.*, "GaN:-Mg grown by MOVPE: Structural properties and their effect on the electronic and optical behavior," *J. Cryst. Growth*, vol. 310, no. 1, pp. 13–21, Jan. 2008.

[250] M. L. Nakarmi, K. H. Kim, J. Li, J. Y. Lin, and H. X. Jiang, "Enhanced p-type conduction in GaN and AlGaN by Mg-δ-doping," *Appl. Phys. Lett.*, vol. 82, no. 18, pp. 3041–3043, May 2003.

[251] C. Bayram, J. L. Pau, R. McClintock, and M. Razeghi, "Delta-doping optimization for high quality p-type GaN," *J. Appl. Phys.*, vol. 104, no. 8, p. 083512, Oct. 2008.

[252] S. Ahmed, M. R. Melloch, E. S. Harmon, D. T. Mcinturff, and J. M. Woodall, "Use of nonstoichiometry to form GaAs tunnel junctions," *Appl. Phys. Lett.*, vol. 71, p. 3667, 1997.

[253] H. Hirayama, N. Maeda, S. Fujikawa, S. Toyoda, and N. Kamata, "Recent progress and future prospects of AlGaN-based high-efficiency deep-ultraviolet light-emitting diodes," *Jpn. J. Appl. Phys.*, vol. 53, no. 10, p. 100209, Oct. 2014.

[254] J. H. Park, D. Y. Kim, E. F. Schubert, J. Cho, and J. K. Kim, "Fundamental Limitations of Wide-Bandgap Semiconductors for Light-Emitting Diodes," *ACS Energy Lett.*, vol. 3, no. 3, pp. 655–662, 2018.

[255] T. Nishida, H. Saito, and N. Kobayashi, "Efficient and high-power AlGaN-based ultraviolet light-emitting diode grown on bulk GaN," *Appl. Phys. Lett.*, vol. 79, no. 6, pp. 711–712, Aug. 2001.

[256] A. Khan, K. Balakrishnan, and T. Katona, "Ultraviolet light-emitting diodes based on group three nitrides," *Nat. Photonics*, vol. 2, no. 2, pp. 77–84, Feb. 2008.

[257] Y. Taniyasu, M. Kasu, and T. Makimoto, "An aluminium nitride light-emitting diode with a wavelength of 210 nanometres," *Nature*, vol. 441, no. 7091, pp. 325–328, May 2006.

[258] N. Maeda and H. Hirayama, "Realization of high-efficiency deep-UV LEDs using

transparent p-AlGaN contact layer," *Phys. status solidi*, vol. 10, no. 11, pp. 1521–1524, Nov. 2013.

[259] J. Cho, E. F. Schubert, and J. K. Kim, "Efficiency droop in light-emitting diodes: Challenges and countermeasures," *Laser Photon. Rev.*, vol. 7, no. 3, pp. 408–421, 2013.

[260] Q. Dai *et al.*, "Carrier recombination mechanisms and efficiency droop in GaInN/GaN light-emitting diodes," *Appl. Phys. Lett.*, vol. 97, no. 13, p. 133507, Sep. 2010.

[261] E. Kioupakis, P. Rinke, K. T. Delaney, and C. G. Van De Walle, "Indirect Auger recombination as a cause of efficiency droop in nitride light-emitting diodes," *Appl. Phys. Lett.*, vol. 98, no. 161107, 2011.

[262] S. Guha, N. A. Bojarczuk, and F. Cardone, "Mg in GaN: Incorporation of a volatile species at high temperatures during molecular beam epitaxy," *Appl. Phys. Lett.*, vol. 71, p. 1685, 1997.

[263] O. Ambacher *et al.*, "Two dimensional electron gases induced by spontaneous and piezoelectric polarization in undoped and doped AlGaN/GaN heterostructures," *J. App. Phys.*, vol. 87, no. 73, pp. 2407–2471, 2000.

[264] O. Ambacher *et al.*, "Measurement of piezoelectrically induced charge in GaN/AlGaN heterostructure field-effect transistors," *J. Appl. Phys.*, vol. 85, p. 1237, 1999.

[265] S. J. Kowsz *et al.*, "Using tunnel junctions to grow monolithically integrated optically pumped semipolar III-nitride yellow quantum wells on top of electrically injected blue quantum wells," *Opt. Express*, vol. 25, no. 4, p. 3841, Feb. 2017.

[266] F. Gan *et al.*, "Multijunction GaInN-based solar cells using a tunnel junction," *Appl. Phys. Express*, vol. 7, p. 034104, 2014.

[267] J. Lian *et al.*, "Nitride-based stacked laser diodes with a tunnel junction," *Appl. Phys. Express*, vol. 11, p. 012701, 2018.

[268] D. Hwang, A. J. Mughal, M. S. Wong, A. I. Alhassan, S. Nakamura, and S. P. DenBaars, "Micro-light-emitting diodes with III–nitride tunnel junction contacts grown by metalorganic chemical vapor deposition," *Appl. Phys. express*, vol. 11, p. 012102, 2018.

[269] Seong-Ran *et al.*, "Lateral current spreading in GaN-based light-emitting diodes

utilizing tunnel contact junctions," *Appl. Phys. Lett.*, vol. 781, no. 10, p. 3265, 2001.

[270] J. Boucart *et al.*, "Metamorphic DBR and tunnel-junction injection. A CW RT monolithic long-wavelength VCSEL," *IEEE J. Sel. Top. Quantum Electron.*, vol. 5, no. 3, pp. 520–529, 1999.

[271] M. T. Hardy *et al.*, "Indium-tin-oxide clad blue and true green semipolar InGaN/GaN laser diodes," *Appl. Phys. Lett.*, vol. 103, no. 10, p. 081103, 2013.

[272] S. Golka *et al.*, "Negative differential resistance in dislocation-free double-barrier diodes grown on bulk GaN," *Appl. Phys. Lett.*, vol. 88, p. 172106, 2006.

[273] B. P. Yonkee *et al.*, "Demonstration of a III-nitride edge-emitting laser diode utilizing a GaN tunnel junction contact," *Opt. Express*, vol. 24, no. 7, p. 7816, 2020.

[274] J. Neugebauer and C. G. Van de Walle, "Atomic geometry and electronic structure of native defects in GaN," *Phys. Rev. B*, vol. 50, no. 11, pp. 8067–8070, Sep. 1994.

[275] S. Chowdhury, M. H. Wong, B. L. Swenson, and U. K. Mishra, "CAVET on Bulk GaN Substrates Achieved With MBE-Regrown AlGaN/GaN Layers to Suppress Dispersion," *IEEE Electron Device Lett.*, vol. 33, no. 1, pp. 41–43, Jan. 2012.

[276] B.P. Yonkee, E. C. Young, S. P. DenBaars, S. Nakamura, and J. S. Speck, "Silver free III-nitride flip chip light-emitting-diode with wall plug efficiency over 70% utilizing a GaN tunnel junction," *Appl. Phys. Lett.*, vol. 109, 2016.

[277] H. Okumura, D. Martin, M. Malinverni, and N. Grandjean, "Backward diodes using heavily Mg-doped GaN growth by ammonia molecular-beam epitaxy," *Appl. Phys. Lett.*, vol. 108, p. 072102, 2016.

[278] C. Bayram, Z. Vashaei, and M. Razeghi, "Room temperature negative differential resistance characteristics of polar III-nitride resonant tunneling diodes," *Appl. Phys. Lett.*, vol. 97, p. 092104, 2010.

[279] T. Kawashima, H. Yoshikawa, S. Adachi, S. Fuke, and K. Ohtsuka, "Optical properties of hexagonal GaN," *J. Appl. Phys.*, vol. 82, no. 97, pp. 2572–61301, 1997.

APPENDIX A

INGAN SOLAR CELL FABRICATION PROCESS

TABLE 17. THE INGAN MQW SOLAR CELL FABRICATION PROCESS USED IN THIS WORK IS PRESENTED HERE.

Stage 1: Lot start		
Step # / Process	Parameters	Special instructions
1.1 Activation anneal	RTP: 810 deg 10 min N_2	

Stage 2: Mesa isolation etch		
Step # / Process	Parameters	Special instructions
2.1 Wafer clean	DI water clean and blow dry	
2.2 Resist coat	Dehydration Hotplate 120C / 5 min HMDS 3000 rpm / 30 sec. HMDS bake 100C/60s AZ4330 / 3000 rpm / 30s Softbake 100C / 120 sec	
2.3 Pattern expose	OAI aligner Mask: MESA Exposure: 200mJ/cm^2, 20 seconds	
2.4 Develop / inspect /bake	MIF-300 Immersion time 120 s Rinse / blow dry Inspect Hardbake 120C / 60 sec	
2.5 Isolation etch	Tool: AGE Recipe: GANISO2 Pressure: 5 mT Ar flow: 5 sccm Cl_2 Flow: 30 sccm BCl_3 Flow: 8 sccm Coil Power: 400 W Platen Power: 70 W	Condition chamber by running O_2CLEAN and GANISO$_2$ recipe

2.6 Demount / Measure step height	Dektak	Acetone / IPA demount
2.7 Resist strip	AZ 400T / 50 C Single bath ~30 min Rinse/blow dry	
2.8 Inspection	Check for resist residue or veils. Use additional piranha clean if required.	

Stage 3: N layer contact		
Step # / Process	Parameters	Special instructions
3.1 Dehydration bake	Dehydration Hotplate 180C / 5 min.	
***Image Reversal	AZ5214IR 2000rpm/30sec Soft bake 100C/90sec Exposure 50 mJ/cm^2 (5 sec) PEB 115C/ 1min Flood exposure 200 mJ/cm^2 Development AZ 300/20 Sec	For image reversal recipe → substitute for 3.2 to 3.5
3.2 LOR coat	CEE Coater LOR-10A Spin: 3000 rpm/ 30sec Bake: 180C/ 60 sec	LOR does not clean well with acetone or IPA.
3.3 Resist coat	AZ3312 / 3000 rpm / 30 sec Softbake 100C / 120 sec	
3.4 Pattern expose	OAI aligner Mask: N CONT Exposure: 60 mJ/cm^2, 6 sec. PEB: 110C / 60 sec	
3.5 Develop / inspect / bake	AZ 300 MIF Immersion time: 90 sec Rinse/blow dry	Verify the development rate of LOR before develop

3.6 Pre-metal clean	Solution: 40:60 HCl:H_2O Time: 180 seconds Room temp DI rinse & blow dry	Within 30 minutes of loading evaporator
3.7 Metallization	Lesker #3 Metal: Ti/Al/Ni/Au 150/2200/400/2000 Å	Include test chip (SiO_2 / Si) with tape mask
3.8 Measure metal thickness and sheet rho	Dektak	Use tape masked test chip
3.9 Liftoff / inspection	AZ400T / Ultrasonic Two baths at ≥ 50C Bath 1 until metal lifted (20 min) Bath 2 for clean up DI rinse and blow dry Microscope inspection	sonication required Inspect all wafers
3.10 Anneal	Heatpulse RTP 760° C, N_2, 2 min Recipe: GAN_760_2min	2 minutes ramp to temperature

Stage 4: ITO		
Step # / Process	Parameters	Special instructions
4.1 Dehydration bake	Dehydration Hotplate 180 ℃ Time: 5 min	
4.2 LOR coat	CEE Coater LOR-10A Spin: 3000 rpm/ 30sec Bake: 180C/ 60 sec	LOR does not clean well with acetone or IPA.
4.3 Resist coat	AZ3312 / 3000 rpm / 30 sec Softbake 100C / 120 sec	
4.4 Pattern expose	OAI aligner Mask: ITO Exposure: 60 mJ/cm^2, 6 sec. PEB: 110C / 60 sec=	Use 6” chuck

4.5 Develop / inspect	AZ 300 MIF Immersion time: 90 sec Rinse/blow dry Microscope inspection	Verify the development rate of LOR before develop
4.6 N_2 plasma clean	Lesker #1 N_2 / 5 mT / 100W / 60 sec	
4.7 ITO deposition	Lesker #1 150 nm	Include test chip (SiO_2 / Si) for R_s measurement (Target: 20 to 50 Ω/sq). Use ellipsometry for thickness measurement
4.8 Liftoff/inspection	AZ400T / Ultrasonic Two baths at ≥ 50C Bath 1 until metal lifted (20 min) Bath 2 for clean up DI rinse and blow dry Microscope inspection	
4.9 ITO contact anneal	MiniBrute furnace 500C / N_2 high flow / 15 min	Ramp (15 min), anneal 15 min and cool (120 min) with sample loaded under high flow N_2.

Stage 5: P-layer contact		
Step # / Process	Parameters	Special instructions
5.1 Dehydration bake	Dehydration Hotplate 180 °C Time: 5 min	
5.2 LOR coat	CEE Coater LOR-10A Spin: 3000 rpm/ 30sec Bake: 180C/ 60 sec	Line the coat bowl with aluminum foil. LOR does not clean well with acetone or IPA.

5.3 Resist coat	AZ3312 / 3000 rpm Softbake 100C / 120 sec	
5.4 Pattern expose	OAI aligner Mask: TP CONT Exposure: 60 mJ/cm^2, 6 sec. PEB: 110C / 60 sec	
5.5 Develop / inspect / bake	AZ 300 MIF Immersion time: 120 sec Rinse/blow dry Microscope inspection	Verify development rate of LOR before develop
5.6 Pre-metal clean	BOE 20:1 8 seconds room temp rinse & dry	30 minutes before loading evaporator
5.7 Metal deposition	Lesker #3 Ti/Pt/Au 150/125/2000 Å	Include test chip (SiO_2 / Si) with tape mask
5.8 Measure metal thickness and sheet rho	Dektak thickness Target = 2,275 Å	Use test chip
5.9 Liftoff / inspection	AZ400T / Ultrasonic Two baths at ≥ 50C Bath 1 until metal lifted (20 min) Bath 2 for clean up DI rinse and blow dry	

Stage 6: Test		
Step # / Process	Parameters	Special instructions
6.1 TLM structures	Measure n-TLM Pattern (30 µm, 40 µm, & 100µm pads) Measure p-TLM Pattern (30 µm, 40 µm, 100 µm & 150µm pads Measure TP-TLM Pattern (30 µm, 40 µm, 100 µm & 150µm pads)	